University of Granada
Faculty of Sciences
Department of Optics

Characterization of Dental Biomaterials by Means of Optical Methods

PhD Thesis

Official Post-graduate Program in Physics

Alicia Fernández Oliveras

Bachelor's Degree in Physics

Bachelor's Degree in Optics and Optometry

Master in Advanced Methods and Techniques in Physics

Granada, 2013

Editor: Editorial de la Universidad de Granada
Autor: Alicia Fernández Oliveras
D.L.: GR 506-2014
ISBN: 978-84-9028-813-9

Universidad de Granada
Facultad de Ciencias
Departamento de Óptica

Caracterización de Biomateriales Dentales Mediante Métodos Ópticos

Tesis Doctoral

Programa Oficial de Posgrado en Física

Alicia Fernández Oliveras

Licenciada en Física

Diplomada en Óptica y Optometría

Máster en Métodos y Técnicas Avanzadas en Física

Granada, 2013

Universidad de Granada
Facultad de Ciencias
Departamento de Óptica

Memoria presentada por:
Alicia Fernández Oliveras
Para optar al Título de:
DOCTOR
por la Universidad de Granada
con Mención Internacional

Fdo.: Alicia Fernández Oliveras

Universidad de Granada
Facultad de Ciencias
Departamento de Óptica

Caracterización de Biomateriales Dentales Mediante Métodos Ópticos

Los doctores María del Mar Pérez Gómez, Catedrática de Escuela Universitaria y Antonio Manuel Rubiño López, Catedrático de Escuela Universitaria, ambos pertenecientes al Departamento de Óptica de la Universidad de Granada.

Certifican:

Que el trabajo de investigación que recoge esta Memoria de Tesis Doctoral, titulada **"Caracterización de Biomateriales Dentales Mediante Métodos Ópticos"**, presentada por la Licenciada en Física, Diplomada en Óptica y Optometría y Máster en Métodos y Técnicas Avanzadas en Física Dña. Alicia Fernández Oliveras para optar al título de Doctor por la Universidad de Granada con Mención Internacional, ha sido realizada bajo nuestra dirección en el Departamento de Óptica de la Universidad de Granada.

Vº Bº La Directora de Tesis

Fdo. Dr. María del Mar Pérez Gómez
Catedrática de Escuela Universitaria
Departamento de Óptica
Universidad de Granada

Vº Bº El Director de Tesis

Fdo. Dr. Antonio Manuel Rubiño López
Catedrático de Escuela Universitaria
Departamento de Óptica
Universidad de Granada

Universidad de Granada

Facultad de Ciencias

Departamento de Óptica

Caracterización de Biomateriales Dentales Mediante Métodos Ópticos

La doctoranda, Alicia Fernández Oliveras, y los directores de la tesis, María del Mar Pérez Gómez y Antonio Manuel Rubiño López, al firmar esta tesis doctoral.

Garantizamos:

Que el trabajo ha sido realizado por la doctoranda bajo la dirección de los directores de la tesis y hasta donde nuestro conocimiento alcanza, en la realización del trabajo, se han respetado los derechos de otros autores a ser citados, cuando se han utilizado sus resultados o publicaciones.

La Directora de Tesis	**El Director de Tesis**	**La Doctoranda**
Fdo. Dr. María del Mar Pérez Gómez	***Fdo. Dr. Antonio Manuel Rubiño López***	***Fdo. Alicia Fernández Oliveras***

PhD Thesis revised by:

Prof. Dra. Dª. Diana Dudea
Associate Professor
Facultatea de Stomatologie
Universitatea de Medicină şi Farmacie "Iuliu Haţieganu"
Cluj-Napoca, ROMÂNIA

Prof. Dra. Dª. Monica Yamauti
Post-graduate Program in Dentistry
Faculdade de Farmácia, Odontologia e Enfermagem
Univeridade Federal do Ceará
Fortaleza, Ceará, BRASIL

A mi familia

"First you guess. Don't laugh, this is the most important step.
Then you compute the consequences. Compare the consequences to experience.
If it disagrees with experience, the guess is wrong.
In that simple statement is the key to science. It doesn't matter how beautiful your guess is or how smart you are or what your name is.
If it disagrees with experience, it's wrong. That's all there is to it."
Richard Feynman

AGRADECIMIENTOS

Quisiera expresar mi agradecimiento a los sucesivos equipos que han dirigido el Departamento de Óptica de la Universidad de Granada desde el año 2005, en el que recibí mi primera beca de investigación, por poner a disposición de mi formación sus infraestructuras y recursos materiales y humanos.

Al responsable del Grupo de Óptica de Granada FQM 151 del Plan Andaluz de Investigación de la Junta de Andalucía, el Dr. Enrique F. Hita Villaverde, por el respaldo y la financiación proporcionados desde mi incorporación al grupo en el año 2007.

Al Vicerrectorado de Política Científica e Investigación de la Universidad de Granada, por concederme una beca de Formación de Investigadores en 2008.

Al Ministerio de Ciencia e Innovación de España, por la beca de Formación del Profesorado Universitario (FPU) que ha avalado mi formación doctoral desde el año 2009.

Obrigada ao Departamento de Física da Universidade do Minho, por me dar a oportunidade de conhecer, aprender e colaborar com os grandes professores, pesquisadores e grandes pessoas.

Um agradecimento especial ao Dr. Manuel Filipe M. Costa, por sua hospitalidade, por compartilhar sua experiência comigo, por contribuir significativamente para a minha profissional creecimiento e por estar sempre pessoa tão atenciosa.

Thanks to Dr. Scott A. Prahl for stimulating discussions and helpful suggestions along with help in the measurement automation and supervision of one of the setups used in this Thesis.

To Mr. David Nesbitt for his efficient revisions of the English texts and to Miss Natasha Phillips for guiding me in discovering the sound of my written words.

Gracias a mis compañeros de grupo por sus valiosas colaboraciones.

A todos los miembros del Departamento de Óptica de la Universidad de Granada por acogerme tan bien desde siempre y, especialmente, a los que han sido mis profesores, porque esta tesis doctoral también es fruto de sus enseñanzas.

A mis directores de tesis, la Dra. María del Mar Pérez Gómez y el Dr. Antonio Manuel Rubiño López, por el tiempo y esfuerzo invertido en mi proyecto doctoral y, sobre todo, por el privilegio que supone trabajar con la libertad que ellos me han otorgado en todo momento.

A mis padres, Jesús y María Luisa, y a mi hermana, Paz, por su apoyo incondicional, su ayuda siempre desinteresada y su inconmensurable paciencia. Porque sin ellos jamás habría terminado mis estudios de Licenciada en Física y Diplomada en Óptica y Optometría obteniendo sendos Premios Extraordinarios de la Universidad de Granada. Porque sin ellos nunca habría sido realidad esta tesis doctoral. Porque ellos son para mí, por sus trayectorias vitales, los mejores exponentes de excelencia personal y profesional.

CONTENTS

INTRODUCCIÓN

PROPIEDADES OPTICAS Y RUGOSIDAD

La propagación de la luz en medios biológicos se caracteriza mediante los coeficientes de absorción y esparcimiento, la función de fase de esparcimiento, el índice de refracción y las condiciones de la superficie (rugosidad). Las propiedades de la superficie están íntimamente ligadas a las propiedades ópticas, pues la forma en la que la luz es reflejada depende no solo de la composición del material sino también de su microestructura.

En Odontología, la sustitución de restauraciones dentales se debe en gran medida a fallos estéticos. Obtener una restauración estética supone que las propiedades ópticas del material de restauración se ajustan a las de los dientes naturales. Dichas propiedades ópticas vienen determinadas por los fenómenos de absorción y esparcimiento de la luz que se producen tanto en la superficie del material como en su interior.

Algunas de las principales propiedades que determinan la apariencia de los materiales de restauración dental dependen del esparcimiento de la luz, como es el caso del color y la translucidez [1, 2]. Más del 80% de los pacientes declaran encontrar diferencias de color y de apariencia entre la restauración dental y sus dientes naturales [3]. Una superficie rugosa en un diente restaurado no solo tiene implicaciones en su apariencia provocando, por ejemplo, tinciones en la superficie, sino que también incrementa la penetración de bacterias y la retención de placa. Como consecuencia de ello, el riesgo de caries y de inflamación gingival aumenta [4]. Por consiguiente, mantener lisa la superficie en una restauración dental es fundamental para su éxito [5].

Entre los métodos basados en la resolución de la ecuación de transporte radiativo, el método de Adición-Duplicación Inversa, en inglés *Inverse Adding-Doubling* (*IAD*), es una alternativa para determinar las propiedades ópticas. La combinación del método *IAD* con simulaciones de Monte Carlo permite una determinación más precisa de las propiedades ópticas que la teoría de Kubelka Munk [6-8], empleada con anterioridad de forma generalizada por su simplicidad. Ello es debido a que el método *IAD* permite determinar separadamente la absorción y el esparcimiento con una alta precisión. Esto es algo que no proporcionan los coeficientes de absorción y esparcimiento de Kubelka Munk (*K* y *S*), puesto que en *S* hay contribuciones de los coeficientes de absorción y esparcimiento de la ecuación de transporte (μ_a y μ'_s = $(1-g)$). Por esta misma razón, la teoría de Kubelka Munk no proporciona forma de distinción alguna entre el esparcimiento y su dirección.

La teoría de Kubelka-Munk [9] describe la propagación de la luz difusa a través de una muestra isotrópica, considerando el flujo producido solo en dos direcciones. La ventaja de esta teoría es que sus coeficientes de absorción y esparcimiento se pueden expresar de forma sencilla en función de la reflectancia y la transmitancia de la muestra. Sin embargo, estos coeficientes no se relacionan de forma directa con las propiedades ópticas del medio. Dado que la teoría de Kubelka-Munk no proporciona una conexión explícita entre sus coeficientes y las propiedades ópticas, como sí ocurre en los métodos basados en la ecuación de transporte radiactivo, diversos autores estudiaron las relaciones entre *S* y *K* y los coeficientes de absorción y esparcimiento de la ecuación de transporte radiativo [10, 11]. En dichos trabajos se establecieron las siguientes relaciones:

$$K = 2\mu_a \qquad (1)$$

$$S = -x\mu_a + \frac{3}{4}\mu'_s \qquad (2)$$

Algunos autores consideran que puede tomarse $x = 0$ [12], pero ni siquiera con esta consideración el análisis de la anisotropía del esparcimiento es viable. En cambio, empleando el método *IAD*, el esparcimiento y su dirección se pueden analizar separadamente a través del coeficiente de esparcimiento (μ_s) y del factor de anisotropía de esparcimiento (*g*). Conjuntamente, el uso de simulaciones de Monte Carlo minimiza los errores sistemáticos teniendo en cuenta la geometría de medida, las pérdidas en los bordes y la dependencia espectral del índice de refracción. Además, conociendo los valores de μ_a, μ_s y g, el color puede evaluarse a partir de simulaciones de la reflectancia sin necesidad de medidas adicionales [13-15]. El método *IAD* combinado con simulaciones de Monte Carlo ha sido ampliamente utilizado para estudiar medios turbios y biológicos [16-21]. Por ello, se espera que dicho método sea adecuado para el análisis de biomateriales.

La evaluación de las características rugométricas de las superficies se limita habitualmente a la valoración de la rugosidad media (R_a) y, a lo sumo, de la desviación cuadrática media (R_q), sin considerar que estos valores no incluyen información relevante que proporcionan otros parámetros relacionados con la superficie. Tal es el caso del tercer y el cuarto momento con respecto a la media de la distribución superficial de alturas, también denominados asimetría y curtosis, respectivamente (R_{sk} y R_{ku}). Por ejemplo, la asimetría permite distinguir dos perfiles de elevación superficiales que tengan los mismos valores de R_a y R_q pero distinta forma, y la evaluación conjunta de R_{sk} y R_{ku} permite determinar si la distribución superficial de alturas es una distribución normal [22].

En el ámbito de la Odontología, se suele estudiar únicamente el valor de R_a, obtenido tradicionalmente a partir de medidas realizadas con perfilómetros y otros dispositivos de contacto [23–28]. Sin embargo, con los requerimientos actuales, se impone el uso de técnicas no invasivas y la inspección perfilométrica resulta insuficiente.

El creciente rango de tipos de superficies, limitaciones de medida y requerimientos de tolerancia han motivado un gran esfuerzo investigador encaminado a desarrollar distintos métodos, sistemas y técnicas metrológicas para la evaluación rugométrica. En este sentido, los métodos ópticos tienen un papel preponderante en la inspección no invasiva de superficies. Entre estos métodos, los basados en triangulación óptica han alcanzado un estatus elevado debido a su flexibilidad, fiabilidad y robustez.

Durante mucho tiempo, la triangulación óptica ha demostrado ser una herramienta de gran valor para la evaluación microtopográfica de superficies en el ámbito industrial y en el científico [29]. Aunque el principio básico de la medida de distancias por triangulación óptica no es reciente, con el paso del tiempo se han ido optimizando los sistemas destinados a la evaluación y el control de calidad de las superficies. Estas mejoras también han motivado aplicaciones a nuevos campos, como es el caso de las Ciencias de la Salud [30, 31]. En particular, se ha comprobado que la inspección microtopográfica basada en triangulación óptica proporciona información valiosa a la hora de evaluar la calidad de la reducción interproximal de esmalte (una técnica ampliamente utilizada en Odontología para solucionar problemas de espacio entre piezas dentales, a fin de mejorar la oclusión o el alineamiento de los dientes evitando la extracción).

La recopilación de los parámetros ópticos y de rugosidad puede potenciar el desarrollo de aplicaciones útiles para la práctica clínica, como técnicas y tratamientos basados en el uso de fuentes láser. Por otra parte, estos datos pueden contribuir al avance de modelos de cálculo en los que se base la optimización de nuevas composiciones de biomateriales. Por ejemplo, en el futuro, la determinación de los parámetros ópticos y de rugosidad podría implementarse junto al desarrollo de nuevos biomateriales dentales. Esto permitiría realizar, entre las composiciones experimentales y materiales disponibles de propiedades conocidas, comparaciones que condujesen a composiciones de los materiales cada vez más adecuadas.

BIOMATERIALES DENTALES: RESINAS DE COMPOSITE Y CERÁMICAS DE ZIRCONIA

Resinas de composite

La búsqueda de materiales de restauración dental que imiten la apariencia y las propiedades de los dientes naturales se inicia con la historia de la Odontología. Sin embargo, hasta el siglo XX no se dispuso de materiales dentales verdaderamente estéticos. En 1958 R.L. Bowen empezó a experimentar con resinas epóxicas y acrílicas, utilizando, además, partículas de relleno como refuerzo. Este trabajo [32] culminó con el desarrollo de la molécula de bisfenol A diglicidiléter dimetacrilato (Bis-GMA), comúnmente denominado Bis-GMA. El Bis-GMA es la base de las resinas de composite actuales, con las cuales se inicia la Odontología Estética moderna.

Si bien también pueden emplearse en la sustitución de dentina, las resinas de composite se emplean mayoritariamente para restauraciones que afectan al esmalte dental.

Básicamente, las resinas de composite dentales contienen, al menos dos componentes distintos: la matriz orgánica o fase continua y partículas inorgánicas de relleno o fase dispersa. Además se incluye un agente de acoplamiento o fase de enlace que permite la unión entre las partículas de relleno y la matriz de orgánica [33].

La matriz orgánica está compuesta por monómeros orgánicos disfuncionales que al reaccionar entre sí forman macromoléculas denominadas polímeros. El proceso de transformación de los monómeros en polímeros se denomina polimerización o fotopolimerización. Al material también se incorporan otros componentes, tales como fotoactivadores (para la polimerización) y pigmentos colorantes (para el control de las características estéticas).

En la actualidad, la fase continua de la mayoría de las resinas de composite se compone de dimetracrilatos como: el bisfenol A diglicidiléter dimetacrilato (Bis-GMA), el bisfenol A polietilenglicol diéter dimetacrilato (Bis-EMA), el dimetacrilato de uretano (UDMA), el dimetacrilato de trietilenglicol (TEGDMA) o dimetacrilatos modificados.

La matriz orgánica representa entre el 30% al 80% del volumen total del material. A pesar de que la molécula de Bis-GMA es ampliamente usada y presenta grandes ventajas, una de sus mayores limitaciones radica en la contracción volumétrica que presenta durante la polimerización (de entre el 2% y el 14%). Esta reducción volumétrica contribuye al desarrollo de tensiones de polimerización que a menudo conducen a fallos adhesivos, microfracturas y caries de recidiva [34].

Con el objetivo de obtener una menor contracción, alta reactividad y biocompatibilidad, se introdujo un nuevo anillo catiónico en el sistema de monómeros, denominado Silorane [35]. Este nombre deriva de la combinación de los nombres de sus principales componentes químicos: silanos y oxiranos (óxido de etileno). La investigación desarrollada ha demostrado que respecto a las pruebas de citoxicidad son similares o incluso presentan mejores resultados que los monómeros dentales de metacrilatos [36, 37]. Sin embargo, las resinas de silorane muestran inferiores valores del parámetro de translucidez (*translucency parameter*, *TP*) que las resinas de dimetacrilatos tanto antes como después de la polimerización. Esto puede explicarse por el hecho de que las resinas de silorane cormercializadas estaban destinadas a restauraciones de piezas dentales posteriores, lo cual limita su uso en clínica [38].

En las últimas décadas, las investigaciones y los avances en las resinas de composite dentales se han desarrollado básicamente en lo que respecta a la fase inorgánica dispersa, ya que ésta es responsable en gran medida de las propiedades físicas del material. Ello ha dado lugar a que sean precisamente las características de dicha fase (tipo, tamaño, fracción volumétrica y morfología de la partícula de relleno) las que permitan clasificar los distintos tipos de composites disponibles en la actualidad.

Las partículas de relleno proporcionan estabilidad dimensional a la matriz orgánica, mejorando las propiedades mecánicas del material sin perder las ventajas aportadas por la matriz orgánica. Introduciendo esta fase en el material, se consigue aumentar la dureza y la resistencia a la fractura, así como mejorar la resistencia a la compresión y a la abrasión. Por otro lado, se logra reducir la contracción de polimerización, la absorción de agua y el coeficiente de expansión térmica.

En la actualidad, los rellenos más comunes están compuestos de: sílice aglomerado y altamente dispersado, vidrios de sílice con bario o estroncio, fluoruro de iterbio, cuarzo cristalino, óxidos de zirconia, silicatos de aluminio y bario o silicatos de aluminio y litio. El tamaño de las partículas de relleno se regula a través de diferentes procesos de fabricación, tales como pulverización, trituración o molido.

El tamaño de partícula de relleno en es el criterio más empleado para la clasificación de las resinas de composite dentales. Según este criterio, se pueden encontrar los siguientes tipos de resinas de composite [39, 40]:

- Composites de macrorrelleno: las partículas tienen un tamaño que oscila entre 10 y 80 μm y representan un 70-80% del peso o un 60-70% del volumen del material. Son las primeras que se desarrollaron y poseen unas características mecánicas adecuadas, pero sus deficientes cualidades estéticas hacen que hoy estén en desuso.

- Composites de microrrelleno: se caracterizan por presentar un relleno de sílice pirolítico que puede ser fraccionado en partículas cuyo tamaño oscila entre 0,007 y 0,115 μm, con un promedio de 0,04 μm. Se consideran altamente estéticos y presentan un excelente pulido.

- Composites híbridos (figura I.1): con su desarrollo se pretendió aunar las ventajas de los dos tipos de resinas anteriores, es decir, excelentes cualidades mecánicas y estéticas. El tamaño de partícula varía entre 0,4 y 3,0 μm, con un valor medio de 0,7 μm. Sus buenas cualidades mecánicas permitían su uso en reparaciones posteriores.

- Composites de nanorrelleno o nanocomposites (figura I.1): contienen partículas de relleno de tamaños inferiores a 10 nm. Estas partículas se disponen individualmente o agrupadas en agregados, denominados nanoclústeres, de 75 nm de tamaño aproximado.

Tabla 1. Tipos y características del relleno en distintas resinas de composite dentales (datos proporcionados por los fabricantes).

Tipo de relleno	Nanocomposite	Híbrido	Híbrido	Supraesférico
Nombre comercial	Filtek Supreme XT	Tetric EvoCeram	Z250	Estelite Omega
Tamaño de partícula	5 - 20 nm (nanoclústeres: 0,6 – 1,4 μm)	0,04 – 3 μm (media: 0,550 μm)	0,01 – 3,5 μm	0,200 μm
Fracción de volumen (%)	58 - 60	53 - 55	60	78
Fracción de peso (%)	78,5	82-83	82	82

En los últimos años la nanotecnología se ha empleado para generar nuevos biomateriales para aplicaciones en distintas áreas de la Medicina y afines, como es el caso de la restauración dental en Odontología. A cualquier material utilizado para reemplazar tejidos se le exige que, en condiciones ideales, además de biocompatibilidad, presente unas cualidades físicas similares a los tejidos reemplazados.

En este sentido, una de las más significativas contribuciones de la nanotecnología en el campo de la Odontología ha sido, precisamente, la generación de los llamados nanocomposites [41]. Estos materiales se han desarrollado a partir de combinaciones de la matriz orgánica de las resinas tradicionales (dimetraquilatos) con nanopartículas de sílice dispersado (nanorrelleno). Con ello se ha pretendido optimizar las características ópticas y mecánicas del material, reduciendo la contracción de polimerización.

Para preparar esta clase de resinas de composite se han sintetizado partículas nanométricas, esencialmente sílice u óxido de zirconia. Las nanopartículas son tratadas con agentes de acoplamiento de silano que les permiten estar unidas a la matriz orgánica cuando el material es fotopolimerizado. Los nanómeros se sintetizan a partir partículas del mismo tamaño y, debido a esto, aunque se utilicen para conformar materiales compuestos altamente cargados, las propiedades reológicas podrían insuficientes. Para superar esta desventaja, se ha dado lugar a que las nanopartículas de relleno se agrupen formando nanoclústeres, en los que dichas partículas mantienen su forma individual. Los nanoclústeres son óxidos nanoméricos sintetizados ligeramente para formar grupos de partículas con una distribución de tamaños controlada.

Mediante el uso de la teoría de Kubelka-Munk [9], trabajos recientes [42] han encontrado que para nuevos materiales de restauración dental (resinas de silorane y nanocomposites) el esparcimiento prevalece frente a la absorción para longitudes de onda por encima de los 450 nm y la transmitancia aumenta con la longitud de onda, a partir de 420 nm.

En los nanocomposites, el hecho de que el tamaño de las partículas sea menor que el de las longitudes de onda del espectro visible provee la oportunidad de desarrollar materiales altamente translúcidos. Si bien se ha comprobado la mejora en algunas propiedades mecánicas de estos biomateriales, aún es necesario profundizar en el análisis de sus propiedades ópticas.

Cerámicas de zirconia

En los últimos años, se ha desarrollado un número creciente de materiales cerámicos que pueden ser utilizados en Odontología sin necesidad de emplear infraestructuras metálicas. Dado que permiten una mayor transmisión de la luz, con estos materiales se puede obtener un modelo estético difícil de imitar por otros materiales empleados en restauraciones que afectan a la dentina.

Entre estos biomateriales, que han dado lugar a las denominadas restauraciones estéticas de cerámica pura, se encuentra los sistemas de cerámica de zirconia. Con cada uno de estos materiales cerámicos se utiliza un enfoque diferente para intentar mejorar las cualidades estéticas sin causar perjuicio a sus propiedades mecánicas.

El dióxido de zirconio (ZrO_2) es un óxido cristalino blanco. Se obtiene como un polvo blanco que posee propiedades ácidas y básicas y, a temperatura normal, presenta una estructura cristalina hexagonal compacta. Su uso como biomaterial es interesante debido a su resistencia mecánica y química, a su estabilidad dimensional y a su módulo elástico similar al acero inoxidable [43, 44]. Aunque es uno de los óxidos cerámicos más empleados en restauración dental debido a sus excelentes propiedades mecánicas, existe controversia sobre su comportamiento óptico, concretamente, sobre si puede considerarse un material translúcido u opaco. Por otro lado, el uso de colorantes le permite lograr colores semejantes a la estructura dentaria, favoreciendo su integración cromática.

La zirconia estabilizada, en inglés *partially stabilized zirconia* (*PSZ*), es una mezcla de polimorfos de zirconia que se obtiene al añadir óxido cúbico en fase de formación (estabilizador). Agregar una cantidad pequeña de este estabilizador a la zirconia pura produce una estructura de fase tetragonal a una temperatura mayor a 1000ºC y una mezcla de fases cúbica, monoclínica y tetragonal, a una temperatura menor [43-45].

Se pueden agregar diversos óxidos para estabilizar las fases tetragonal y/o cúbica, por ejemplo: óxido de magnesio (MgO), óxido de itrio o itria (Y_2O_3), óxido de calcio (CaO) y óxido de cerio (Ce_2O_3). Cualquiera de estos óxidos genera un material multifásico a temperatura ambiente, conocido como zirconia policristalina tetragonal, en inglés *tetragonal zirconia polycrystal* (*TZP*). La microestructura de este material a temperatura ambiente generalmente consiste en zirconia cúbica (fase mayor) con precipitados de zirconia tetragonal y monoclínica (fase menor). Estos precipitados pueden existir como granos fronterizos o dentro de los granos cúbicos de la matriz [43-46].

Garvie y Nicholson demostraron que se mejoró la resistencia mecánica de la *PSZ* debido a la distribución fina y homogénea de la fase monoclínica dentro de la matriz cúbica [47]. El desarrollo de la zirconia como material de ingeniería estuvo marcado por el aporte de trabajos [48] que demostraron cómo obtener la mejor transformación de las fases tetragonal a monoclínica (T→M) para lograr mejorías en la resistencia mecánica y la dureza de la *PSZ*. Los autores observaron que los precipitados tetragonales metaestables finamente dispersos dentro de la matriz cúbica eran capaces de transformarse en precipitados monoclínicos cuando se aliviaba la fuerza ejercida sobre ellos por la matriz.

Por ejemplo, en el avance de una grieta sobre el material, el campo de fuerza asociado con la expansión (debido a la transformación de fases) actúa en contra del campo de fuerza que promueve la propagación de la grieta. Con esto se logra una mayor dureza del material debido a que la energía asociada con la propagación de la grieta se disipa, tanto en la transformación de fases T→M como en superar la fuerza de compresión generada por el aumento de volumen menor [43, 44, 50].

Se puede lograr el desarrollo de los precipitados tetragonales por la adición de alrededor de un 8mol% de MgO al ZrO_2. Esto permite la formación de una microestructura totalmente cúbica a 1800°C y la nucleación dentro de la matriz de la fase tetragonal metaestable durante el enfriamiento y envejecimiento. Las cerámicas *PSZ* se pueden obtener también en el sistema ZrO_2-Y_2O_3, en el que también es posible obtener cerámicas que a temperatura ambiente presentan sólo fase tetragonal.

La zirconia policristalina tetragonal estabilizada con itria (*Y-TZP*) contiene aproximadamente 2-3mol% de itria y está compuesta por granos tetragonales con tamaños del orden de 100 nm. Debido a sus excelentes propiedades mecánicas, las cerámicas *Y-TZP* se tienen un amplio rango de aplicaciones clínicas.

La zirconia policristalina tetragonal estabilizada con itria 3mol% (*3Y-TZP*) contiene un 3mol% de itria como estabilizador y es la cerámica de zirconia de mayor uso biomédico. En Odontología se emplea para la fabricación de pilares para implantes, coronas dentales y dentaduras parciales fijas [51]. Las restauraciones se fabrican por un fresado suave de bloques presinterizados y una posterior sinterización a altas temperaturas, o por un fresado rígido de bloques completamente sinterizados [45, 50].

En la fabricación de los bloques de *3Y-TZP*, normalmente, los polvos utilizados tienen un aglutinante que hacen al material apto para el prensado. También contienen alrededor del 2% en peso de HO_2 (tradicionalmente difícil de separar del ZrO_2). Estos polvos tienen variaciones pequeñas en su composición química y consisten en aglomerados secados por aspersión obtenidos a partir de cristales mucho más pequeños.

Los bloques son fabricados mediante un prensado frío isostático y el aglutinante es eliminado posteriormente con un tratamiento de calor previo al sinterizado. Las condiciones de este proceso deben ser controladas cuidadosamente por el fabricante, sobre todo la velocidad de calentamiento y la temperatura del presinterizado.

Si la velocidad de calentamiento es muy rápida, la eliminación del aglutinante y los productos asociados podría generar grietas en los bloques, por lo que se prefieren velocidades de calentamiento más lentas [52]. La elección de una adecuada temperatura de presinterización de los bloques es un aspecto crítico, pues dicha temperatura afecta a la dureza y al fresado del material. Estas dos características actúan en direcciones opuestas: se necesita una adecuada dureza para el manejo de los bloques pero, si la dureza es muy alta, puede ser perjudicial para el fresado.

El fresado es mejor si se realiza en dos pasos. Por ello, se hace primero un fresado brusco a una velocidad de avance baja y luego un fresado fino a una velocidad mayor [52]. La temperatura de presinterización también afecta a la rugosidad de los bloques, de modo que temperaturas globales mayores generan superficies más rugosas.

La sinterización de las restauraciones fresadas tiene que ser cuidadosamente controlada, utilizando hornos programados y respetando las condiciones que dan los fabricantes. Las temperaturas finales alcanzadas suelen estar entre los 1350 y 1550ºC con tiempos de permanencia de 2 a 5 horas. Estas variaciones en las condiciones de sinterización se deben a la distinta composición química inicial del polvo de *3Y-TZP*. Por ejemplo, adicionar cantidades pequeñas de alúmina actúa favorablemente en la sinterización, permitiendo el uso de temperaturas de sinterización más bajas y tiempo menores.

Las temperaturas y tiempos de sinterización son determinantes en la obtención del tamaño del grano del producto final y en su posterior estabilidad [50]. Por ejemplo, si las temperaturas de sinterización alcanzan los 1500ºC con un tiempo de sinterización de 5 horas, se ha comprobado que aumenta la cantidad de fase cúbica en la cerámica *3Y-TZP* [53]. La mayor presencia de granos cúbicos es perjudicial para la resistencia de la cerámica *3Y-TZP*, lo cual demuestra la importancia de controlar las condiciones el proceso de sinterización de estos materiales.

El alto índice de refracción y la alta opacidad en el espectro visible de la cerámica de zirconia estabilizada con itria la hacen muy conveniente en ciertas prácticas clínicas relacionadas con estética dental. Por ejemplo, para cubrir infraestructuras metálicas o para enmascarar coloraciones inadecuadas en sustratos y pilares de piezas dentales [45, 46].

En trabajos recientes [54] se ha comparado la translucidez de la dentina y de la zirconia policristalina tetragonal estabilizada con itria, a través de la evaluación del *TP* (diferencia de color entre medidas realizadas sobre un fondo negro y un fondo blanco para una misma muestra).

También se han determinado se han determinado los coeficientes de scatering y absorción de Kubelka-Munk de este tipo de cerámicas concluyéndose que, tras el coloreado y sinterizado, el esparcimiento prevalece frente a la absorción, como se ocurre en los tejidos biológicos [55]. En este sentido, es interesante realizar nuevos estudios que permitan seguir avanzando en el conocimiento de las propiedades ópticas de estos biomateriales.

APORTACIONES MÁS NOVEDOSAS DE LA TESIS DOCTORAL

Teniendo en cuenta este contexto y antecedentes, las contribuciones más novedosas que aportará esta Tesis Doctoral se pueden resumir en los siguientes puntos:

Evaluación de la función de fase de esparcimiento y del factor de anisotropía de esparcimiento, g, a partir de medidas experimentales (no a partir de modelos, simulaciones o aproximaciones teórico-empíricas) en resinas de composite y cerámicas de zirconia para aplicaciones dentales. Comprobación de la idoneidad del método experimental empleado para obtener los valores de g con una precisión tal que permita establecer comparaciones entre materiales y distinciones entre un mismo material en diferentes condiciones (distintos espesores de la muestra y distintas longitudes de onda). Esto se comprueba, incluso, para tejidos dentales humanos (esmalte y dentina).

Determinación de los coeficientes de absorción y esparcimiento (μ_a y μ_s) de resinas de composite y cerámica de zirconia mediante el algoritmo *IAD* a través de la incorporación de valores experimentales del factor de anisotropía de esparcimiento, g, considerando los cambios espectrales de dicho factor y del índice de refracción. Corroboración de la idoneidad del método experimental empleado para obtener los valores de μ_a y μ_s con una precisión que permita analizar comparativamente distintos materiales.

Realización, en condiciones de repetividad, de medidas encaminadas a valorar el efecto de tejidos dentales humanos (esmalte y dentina) y resinas de composite sobre el estado de la luz polarizada, proporcionando la incertidumbre asociada a los ángulos de desviación del plano de polarización.

Evaluación de los principales parámetros de rugosidad (R_a, R_q, R_{sk} y R_{ku}) en resinas de composite y cerámicas de zirconia, -proporcionando información, no sólo sobre la rugosidad media, sino también sobre la distribución superficial de alturas-, mediante el uso de un sistema microtopográfico no invasivo basado en triangulación óptica. Comprobación de la idoneidad de este sistema para obtener los principales parámetros de rugosidad con una precisión tal que permita establecer comparaciones entre materiales y distinciones entre un mismo material en diferentes condiciones (tratamiento superficial en composites y proceso de sinterización en cerámica de zirconia).

Aportación de una información tan relevante como es la incertidumbre asociada a todas y cada una de las magnitudes determinadas experimentalmente (factor de anisotropía, coeficientes de absorción, esparcimiento y atenuación, profundidad de penetración óptica, ángulo de desviación del plano de polarización, parámetros de rugosidad y porcentaje de brillo). Esto constituye una importante novedad pues se obvia de forma generalizada en los trabajos que estudian biomateriales y, concretamente, biomateriales destinados a aplicaciones dentales, de modo que no es posible conocer la precisión de los valores de las magnitudes facilitados, ni en qué medida las comparaciones establecidas se basan de diferencias significativas.

REFERENCIAS

[1] Terry, D.A., Geller, W., Tric, O., Anderson, M. J., Tourville, M. and Kobashigawa, A., “Anatomical form defines color: function, form and aesthetics,” Pract. Proced. Aesthet. Dent. 14(1), 59-67 (2002).

[2] Lee, Y. K., Lim, B. S. and Kim, C.W., “Effect of surface conditions on the color of dental resin composites,” J. Biomed. Mate. Res. 63(5), 657-63 (2002).

[3] Joiner, A., “Tooth colour: a review of the literature,” J Dent. 32(Suppl. 1), 3-12 (2004).

[4] Jefferies, S. R., “The art and science of abrasive finishing and polishing in restorative dentistry,” Dent. Clin. North Am. 42(4), 613-27 (1998).

[5] Joniot, S. B., Grégoire, G. L., Auther, A. M. and Roques, Y. M, “Three-dimensional optical profilometry analysis of surface states obtained after finishing sequences for three composite resins,” Oper. Dent. 25(4), 311-315 (2000).

[6] Yeh, C. L., Miyagawa, Y., and Powers, J. M. “Optical properties of composites of selected shades,” J. Dent. Res. 61, 797-780 (1982).

[7] Grajower, R., Wozniak, W. T. and Lindsay, J. M., “Optical properties of composite resin", J. Oral. Rehab. 9, 389-399 (1982).

[8] Taira, M. Okazaki, M. and Takahashi, J., “Studies on optical properties of two commercial visible-light-cured composite resins by diffuse reflectance measurements,” J. Oral Rehab. 26, 329-337 (1999).

[9] Kubelka, P. and Munk, F., “A contribution to the optics of pigments,” Z. Tech. Phys. 12, 593-601 (1931).

[10] Brinkworth B.J., “Interpretation of the Kubelka-Munk Coefficients in reflection theory,” Appl Opt. 11, 1434 – 1435 (1972).

[11] Star, W.M., Marijnissen, J. P. A. and van Gemert M. J. C., “Light dosimetry in optical phantoms and in tissues: I. Multiple flux and transport theory,” Phys. Med. Biol. 33(4), 437-454 (1988).

[12] Thennadil, S. N., "Relationship between the Kubelka-Munk scattering and radiative transfer coefficients," J. Opt. Soc. Am. A 25, 1480-1485, (2008).

[13] Koblova E. V., Bashkatov, A. N., Dolotov, L. E., Sinichkin, Y. P., Kamenskikh, T. G., Genina, E. A. and Tuchin, V. V., "Monte Carlo modeling of eye iris color," Proc. SPIE 6535, 1 (2006).

[14] Randeberg, L. L. and Svaasand, L. O., "Simulated color: a diagnostic tool for skin lesions like port-wine stain," Proc. SPIE 4244, 1–12 (2001).

[15] Liu, Q. and Ruprecht, E. "Radiative transfer model: matrix operator method," Appl. Opt. 35(21), 4229-4237, (1996).

[16] Svaasand, L. O., Norvang, L. T., Fiskerstrand, E. J., Stopps, E. K. S., Berns, M. W. and Nelson, J. S., "Tissue parameters determining the visual appearance of normal skin and port wine stains," Lasers Med. Sci. 10, 55–65 (1995).

[17] Wang, L., Sharma, S., Aernouts, B., Ramon, H. and Saeys, W., "Supercontinuum laser based double-integrating-sphere system for measuring optical properties of highly dense turbid mediain the 1300-2350 nm region with high sensitivity," Proc. SPIE 8427, 84273B-1-6 (2012)..

[18] Sardar, D. K., Yust, B. G., Barrera, F., Minum, L. C. and Tsin A. T. C., "Optical absorption and scattering of bovine cornea, lens and retina in the visible region," Lasers Med. Sci. 24(6), 839-847 (2009).

[19] Honda, N., Ishii, K., Kimura, A., Sakai, M. and Awazu, K., "Determination of optical property changes by laser treatments using inverse adding-doubling method," Proc. SPIE 7175, 71750Q-1-8 (2009).

[20] Ishii, K., Kimura, A. and Awazu, K., "Optical properties of tissues after laser treatments in the wavelength range of 350 - 1000 nm," Proc. SPIE 6991, 69912F-1-7 (2008).

[21] Chen, Y. C., Ferracane, J. L. and Prahl, S. A., "A pilot study of a simple photon migration model for predicting depth of cure in dental composite," Dent. Mater. 21(11), 1075–1086 (2005).

[22] Gadelmawla, E. S.; Koura, M. M., Maksoud, T. M. A., Elewa I. M. and Soliman, H. H., "Roughness parameters," J. Mater. Process. Technol. 123(1), 133-145 (2002).

[23] da Costa, J.B., Goncalves, F. and Ferracane, J. L., "Comparison of two-step versus four-step composite finishing/polishing disc systems: evaluation of a new two-step composite polishing disc system," Oper Dent. 36(2), 205-212 (2011).

[24] Celik, C. and Ozgünaltay, G., "Effect of finishing and polishing procedures on surface roughness of tooth-colored materials," Quintessence Int.. 40(9), 783-789 (2009).

[25] Paravina, R. D., Roeder, L., Lu, H., Vogel, K. and Powers, J. M., "Effect of finishing and polishing procedures on surface roughness, gloss and color of resin-based composites," Am. J. Dent. 17(4), 262-266 (2004).

[26] Johnson, A., van Noort, R., Hatton, P. V. and Walsh, J. M., "The effect of investment material and ceramming regime on the surface roughness of two castable glass-ceramic materials," Dent. Mater. 19(3), 218-225 (2003).

[27] Kim, I. J., Lee, Y. K., Lim, B. S. And Kim, C. W., "Effect of surface topography on the color of dental porcelain," J. Mater. Sci. Mater. Med. 14(5), 405-409 (2003).

[28] Reis, A. F., Giannini, M., Lovadino, J. R. and Ambrosano, G. M., "Effects of various finishing systems on the surface roughness and staining susceptibility of packable composite resins," Dent. Mater. 19(1), 12-18 (2003).

[29] Costa, M. F. M., "Optical Triangulation-Based Microtopographic Inspection of Surfaces," Sensors 12, 4399-4420 (2012).

[30] Pacheco, M. C. L., Costa, M. F. M., Zapata, A. J. P., Cherit, J. D. and Gallegos, E. R., "Implementation and analysis of relief patterns of the surface of benign and malignant lesions of the skin by microtopography," Phys. Med. Biol. 50, 5535–5543 (2005).

[31] Costa, M. F. M. and Pereira, P. B., "Optical microtopographic inspection of the surface of tooth subjected to stripping reduction," Proc. SPIE 8001, 80012X-1-5 (2011).

[32] Bowen, R. L., "Properties of a silica-reinforced polymer for dental restoration," J. Am. Dent. Assoc. 66, 57-64 (1963).

[33] Fortin, D. and Vargas, M. A., "The spectrum of composites:new techniques and materials," J. Am. Dent. Assoc. 131, 26S-30S (2000).

[34] Soh, M. S., Yap, A. and Sellinger A., "Metacrylate and epoxy functionalized nanocomposites based on silsesquioxane cores for use in dental applications," Europ. Polymer J. 43, 315-327 (2007).

[35] Weinmann, W., Thalacker, C. and Guggenberger, R., "Siloranes in dental composites," Den Mat. 21, 68-74 (2005).

[36] Eick, D., Smith, R., Pinzino, C. and Kostoryz, L., "Stability of silorane dental monomers in aqueous systems," Journal Dent. 34, 405-410 (2006).

[37] Eick, D., Khoh, S., Chappelow, C,. Kilway, K., Giese, O., Glaros, A. and Pinzir, C., "Properties of silorane-hased dental resins and composites

containine a stress-reducing monomer," Dent. Mater. 23, 1011-1017 (2007).

[38] Pérez, M. M., Ghinea, R., Ugarte-Alván, L. I., Pulgar, R. and Paravina, R. D., "Color and translucency in silorane-based resin composite compared to universal and nanofilled composites," J. Dent. 38 Suppl 2, e110-e116 (2010).

[39] dos Santos, G. B., Alto, R. V., Filho, H. R., da Silva, E. M. and Fellows, C. E., "Light transmission on dental resin composites," J. Am. Dent. Mat. 24, 571–576 (2008).

[40] Lim, Y. K, Lee, Y. K., Lim, B. S., Rhee, S. H. and Yang, H. C., "Influence of filler distribution on the color parameters of experimental resin composites," Dent Mater. 24(1), 67-73 (2008).

[41] Mitra, S. B., Wu, D. and Holmes, B. N., "An application of nanotechnology in advanced dental materials," J. Am. Dent. Assoc. 134(10), 1382–1390 (2003).

[42] Ugarte-Alván, L. I., Evaluación óptica de nuevas resinas compuestas: nanocomposites y resinas de silorane, Tesis Doctoral, Universidad de Granada, 2010.

[43] Piconi, C. and Maccauro G., "Zirconia as a ceramic biomaterial," Biomaterials 20(1), 1-25 (1999).

[44] Vagkopoulou, T., Koutayas, S. O., Koidis, P. and Strub, J. R., "Zirconia in dentistry: Part 1. Discovering the nature of an upcoming bioceramic," Eur. J. Esthet. Dent. 4(2), 130-51 (2009).

[45] Kelly, J. R. and Benetti, P., "Ceramic materials in dentistry: historical evolution and current practice,". Aust. Dent. J. 56 Suppl 1, 84-96 (2011).

[46] Vagkopoulou, T., Koutayas, S. O., Koidis, P. and Strub, J. R., “Zirconia in dentistry: Part 1. Discovering the nature of an upcoming bioceramic,” Eur. J. Esthet. Dent. 4(2), 130-51 (2009).

[48] Garvie, R. C. and Nicholson, P. S., “Phase analysis in zirconia systems,” J. Am. Ceram. Soc. 55, 303-305 (1972).

[49] Garvie, R. C., Hannink, R. H. and Pascoe, R. T., “Ceramic steel?” Nature 258, 703 (1975).

[50] Denry I. and Kelly, J. R., “State of the art of zirconia for dental applications,” Dent. Mater. 24(3), 299-307 (2008).

[51] Cavalcanti, A. N., Foxton, R. M., Watson, T. F., Oliveira, M. T., Giannini, M. and Marchi, G. M., “Y-TZP Ceramics: key concepts for clinical application,” Oper Dent 34(3), 344-351 (2009).

[52] Terry, D. A., Leinfelder, K. F. and Geller, W., [Aesthetic & restorative dentistry. Material selection & technique], Everest Publishing Media, Shaniwar Peth, 2009.

[53] Chevalier, J., Deville, S., Münch, E., Jullian, R. and Lair, F., “Critical effect of cubic phase on aging in 3 mol% yttria-stabilized zirconia ceramics for hip replacement prosthesis,” Biomaterials 25, 5539-5545 (2004).

[54] Pecho, O. E., Ghinea, R., Ionescu, A. M., Cardona, J. C., Paravina R. D. and Pérez M. M., “Color and translucency of zirconia ceramics, human dentine and bovine dentine,” J. Dent. 40 Suppl 2, 34e-40e (2012).

[55] Pecho, O. E., Caracterización óptica y estructural de las cerámicas en base a policristales tetragonales de zirconia estabilizados con ytria, Tesis Doctoral, Universidad de Granada, 2012.

Chapter I.

SUMMARISED INTRODUCTION

Light propagation in biological media is characterized by the absorption coefficient, the scattering coefficient, the scattering phase function, the refractive index, and the surface conditions (roughness). The surface properties are intimately related with the optical properties in a material, since the way that light is reflected by the material depends not only on its composition but also on its microstructure.

In dentistry, aesthetic failure is one of the most widespread reasons for restoration replacement. Aesthetic restoration involves a visible match of the optical properties of restorative material and natural teeth. These optical properties are determined by light absorption and scattering by the medium's surface and interior. Some of the main appearance properties of restorative materials, such as the perceived color and translucency, are intimately related with light-scattering properties [I.1, I.2]. More than 80% of patients are reportedly aware of color and appearance differences between the restoration and the adjacent natural teeth [I. 3]. The rough surface of a treated tooth not only affects the appearance, for example superficial staining, but also increases penetration of bacteria and plaque retention. This results in a higher risk of cavities and gingival inflammation [I.4]. Therefore, maintaining the smooth surface of a restoration is of utmost importance for its success [I.5].

Among the methods based on solving the radiative transport theory, the Inverse Adding-Doubling (IAD) algorithm is an alternative for determining optical properties. The combination of the IAD algorithm with the Monte Carlo simulations, leads to a more precise determination of optical properties than the previously used Kubelka Munk theory [I.6-I.8]. This is because the IAD method enables a separate determination of absorption and scattering parts with high precision. This is not provided by the Kubelka Munk absorption and scattering coefficients (K and S), since S is made up of the radiative theory's absorption and scattering coefficients (μ_{a}, μ_s and g). For this same reason, Kubelka Munk theory does not allow any separation between pure scattering and its direction.

In contrast, with the IAD method, scattering can be separated into pure scattering (with the scattering coefficient μ_s) and its direction (with the scattering anisotropy factor g). In addition, the use of Monte Carlo simulations minimizes systematic errors by taking into account the measuring geometry, radiation losses at border lines, and the wavelength dependent refractive index. Moreover, with the knowledge of the μ_a, μ_s and g, color can be evaluated from simulated reflectance values without additional measurements [I.9-I.11]. The IAD method along with inverse Monte Carlo simulations has been broadly used to study biological and turbid media [I.12-I.17]. As a result, its suitability for dental biomaterials is expected.

Optical methods have the most important role for non-invasive inspection of surfaces. The increasing range of surface types, measurement limitations and tolerance requirements has demanded a major research effort in the development of different methods, systems and metrological techniques. The profilometric inspection seems to be insufficient in many instances. Among the optical methods, triangulation-based ones have gained a major status thanks to their flexibility, reliability and robustness. Optical triangulation has for a long time proved to be an invaluable tool for microtopographic evaluation of surfaces in the industrial and scientific fields [I.18]. Successful applications in life sciences have also been performed [I.19, I.20]. Particularly, triangulation-based microtopographic inspection of treated tooth surfaces has proved to provide valuable insights in order to evaluate the quality of dental enamel stripping (a technique widely used in dentistry).

Gathering of optical and roughness parameters may assist the development of potential applications useful for clinical practice, such as laser-based techniques and treatments. Furthermore, this data may allow the advance of other calculation models as a basis for the optimization of new biomaterial composition. For example, in the future, the determination of optical and roughness parameters could be used along with the development of new dental biomaterials. This would allow comparisons between experimental compositions and available materials of known properties, thus revealing the most suitable material compositions.

Currently, dental-resin composites are among the most common and widely used materials for replacing enamel. Dental nano-filled resin composites have recently been introduced [I.21]. Nanotechnology applied to dental composites has provided filler particles that are dramatically smaller, can be dispersed in high concentrations and are polymerized into the resin system with molecules designed to be compatible when coupled with a polymer. Since this molecular manufacturing provides other unique characteristics, optical properties of nanocomposites could differ when compared with those of conventional composites (hybrids and micro-hybrids).

With the intention of avoiding the infrastructure of metallic prostheses, structural ceramics have been improved and progressively more employed in restorative dentistry. One ceramic material currently used to replace dentine in an irreversibly diseased tooth is yttrium cation-doped tetragonal zirconia polycrystal (3Y-TZP). The microstructure of 3Y-TZP ceramics for dental applications consists of small equiaxed grains with diameter sizes depending on the sintering temperature [I.22]. The sintered ceramic for dental applications is fabricated using computer-aided design and manufacturing (CAD/CAM) procedures from pre-sintered zirconia ceramic. This ceramic material arose as a versatile and promising biomaterial because of its good mechanical and biological properties [I.23, I.24]. However, its roughness and optical characterizations have not been completely developed.

The fulfillment of optimal quality and final success in biomedical application of dental-resin composites and zirconia ceramics calls for thorough studies to assess the appropriate material properties.

The following figures show microscope images of the dental biomaterials studied in this PhD thesis and of the dental tissues they are meant to replace.

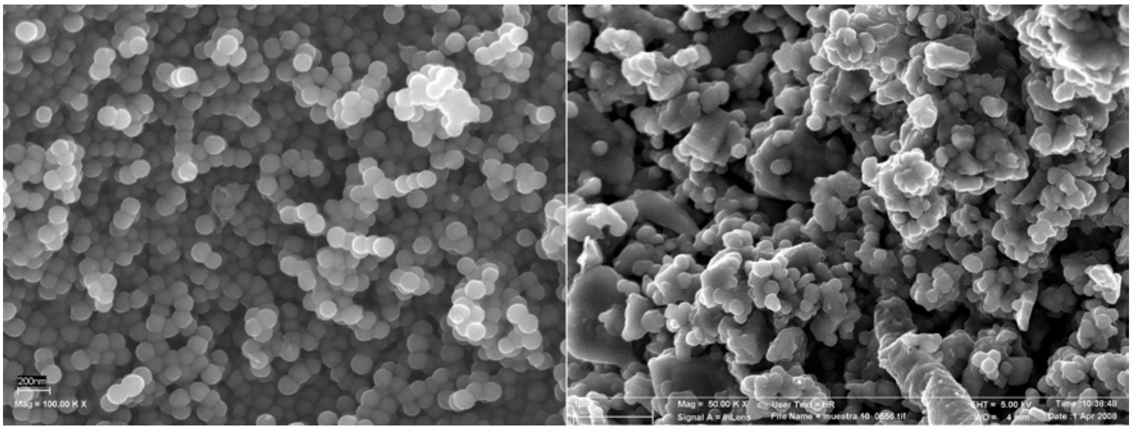

Figure I.1. SEM images of the inorganic fillers of two different types of dental-resin composites: nanocomposite (left) and hybrid (right).

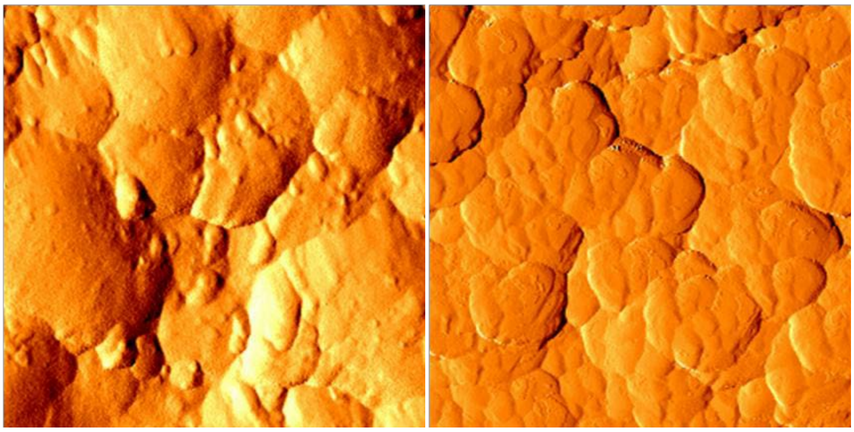

Figure I.2. AFM images of zirconia ceramic: sintered (left) and pre-sintered (right).

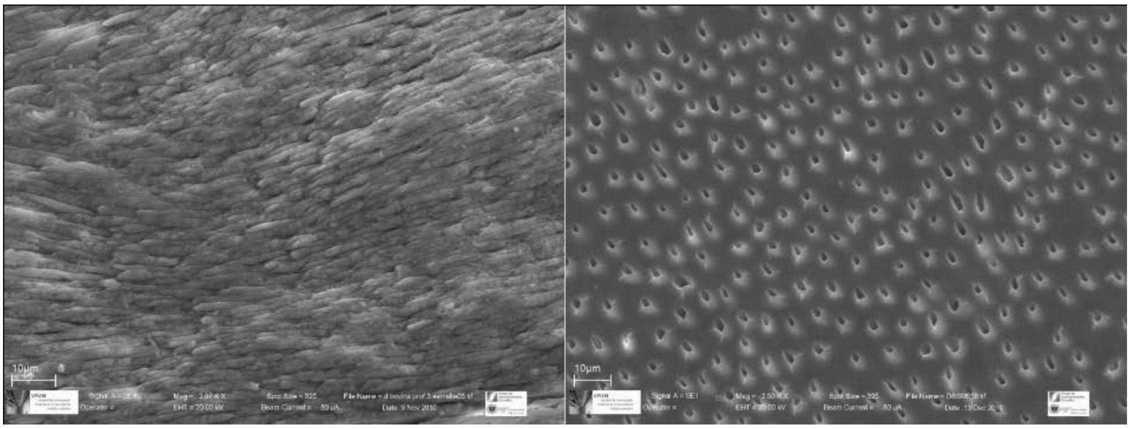

Figure I.3. SEM images of the human dental tissues: enamel (left) and dentine (right).

REFERENCES

[I.1] Terry, D.A., Geller, W., Tric, O., Anderson, M. J., Tourville, M. and Kobashigawa, A., “Anatomical form defines color: function, form and aesthetics,” Pract. Proced. Aesthet. Dent. 14(1), 59-67 (2002).

[I.2] Lee, Y. K., Lim, B. S. and Kim, C.W., “Effect of surface conditions on the color of dental resin composites,” J. Biomed. Mate. Res. 63(5), 657-63 (2002).

[I.3] Joiner, A., “Tooth colour: a review of the literature,” J Dent. 32(Suppl. 1), 3-12 (2004).

[I.4] Jefferies, S. R., “The art and science of abrasive finishing and polishing in restorative dentistry,” Dent. Clin. North Am. 42(4), 613-27 (1998).

[I.5] Joniot, S. B., Grégoire, G. L., Auther, A. M. and Roques, Y. M, “Three-dimensional optical profilometry analysis of surface states obtained after finishing sequences for three composite resins,” Oper. Dent. 25(4), 311-315 (2000).

[I.6] Yeh, C. L., Miyagawa, Y., and Powers, J. M. “Optical properties of composites of selected shades,” J. Dent. Res. 61, 797-780 (1982).

[I.7] Grajower, R., Wozniak, W. T. and Lindsay, J. M., “Optical properties of composite resin", J. Oral. Rehab. 9, 389-399 (1982).

[I.8] Taira, M. Okazaki, M. and Takahashi, J., “Studies on optical properties of two commercial visible-light-cured composite resins by diffuse reflectance measurements,” J. Oral Rehab. 26, 329-337 (1999).

[I.9] Koblova E. V., Bashkatov, A. N., Dolotov, L. E., Sinichkin, Y. P., Kamenskikh, T. G., Genina, E. A. and Tuchin, V. V., “Monte Carlo modeling of eye iris color,” Proc. SPIE 6535, 1 (2006).

[I.10] Randeberg, L. L. and Svaasand, L. O., “Simulated color: a diagnostic tool for skin lesions like port-wine stain,” Proc. SPIE 4244, 1–12 (2001).

[I.11] Liu, Q. and Ruprecht, E. “Radiative transfer model: matrix operator method,” Appl. Opt. 35(21), 4229-4237, (1996).

[I.12] Svaasand, L. O., Norvang, L. T., Fiskerstrand, E. J., Stopps, E. K. S., Berns, M. W. and Nelson, J. S., “Tissue parameters determining the visual appearance of normal skin and port wine stains,” Lasers Med. Sci. 10, 55–65 (1995).

[I.13] Wang, L., Sharma, S., Aernouts, B., Ramon, H. and Saeys, W., “Supercontinuum laser based double-integrating-sphere system for measuring optical properties of highly dense turbid mediain the 1300-2350 nm region with high sensitivity,” Proc. SPIE 8427, 84273B-1-6 (2012)..

[I.14] Sardar, D. K., Yust, B. G., Barrera, F., Minum, L. C. and Tsin A. T. C., “Optical absorption and scattering of bovine cornea, lens and retina in the visible region,” Lasers Med. Sci. 24(6), 839-847 (2009).

[I.15] Honda, N., Ishii, K., Kimura, A., Sakai, M. and Awazu, K., “Determination of optical property changes by laser treatments using inverse adding-doubling method,” Proc. SPIE 7175, 71750Q-1-8 (2009).

[I.16] Ishii, K., Kimura, A. and Awazu, K., “Optical properties of tissues after laser treatments in the wavelength range of 350 - 1000 nm,” Proc. SPIE 6991, 69912F-1-7 (2008).

[I.17] Chen, Y. C., Ferracane, J. L. and Prahl, S. A., “A pilot study of a simple photon migration model for predicting depth of cure in dental composite,” Dent. Mater. 21(11), 1075–1086 (2005).

[I.18] Costa, M. F. M., “Optical Triangulation-Based Microtopographic Inspection of Surfaces,” Sensors 12, 4399-4420 (2012).

[I.19] Pacheco, M. C. L., Costa, M. F. M., Zapata, A. J. P., Cherit, J. D. and Gallegos, E. R., “Implementation and analysis of relief patterns of the surface of benign and malignant lesions of the skin by microtopography,” Phys. Med. Biol. 50, 5535–5543 (2005).

[I.20] Costa, M. F. M. and Pereira, P. B., “Optical microtopographic inspection of the surface of tooth subjected to stripping reduction,” Proc. SPIE 8001, 80012X-1-5 (2011).

[I.21] Mitra, S. B., Wu, D. and Holmes, B. N., “An application of nanotechnology in advanced dental materials,” J. Am. Dent. Assoc. 134(10), 1382–1390 (2003).

[I.22] Denry I. and Kelly, J. R., “State of the art of zirconia for dental applications,” Dent. Mater. 24(3), 299-307 (2008).

[I.23] Piconi, C. and Maccauro G., “Zirconia as a ceramic biomaterial,” Biomaterials 20(1), 1-25 (1999).

[I.24] Chevalier J. and Gremillard, L., “Ceramics for medical applications: A picture for the next 20 years,” J. Eur. Ceram. Soc. 29(7), 1245-1255 (2009).

Chapter II.

MOTIVATION AND OBJECTIVES

Currently, obtaining biomaterials capable of replacing tissue is an issue that arouse widespread interest in society and on which an important part of the international scientific community is concentrating its efforts. The implementation of treatments that use new generation biomaterials happens, no doubt, by the prior accomplishment of studies to analyze the behavior and the actual characteristics of these materials. The results of such studies will condition, to a large extent, the success of future applications to be carried out in the biomedical field. Before they can be developed to their full potential, it is essential to know in detail how the materials already being generated are and how they behave.

In order to deepen the knowledge of new biomaterials it is vital to study their optical properties, even if the main function of the restored tissue is not visual. For example, comprehension of laser radiation propagation in these materials is crucial to establish the effects of many current treatments, which are based on tissue irradiation with laser sources. The latest harmless diagnostic techniques also have their foundation in the optical response of biological media. In fact, for the future development of therapeutic and diagnostic applications, it is imperative to know the relationships between optical and biological properties of tissues and, thus, of biomaterials.

Therefore, the present Thesis pursues the next goals:

Main objective:

To apply optical methods to characterize biomaterials used in dentistry for substitution of dental tissues (dentine and enamel), such as zirconia ceramic and dental-resin composites.

Specific objectives:

1.-Perform measurements for precise determination of the scattering anisotropy values of dental biomaterials. Comparatively analyze the behavior showed by the scattering anisotropy in these biomaterials and in the tissues that they are meant to replace.

2.-Apply the IAD algorithm to achieve precise values of the absorption and scattering coefficients of the dental biomaterials, using the scattering anisotropy factor values previously obtained.

3.-Perform measurements to evaluate the effect of dental biomaterials on the polarized light state.

4.-Complete a microtopographic non-invasive inspection to evaluate with precision the main roughness parameters of the biomaterials by means of an optical triangulation system. Complement the information about roughness with specular gloss measurements.

The subsequent contents of this PhD thesis are structured as follows: Each chapter between III and VI corresponds to one of the specific objectives pursued. Each of these chapters includes the state of the art, the methodology, the materials analyzed, the results obtained, their discussion and the references quoted. In chapter VII the final conclusions are gathered and chapter VIII contains the publications due to the work developed in the present Thesis. Finally, chapter IX is dedicated to the funding sources that have made this work possible.

The following table shows the relationship between the specific objectives, the chapters of this Thesis and the scientific publications included in the database *Web of Science* produced by the *Institute for Scientific Information (ISI).*

Table II.1. Relationship between specific objectives, chapters and publications included in the database *Web of Science,* of the *Institute for Scientific Information (ISI).*

Specific objective	Chapter	Publications in *Web of Science (ISI).*
1.- Perform measurements for precise determination of the scattering anisotropy values in dental biomaterials. Comparatively analyze the behavior showed by the scattering anisotropy in these biomaterials and in the tissues that they are meant to replace.	III	Fernández-Oliveras, A., Rubiño M. and Pérez M. M., "Scattering anisotropy measurements in dental tissues and biomaterials". J. Eur. Opt. Soc.-Rapid Publ. 7, 12016-1-12016-8 (2012). Fernández-Oliveras, A., Pecho, O. E., Rubiño, M. and Pérez, M. M., "Measurements of scattering anisotropy in dental tissue and zirconia ceramic". Proc. SPIE 8427, 84272C-1-6 (2012). Fernández-Oliveras, A., Carrasco, I. M., Ghinea, R., Pérez, M. M. and Rubiño, M., "Comparison between experimental and computational methods for scattering anisotropy coefficient determination in dental-resin composites". Proc. SPIE 8427, 84272B-1-7 (2012).
2.- Apply the IAD algorithm to achieve precise values of the absorption and scattering coefficients of the dental biomaterials including the scattering anisotropy factor values previously obtained.	IV	Fernández-Oliveras, A., Rubiño M. and Pérez M. M., "Scattering and absorption properties of biomaterials for dental restorative applications". Submitted (2013). Fernández-Oliveras, A., Rubiño M. and Pérez M. M., "Determination of optical properties in dental restorative biomaterials using the inverse-adding-doubling method". Proc. SPIE, In press (2013).
3.- Accomplish measurements for evaluating the effect of dental biomaterials on the polarized light state.	V	Fernández-Oliveras, A., Pecho, O. E., Rubiño, M. and Pérez, M. M., "Measurements of optical polarization properties in dental tissues and biomaterials". Proc. SPIE 8001, 80012Y-1-7 (2011).
4.- Complete a microtopographic non-invasive inspection to evaluate with precision the main roughness parameters of the biomaterials by means of an optical triangulation system. Complement the information about roughness with the results of specular gloss measurements.	VI	Fernández-Oliveras, A., Costa, M. F. M., Pecho, O. E., Rubiño, M. and Pérez, "Rugometric and microtopographic non-invasive inspection in dental-resin composites and zirconia ceramics". Proc. SPIE, In press (2013). Fernández-Oliveras, A., Costa, M. F. M., Yebra, A., Rubiño, M. and Pérez, M. M., "Gloss measurements and rugometric inspection in dental biomaterials". Proc. SPIE, In press (2013).

Chapter III.

SCATTERING ANISOTROPY EXPERIMENTAL ANALYSIS AND COMPARISON WITH DENTAL TISSUES

STATE OF THE ART

Knowledge of the optical properties of biological structures is useful for clinical applications, and even more so when dealing with incoming biomaterials engineered to benefit the patient.

The optical properties of turbid media are described by the absorption coefficient, the scattering coefficient (μ_s), and the phase function, which represents the scattering angular distribution. The phase function is usually characterized by the scattering anisotropy factor g, which equals the average cosine of the scattering angle. For media with anisotropic scattering, g and the scattering coefficient can be combined into a reduced scattering coefficient, $\mu'_s = (1-g)$, to effectively assume that the media exhibits isotropic scattering.

Certain methods for determining optical parameters assume that light scattered from biological media is isotropically distributed over all angles [III.1-III.3]. However, many works show that an angular dependence of light scattering may exist and affect the optical behaviour of biological media [III.4-III.11]. Therefore, the recovery of the scattering-angular distribution is important for biological media and, consequently, a better knowledge of the scattering anisotropy in biomaterials becomes of great interest.

On the other hand, computational models based on Mie theory can be used to estimate the scattering anisotropy coefficient [III.12], but they are usually applied to ideal medium where the shape of the scattering particle is perfectly spherical. Therefore, this approach is potentially hazardous when applied to real material with irregular particle shapes. Although values of specific optical properties have usually been determined employing Mie theory [III.13], the extent to which this theory can be applied to light scattering in dental-resin composites has not yet been analysed. For that reason, it is important to compare the values estimated with these methods with measured data from independent experimental techniques.

The fulfilment of optimal quality and final success in medical application of biomaterials required complete studies to assess the appropriate material properties. In this sense, comparative analysis of optical behaviour in dental tissues and their substitute material becomes necessary.

The aim of this chapter is to experimentally analyse the scattering anisotropy in human enamel and dentine and their potential substitute biomaterials (hybrid dental-resin, nano-filled composite, and zirconia ceramic) and comparatively study them.

The scattering anisotropy factor can be experimentally determined by irradiating the media with a laser beam and making angular scattering measurements in a goniometer [III.4-III.7]. Since the scattering coefficient depends on the wavelength considered, in order to compute the reduced scattering coefficient, the corresponding g value should be known. However, the spectral variation of the scattering anisotropy factor has not been fully analysed.

In the present chapter, goniometric measurements were made for four wavelengths in the visible range, allowing a spectral characterization of the material studied. Previously, for each material, measurements were made with two different sample thicknesses at the same wavelength, checking the behaviour of the angular scattering profile. The extrapolation of these scattering patterns to an incremental thickness would specify the appropriate phase function to be used in the radiative-transport equation [III.4]. With the intention of establishing comparisons between different materials, measurements were made with the most similar sample thicknesses for the rest of the wavelengths.

Moreover, at 632.8 nm, a computational model was applied to estimate the scattering anisotropy coefficient of two different dental-resin composites (nano-filled and hybrid). Some of the required input parameters for computing the theoretical model, such as mean particle size and filler-volume fraction of the dental resins, were experimentally determined elsewhere [III.14].

THEORETICAL BACKGROUND

When light travels through a biological media, it can be reflected, transmitted, or scattered due to the heterogeneity of the medium. When light finds an obstacle in the medium, a scattering event occurs, and the light-propagation direction changes; if light finds another obstacle, a new scattering event takes place and the light-propagation direction changes again. Scattering depends on the wavelength of irradiation, the refractive indexes of the medium, and the particle which causes the scattering, as well as on the particle diameter and cross section.

When light is scattered by a particle, its trajectory is deflected by an angle called scattering angle (θ). A value $\theta = 0$ means that photons continue in the same direction as before the collision. The component of the new trajectory which is aligned in the forward direction is proportional to the scattering-angle cosine. The scattering anisotropy factor g is a measure of the amount of forward direction retained after a single scattering event, and is defined by the mean value of the scattering-angle cosine:

$$g = \int_{-1}^{1} p(\cos\theta)\cos\theta d(\cos\theta) \qquad \text{(III.1)}$$

where p is the scattering-phase function that describes the fraction of light scattered from the obstacle as a function of the scattering angle. The phase function is normalized so that its integral over all directions is one:

$$\int_{-1}^{1} p(\cos\theta) d(\cos\theta) = 1 \qquad \text{(III.2)}$$

Being normalized, $p(\theta)$ represents the probability of θ being the angle between the direction of the photons before and after the scattering event . The anisotropy factor varies between complete backward scattering (g = -1) and complete forward scattering (g = 1). If g = 0, then the medium is said to be isotropic, signifying that photons have the same probability of going in any direction.

The phase function describes the fraction of light scattered from one direction into another one and depends only on the angle between the two directions (scattering angle). Theoretically the scattering profile is independent of the incoming light direction. This means that the phase function should be symmetric when considering different directions of rotation with respect to the incident direction of light. Therefore, when goniometric measurements are made in order to determine the scattering profile, the direction of rotation is usually chosen arbitrarily.

In this chapter, for goniometric measurements, we have considered both directions of rotation in the same plane and proved that experimental phase functions are not symmetric. Taking this into account, to compute the *g* factor that represents the phase function, we consider the average between the two values corresponding to both angular directions of rotation. Many works deal with scattering anisotropy in turbid media but do not in general consider the asymmetry of experimental phase functions in the recovery of the *g* factor by goniometric measurements [III.5-III.7].

On the other hand, if the particle which causes the scattering has a size close to the wavelength of incident light, Mie theory can be applied to evaluate the scattering events. This theory provides a solution to the problem of light scattered by homogeneous spherical particles.

MATERIALS AND METHODS

Sample preparation

Two different types of dental-resin composites (nano-filled and hybrid) with similar polymeric matrixes (dimethacrylates): bisphenol A diglycidylether methacrylate (Bis-GMA), bisphenol A polyethylene glycol diether dimethacrylate (Bis-EMA), urethane dimethacrylate (UDMA) and triethylene glycol dimethacrylate (TEGDMA), were studied. The characteristics of each dental-resin composite, according to the manufacturer, are shown in Table III.1.

Table III.1. Characteristics of the two different types of dental resin-composites analysed according to the manufacturer data.

Dental-Resin Composite	Organic Matrix	Inorganic Filler	Type
Filtek Supreme XT	Bis-GMA, Bis-EMA, UDMA, TEGDMA	Silica agglomerate, highly dispersed silica	Nanocomposite
Tetric EvoCeram	Bis-GMA, UDMA, TEGDMA	Ba glass, ytterbium triflouride, mixed oxides, pre-polymers	Hybrid

Specimens were made on a glass plate (Knittel GLASER, Bielefeld, Germany) with a circular hole prepared with a high-speed hand-piece and a round bur. With the use of glass plates 1 mm and 0.5 mm thick, two samples of different thickness were prepared from each dental resin. After the placement of composites, a clear plastic sheet (Acrylite Plus Clear, Tap Plastics, Dublin, CA, USA) was laid on the top and bottom of the mould and another glass plate was pressed onto the top to standardize the specimen thickness. Each sample underwent photo-polymerization for 40 seconds using a light-curing unit (Bluephase, Ivoclar Vivadent AG, Liechtenstein) with a irradiance of 1100 mW/cm^2 ± 10%. After photo-polymerization, all glass plates were removed. Specimens were handled according to manufacturer's instructions. All specimens were prepared by the same user in order to minimize variability.

For dental-tissue sample preparation, one human tooth was laterally cut into slices. All cuts were made with an automatic precision cut-off machine (Accutom-5 *Struers*, Ballerup, Denmark). The slices provided samples of enamel and dentine with different thicknesses. Specimens were polished with silicon carbide paper from 220 to 4000 grits and finally with alumina slurry of 1, 0.3 and 0.05μm. Then, they were placed in an ultrasonic cleaner (*Renfert*, CA, USA) with distilled water in 3 cycles of 10 min to eliminate polishing detritus. Finally, the samples were stored in distilled water.

Sintered LAVA™Zirconia samples provided by the manufacturer with two different thicknesses were used to study zirconia ceramic material. The framework ceramics were fabricated using computer-aided design and manufacturing (CAD/CAM) procedures from presintered zirconia blanks, the sizes of which had been increased to compensate for shrinkage during sintering in a special high-temperature furnace.

For the different material analyzed, sample thicknesses used are listed in Table III.2.

Table III.2. Thicknesses of the samples used in the measurements (values determined with 0.01 mm in sensitivity).

Material	Thicknesses (mm)	
Enamel	0.97	0.46
Dentine	0.88	0.41
Nanocomposite	1.11	0.46
Hybrid composite	1.03	0.46
Zirconia ceramic	0.30	0.50

Experimental setup

The set-ups used for scattering anisotropy measurements (Figures III.1 to III.4) schematically consisted of a randomly polarized laser source, a goniometric rotary stage of 120 mm in diameter (NT62-295, Edmund Optics, USA) and a photodiode detector connected to an amplifier-multimeter (34401A, Agilent Technologies, USA) measuring system. The photodiode was mounted at the edge of the rotary stage and had an aperture of 3 mm in diameter. The samples were placed in the centre of the rotary stage and irradiated with the laser beam. The laser light scattered off the sample was detected by the photodiode for different scattering angles. With each sample, measurements were made in both directions of rotation (between 0 and 180 degrees, and between 0 and -180 degrees).

In the case of the backward-forward scattering measurements, with the set-up configuration shown in Figures III.1 and III.2, the detector itself may prevent the laser beam from reaching the sample. To avoid this drawback, we propose another configuration where a beam splitter allows the laser beam to aim at the sample by reflection without blocking backscattered light, which reached the detector by transmission (Figures III.3 and III.4). This set-up configuration was used for the measurements at scattering angles between 160 and 180º, and between -164 and -180º.

The scattering anisotropy factor was calculated for the specimens at different wavelengths. For this, measurements were made using two laser sources: a He-Ne laser source with a power of 17.0 mW and beam diameter of 0.98 mm (LHRR-1700, Research Electro Optics, USA), which provided a wavelength of 632.8 nm; and a tunable ion-argon laser source with 1000 mW of maximum total power and beam diameter of 0.75mm (Stellar-Pro-L ML/1000, Modu-Laser, USA), which provided wavelengths of 457.9, 488.0 and 514.5 nm.

First, with the He-Ne laser, measurements were made for each material with two different sample thicknesses (shown in Table III.2) in order to check the behaviour of the angular scattering profile. Then, with the ion-argon laser, measurements were made with the most similar sample thickness (third column in Table III.2), to establish comparisons between different materials.

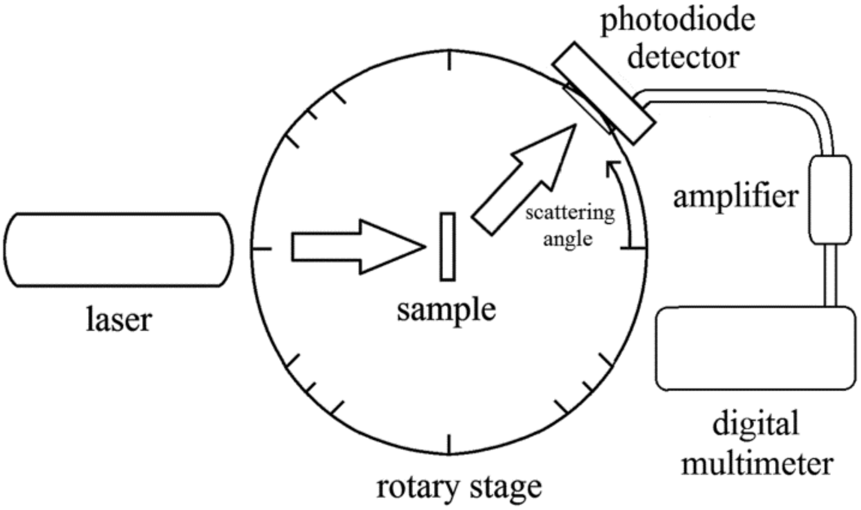

Figure III.1. Scheme of the experimental set-up used in scattering anisotropy measurements on the dental tissues and biomaterials, for scattering angles between 0 and 156º, and between 0 and -162º.

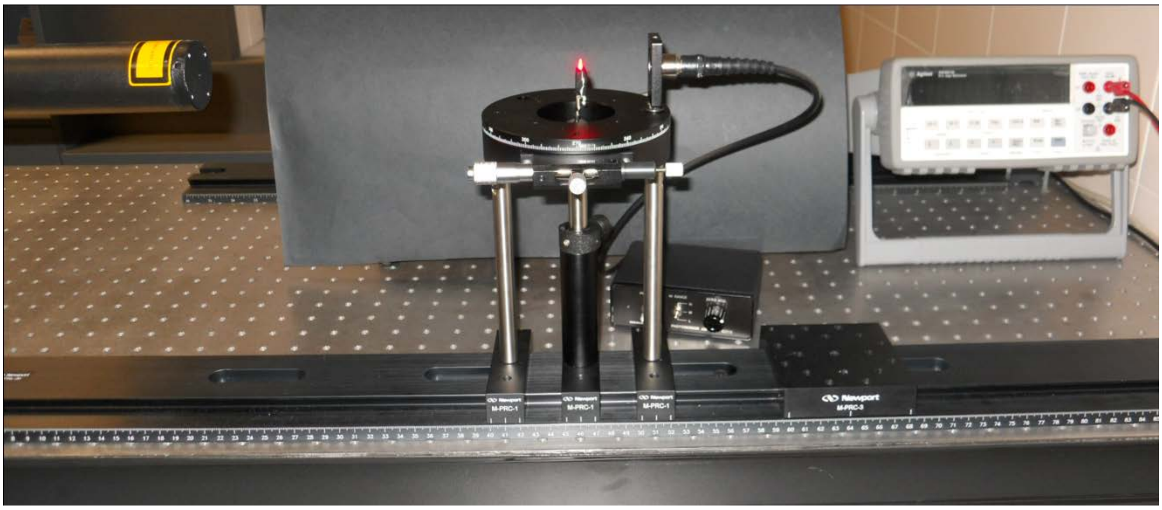

Figure III.2. Experimental set-up used in scattering anisotropy measurements on the dental tissues and biomaterials, for scattering angles between 0 and 156º, and between 0 and -162º.

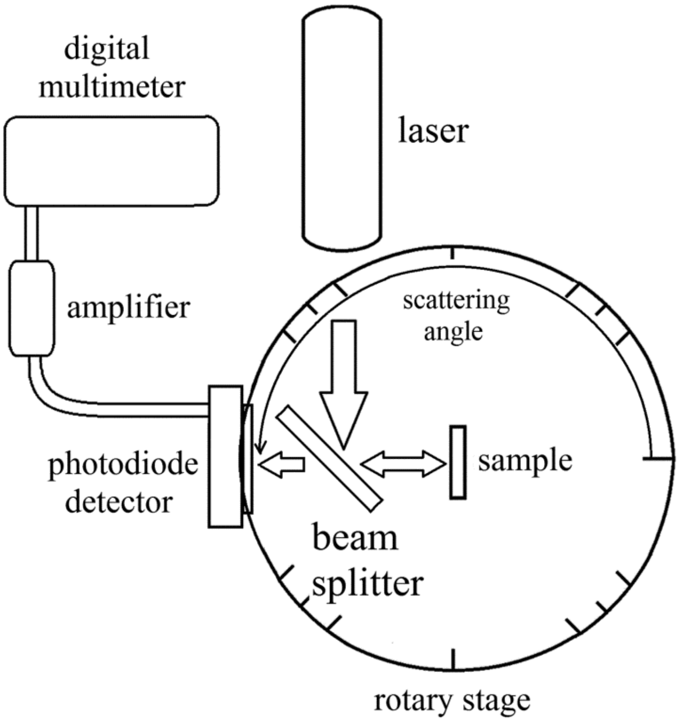

Figure III.3. Scheme of the experimental set-up used in scattering anisotropy measurements on the dental tissues and biomaterials, for scattering angles between 160 and 180º, and between -164 and -180º.

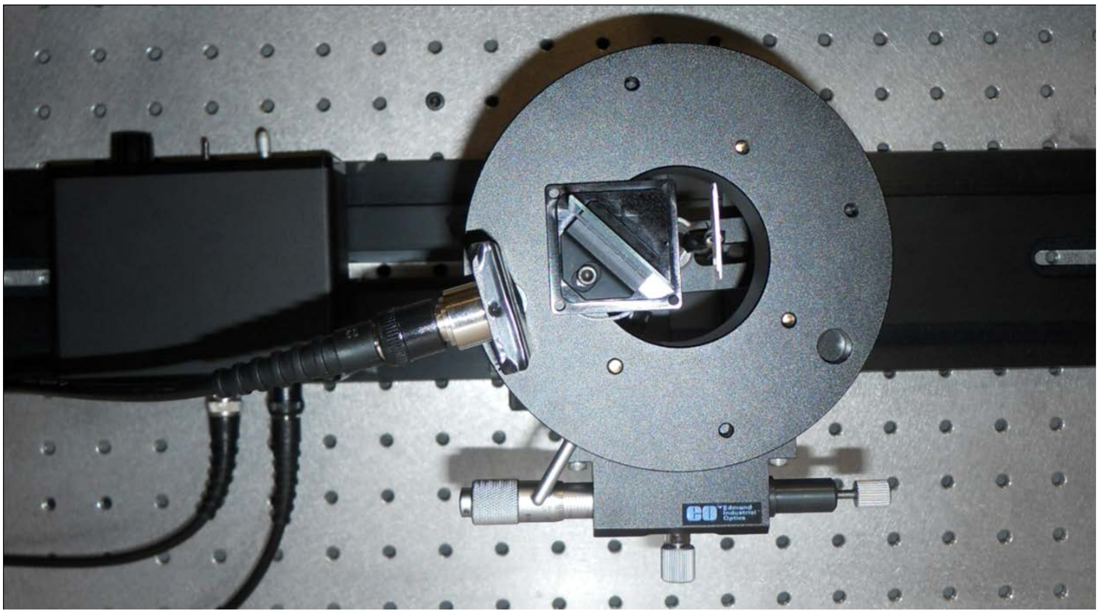

Figure III.4. Detail of the experimental set-up used in scattering anisotropy measurements on the dental tissues and biomaterials, for scattering angles between 160 and 180º, and between -164 and -180º.

Data processing

The data of detected values represented the collected power of the scattering signal. From the measurements of scattered-light signal (*V*) at various scattering angles (*θ*), the scattering anisotropy factor (*g*) was calculated according to [III.6]:

$$g = \frac{\sum_i V_i \cos\theta_i}{\sum_i V_i} \qquad \text{(III.3)}$$

where the sums were taken over the evaluated scattering angles and signal values, at an increment of 4 degrees of scattering angle.

Measurements were made in both directions of rotation (between 0 and 180 degrees, and between 0 and -180 degrees). Considering positive and negative angles, we calculated both corresponding *g* values and determined the average g. The average deflection angle in a scattering event (average scattering angle) can be calculated as the arccosine of *g*, since *g* represents the average cosine of the scattering angle. Therefore, from the average *g* value, the related average scattering angle was determined. The uncertainties associated to the anisotropy-factor values and the average scattering angles were calculated taking into account the law of propagation of uncertainties [III.15].

For the scattering angles between 160 and 180°, and between -164 and -180°, measurements were made under different experimental conditions since we used another set-up (shown in Figures III.3 and III.4). The scattered light signals were normalized in order to add the measurements to the rest of the data (collected with the set-up in Figures III.1 and III.2). The normalizing factor was estimated in this way: for three different scattering angles, measurements of the scattering signal were made with both experimental set-ups. For each pair of measurements, a value of the normalizing factor was calculated and the average was finally considered. Each normalizing factor value was determined by dividing the scattering signal measured with the set-up schematized in Figure III.1 by the scattering signal measured with the set-up schematized in Figure III.3. The uncertainty in the normalizing factor was also calculated according to the law of propagation of uncertainties and considered in the computation of the uncertainties associated with the normalized scattering signal values (those corresponding to scattering angles between 160 and 180º, and between -164 and -180º).

As a test of reproducibility, for the zirconia ceramic sample at 488.0 nm, measurements with the set-up proposed (Figures III.3 and III.4) were repeated, demonstrating that the difference between the corresponding *g* values was less than the associated uncertainty.

To investigate the significance of the signal values measured with the set-up proposed for angles between 160 and 180º, and between -164 and -180º, we also computed the g values while omitting these measurements. The difference between the *g* values determined (with and without these measurements) was found to be significant, for each material studied.

Before processing, the data were corrected to reduce effects from the background noise, due to laboratory ambient lighting and photodiode dark current (response produced in the absence of input light-signal, i.e. with the detector in the dark). The background noise was corrected by subtracting from the measured signal values the background signal detected when obscuring the laser source.

RESULTS AND DISCUSSION

To make comparisons between the scattering-signal profiles found at different wavelengths and with different sample thicknesses, we normalized the scattering-signal profiles. For positive scattering angles, the profile was normalized by dividing the each signal value by the sum of all the signal values from 0 to 180. For negative scattering angles, the profile was normalized by dividing each signal value by the sum of all the signal values from 0 to -180. In this way, we determined the normalized phase function from the angular scattering profile. Each value of the normalized phase function represents the probability associated to the corresponding scattering angle as the deflection angle in a scattering event.

Influence of sample thickness

As pointed out above, to check the influence of the sample thickness in the angular scattering profile, with the He-Ne laser, we made measurements for each material with two different sample thicknesses (shown in Table III.2).

The scattering phase functions found with the different sample thicknesses of each material are shown in Figures III.5 to III.9. The corresponding average *g* values and the related average scattering angles are listed in Table III.3, with their associated uncertainties. It is noteworthy that by virtue of the low uncertainties found, differences between the *g* values are significant.

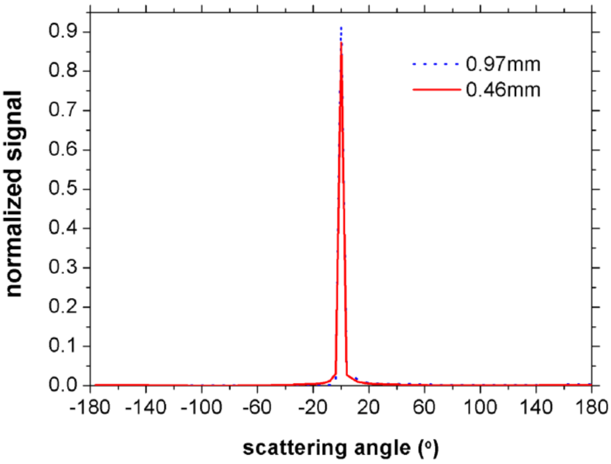

Figure III.5. Normalized scattering signal for the human enamel samples of different thicknesses.

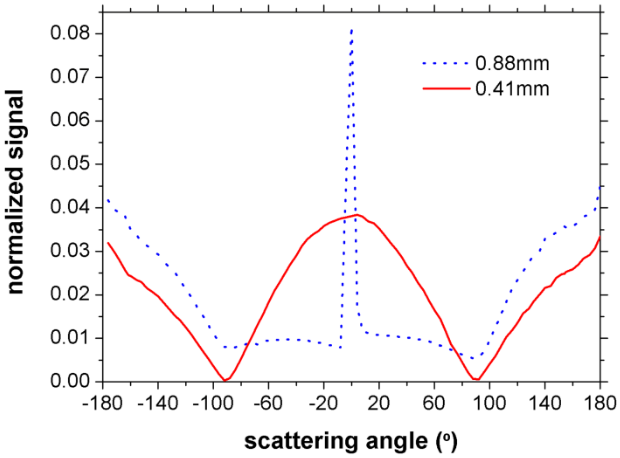

Figure III.6. Normalized scattering signal for the human dentine samples of different thicknesses.

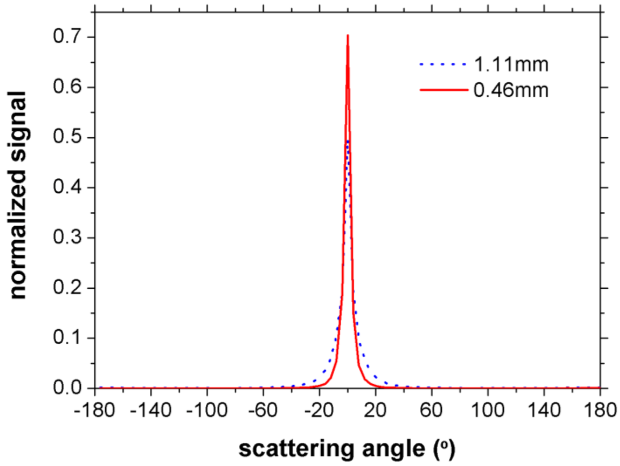

Figure III.7. Normalized scattering signal for the dental nanocomposite samples of different thicknesses.

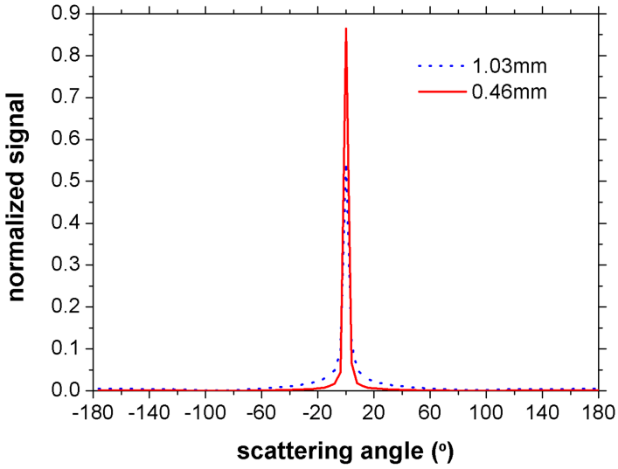

Figure III.8. Normalized scattering signal for the hybrid composite samples of different thicknesses.

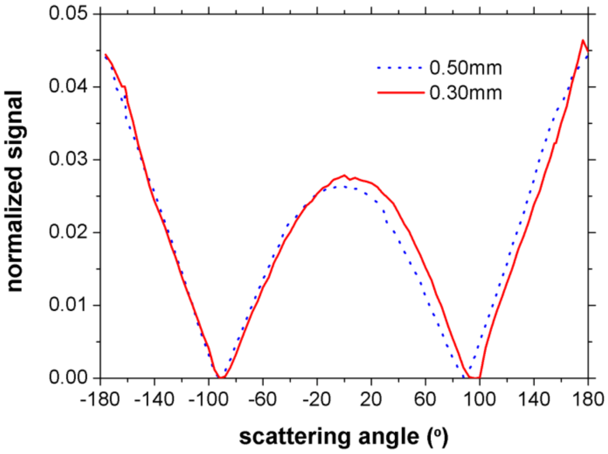

Figure III.9. Normalized scattering signal for the zirconia ceramic samples of different thicknesses.

Table III.3. Average *g* values and scattering angles with their associated uncertainties for the different sample thicknesses (λ = 632.8 nm).

Material	**Thickness (mm)**	**Average *g***	**Average θ (º)**
Enamel	0.97	0.8870 ± 0.0003	27.51 ± 0.04
Dentine	0.88	-0.3021 ± 0.0020	107.59 ± 0.12
Nano-composite	1.11	0.9283 ± 0.0004	21.83 ± 0.06
Hybrid composite	1.03	0.7813 ± 0.0004	38.62 ± 0.04
Zirconia ceramic	0.30	-0.1763 ± 0.0014	100.15 ± 0.08
Material	**Thickness (mm)**	**Average *g***	**Average θ (º)**
Enamel	0.46	0.91867 ± 0.00011	23.268 ± 0.016
Dentine	0.41	0.0620 ± 0.0010	86.45 ± 0.06
Nano-composite	0.46	0.98297 ± 0.00021	10.59 ± 0.07
Hybrid composite	0.46	0.95429 ± 0.00014	17.39 ± 0.03
Zirconia ceramic	0.50	-0.2074 ± 0.0024	101.97 ± 0.14

The results show that, for all specimens studied, the thicker the sample the lower the *g* value obtained from goniometric measurements, in accordance with conclusions of other works [III.4]. As established, the thicker sample attenuates the on-axis intensity signal, yielding a less forward-directed scattering profile than the thinner sample. The extrapolation of these scattering profiles to an incremental thickness would specify the appropriate phase function to be used in the radiative-transport equation.

Therefore, in the subsequent measurements, we used the thinner sample of each material, except in the case of the zirconia ceramic; for zirconia ceramic, since differences between the two sample thicknesses were lower, we chose the thicker one because its thickness was more similar to those of the thinner samples of the other materials.

Spectral variation

In Figures III.10 to III.14, for each material, the scattering phase functions at the evaluated wavelength are shown. The average *g* values calculated from the measurements and the related average scattering angles with their uncertainties associated are listed in Tables III.4 and III.5. It is worth noting the low uncertainty found, which allowed the *g* values calculated to be distinguished and compared.

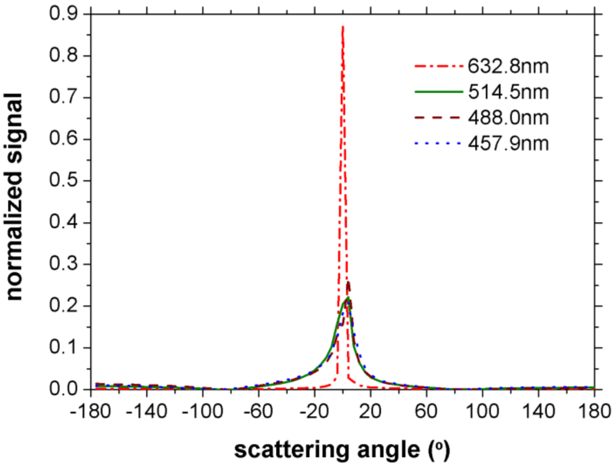

Figure III.10. Normalized scattering signal of the human enamel at different wavelengths of the visible spectrum.

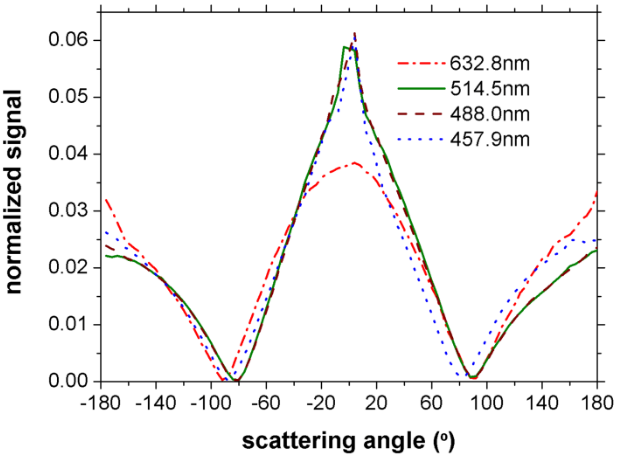

Figure III.11. Normalized scattering signal of the human dentine at different wavelengths of the visible spectrum.

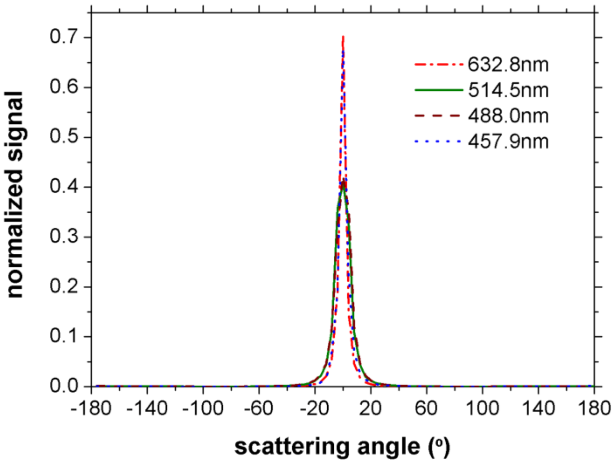

Figure III.12. Normalized scattering signal of the dental nanocomposite at different wavelengths of the visible spectrum.

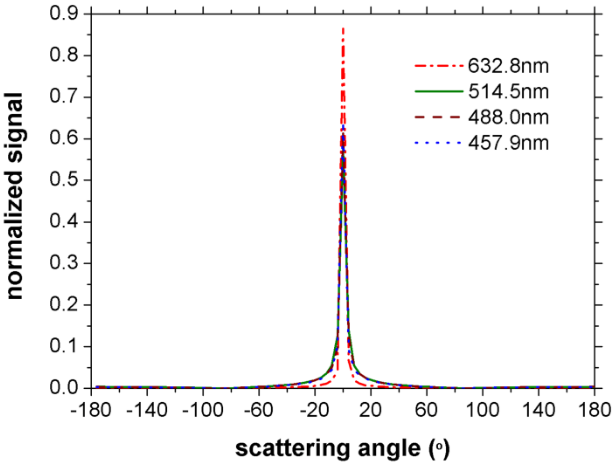

Figure III.13. Normalized scattering signal of the hybrid composite at different wavelengths of the visible spectrum.

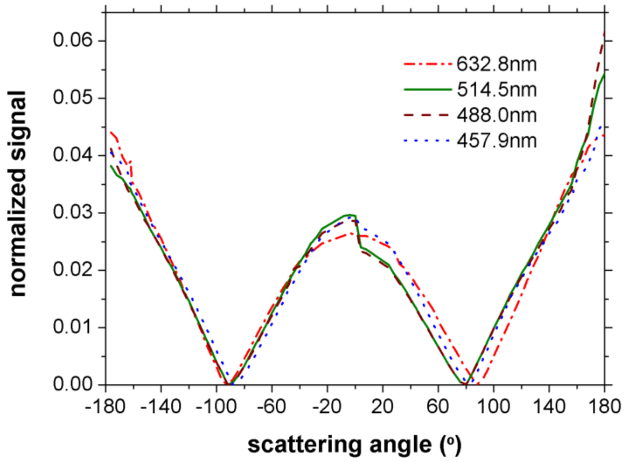

Figure III.14. Normalized scattering signal of the zirconia ceramic at different wavelengths of the visible spectrum.

Table III.4. Average *g* values with their associated uncertainties for the different wavelengths analysed.

λ (nm)	**Average *g***		
	Enamel	**Nanocomposite**	**Hybrid composite**
457.9	0.6812 ± 0.0008	0.9617 ± 0.0003	0.8710 ± 0.0003
488.0	0.6666 ± 0.0006	0.9487 ± 0.0004	0.8555 ± 0.0003
514.5	0.7418 ± 0.0006	0.9570 ± 0.0004	0.8558 ± 0.0003
632.8	0.91867 ± 0.00011	0.98297 ± 0.00021	0.95429 ± 0.00014

λ (nm)	**Average *g***	
	Dentine	**Zirconia ceramic**
457.9	0.1291 ± 0.0010	-0.192± 0.003
488.0	0.2104 ± 0.0009	-0.247± 0.005
514.5	0.2122 ± 0.0010	-0.233± 0.003
632.8	0.0620 ± 0.0010	-0.2074± 0.0024

Table III.5. Average scattering angles with their associated uncertainties for the different wavelengths analysed.

λ (nm)	**Average θ (º)**		
	Enamel	**Nanocomposite**	**Hybrid composite**
457.9	47.06 ± 0.06	15.91 ± 0.06	29.42 ± 0.03
488.0	48.19 ± 0.05	18.44 ± 0.07	31.19 ± 0.03
514.5	42.11 ± 0.05	16.87 ± 0.08	31.16 ± 0.04
632.8	23.268 ± 0.016	10.59 ± 0.07	17.39 ± 0.03

λ (nm)	**Average θ (º)**	
	Dentine	**Zirconia ceramic**
457.9	82.58 ± 0.06	101.08 ± 0.17
488.0	77.86 ± 0.05	104.3 ± 0.3
514.5	77.75 ± 0.06	103.48 ± 0.20
632.8	86.45 ± 0.06	101.97 ± 0.14

The results reveal that g values have similar spectral variation for all the material, except for the human dentine. For the dental-resin composites, human enamel, and zirconia ceramic, the g values diminish at 488.0 nm and augment from 514.5 nm. For the human dentine, the g value increase at 488.0 nm and decrease from 514.5 nm. This may be due to the different internal structure of dentine, which is composed of the so-called tubules, which are oriented from the pulp to the dentin-enamel junction [III.16].

Instead, dental enamel is internally composed of inorganic apatite-like crystals surrounded by a protein-lipid-water matrix, with the crystals clustered together in rods approximately perpendicular to the tooth surface [III.17]. Compared with the dentine structure, the enamel structure is more similar to the dental-resin composite structure (since dental-resins are composed by inorganic filler particles immersed in an organic matrix), and also to the microstructure of 3Y-TZP ceramics for dental applications, which consists of small equiaxed grains with diameter sizes depending on the sintering temperature [III.18].

For the dental composites, the angular scattering profiles indicate the presence of a more pronounced forward-directed scattering in the nano-filled dental resin than in the hybrid dental-resin composite. The results show that *g* values are higher for the nanocomposite than for the hybrid composite, at every wavelength studied. The higher *g* values for the nanocomposite reveal that the scattering particle is more similar to a perfect sphere, since it is established that for more spherical scattering particles the scattering anisotropy factor increases [III.5]. On the other hand, for spherical nanoparticles (diameters from 0.05 to 2.5 µm) in aqueous suspensions, it is established that the g value increases with the scatterer diameter [III.19]. Therefore, lower *g* values for the hybrid composite may be related to a lower concentration of scattering centers, resulting in a smaller scatterer diameter. This agrees with observations made elsewhere, when filler particle size and particle-size distribution of dental-resin composites was determined employing a digital-image analysis [III.14].

From the scattering profiles of Figures III.10 to III.14 and the *g* values of Table III.4, we can conclude that, in general terms, the dental-resin composites and human enamel show a similar angular scattering behaviour; moreover, on the other hand, the zirconia ceramic present a scattering angular behaviour more similar to that of human dentine. This is valuable for biomedical applications, since it means that the biomaterials analysed show angular-scattering behaviour comparable to that of the tissues that they are meant to replace.

Comparison between experimental and computational methods for the dental-resin composites

To determine the scattering anisotropy coefficient by means of Mie theory, a MATLAB code previously described by Matzler [III.12] was used. This code is limited to homogeneous dielectric spheres and its key parameters for calculations are the Mie coefficients to compute the amplitudes of the scattered field. The computation of these parameters has been the most challenging part in Mie computations due to the involvement of spherical Bessel functions up to high order. MATLAB's built-in double-precision Bessel functions were used for the computation of the Mie coefficients with this code.

From Mie coefficients, the scattering efficiency and also the scattering functions were determined. These functions describe the scattered field and are required if the detailed shape of the angular scattering pattern is needed, as in the case of scattering anisotropy calculations. To describe the scattering functions, angular scattering patterns of the spherical harmonics, followed from recurrence relations of the scattering angle cosine, were used. These data allowed the computation of the scattering anisotropy coefficient values.

The input parameters required for computation with the MATLAB code are the refractive indexes (*n*) of the organic matrix and filler particles, the particle size, and the filler volume fraction. For the refractive indexes, data provided by the manufacturers was used. The filler fraction and the mean particle size were calculated from independent morphological measurements [III.14] employing high-zoom Field Emission Scanning Electron Microscope (Fe-SEM) digital images.

The values of the parameters used as input in the computational model, for both dental-resin composites involved in this study are shown in Table III.6.

Table III.6. Input parameters for the computational estimation of the scattering anisotropy factor in the dental-resin composites.

Dental-resin composite	**Filler fraction (%)**	**Average particle size (μm)**	**Filler refractive index**	**Matrix refractive index**
Nanocomposite	75.8	0.827	1.56	1.546
Hybrid composite	66.8	0.613	1.52	1.546

Table III.7 presents the values of the scattering-anisotropy factor (*g*) for both dental-resin composites, as determined from the gonometric measurements and as estimated with the computational method, for a wavelength of 632.8 nm.

Table III.7. Experimental and estimated values of the scattering anisotropy factor for the dental resin-composites analysed (λ = 632.8 nm).

Dental-resin composite	**Experimental method**	**Computational method**
Nanocomposite	0.98297 ± 0.00021	0.9399
Hybrid composite	0.95429 ± 0.00014	0.8975

As can be seen, computational predictions of *g* are lower than reflected by the experimental data, but the agreement is good for both materials. In the case of the nano-filled composite, values of *g* found with both methods are closer to each other than in the case of the hybrid composite. This result may be related to irregular filler-particle shape of the hybrid dental-resin composite. The higher experimental values (compared with Mie theory computations) may indicate that the scattering particle causes more narrow-angle scattering than does a perfect sphere of equal volume.

Comparative analysis of pre-sintered and sintered zirconia ceramics

To study zirconia ceramic dental material, pre-sintered and sintered LAVA™Zirconia samples with similar thicknesses provided by the manufacturer were used. For the samples analysed, thicknesses used are listed in Table III.8.

The samples were irradiated with the He-Ne laser beam (λ = 632.8 nm) and the angular-scattering distributions were measured using the rotating goniometer, as described previously. Figure III.15 shows the scattering phase functions obtained for the human dentine and the zirconia samples analysed.

Table III.8. Sample thicknesses used in the measurements for the comparative analysis of the zirconia ceramics (values determined with 0.01 mm in sensitivity).

Material	Thickness (mm)
Pre-sintered zirconia ceramic	0.48
Sintered zirconia ceramic	0.50
Human dentine	0.41

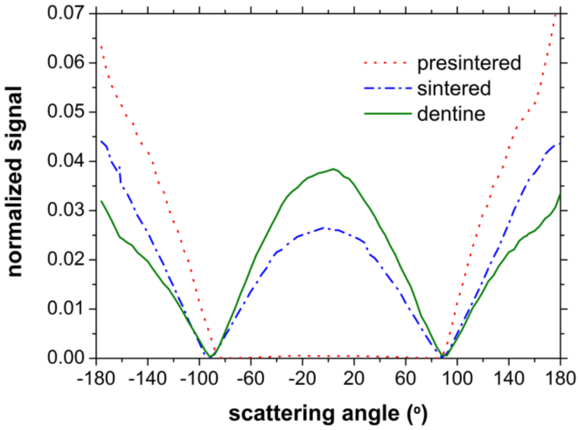

Figure III.15. Normalized scattering signal for the zirconia ceramics (pre-sintered and sintered) and human dentine.

The average *g* values calculated from the measurements and the related average scattering angles with their uncertainties associated are listed in Table III.9. It bears noting the low uncertainties found, which allowed the g values calculated to be distinguished and compared.

Table III.9. Average *g* values and average scattering angles with their associated uncertainties for the human dentine and the zirconia samples analysed.

Sample	Average *g*	Average *θ* (º)
Pre-sintered zirconia ceramic	-0.7970 ± 0.0016	142.84º ± 0.15º
Sintered zirconia ceramic	-0.2074 ± 0.0024	101.97º ± 0.14º
Human dentine	0.0620 ± 0.0010	86.45º ± 0.06º

The scattering profiles of Figure III.15 and the *g* values of Table III.8 indicate the presence of a more pronounced forward-directed scattering in the human dentine than in the zirconia ceramic samples. However, this difference is considerably lower in the case of the sintered zirconia sample. In the case of the pre-sintered sample, only the backward lobe of the scattering profile is comparable to that of human dentine. By contrast, for the sintered zirconia and the dentine samples, both the backward and the forward lobes of the scattering profiles show similar behaviour. For the pre-sintered zirconia ceramic, the far lower values of the forward scattering lobe lead to a higher opacity compared with the dentine tissue and the sintered zirconia ceramic.

In general terms, the scattering angular behaviour of zirconia ceramic is more similar to that of human dentine after the sintering process. This finding is valuable for clinical applications, since it means that the ceramic material analysed shows more appropriate and advantageous optical properties when it has been sintered, as its angular-scattering behaviour becomes comparable to that of the tissue that it is meant to replace.

REFERENCES

[III.1] Anderson, R. R. and Parish, J. J., "The optics of human skin," J. Invest. Dermatol. 77, 13-19 (1981).

[III.2] van Gemert, M. J. C., Verdaasdonk, R., Stassen, E. G., Schets, G. A. C. M., Gijsbers, G. H. M. and Bonnier, J. J., "Optical properties of human blood vessel wall and plaque" Lasers Surg. Med. 5, 235–237(1985)..

[III.3] Ertefai, S. and Profio, A. E., "Spectral transmittance and contrast in breast diaphanography," Med. Phys. 12, 393–400 (1985).

[III.4] Jacques, S. L., Alter, C. A. and Prahl, S. A., "Angular Dependence of HeNe Laser Light Scattering by Human Dermis," Lasers Life Sci. **1**, 309-334 (1987).

[III.5] Steinke J. M. and Shepherd, A. P. "Comparison of Mie theory and the light scattering of red blood cells" Appl. Opt. 27, 4027-4033 (1988).

[III.6] Sardar, D. K., Salinas, F. S., Perez, J. J. and Tsin, A. T. C., "Optical characterization of melanin," J. Biomed. Opt. 6, 404-411 (2001).

[III.7] Sardar, D. K., Yow, R. M., Tsin, A. T. C. and Sardar, R., "Optical scattering, absorption and polarization of healthy and neovascularized human retinal tissues," J. Biomed. Opt. 10, 0515011-1-8 (2005).

[III.8] Joshi, N. Donner C. and Jensen, H. W., "Noninvasive measurement of scattering anisotropyin turbid materials by nonnormal incident illumination," Opt. Lett. 31, 936-938 (2006).

[III.9] Hammer, M., Schweitzer, D., Thamm, E. and Kolb, A., "Optical properties of ocular fundus tissues determined by optical coherence tomography," Opt. Commun. 186 149-153 (2000).

[III.10]Kienle, A., Patterson, M. S., Ott, L. and Steiner, R., "Determination of the scattering coefficient and the anisotropy factor from laser Doppler spectra of liquids including blood" Appl. Opt. 35, 3404-3412 (1996).

[III.11]Liu, Q. and Ruprecht, E. "Radiative transfer model: matrix operator method," Appl. Opt. 35(21), 4229-4237, (1996).

[III.12]Matzler, C., MATLAB functions for Mie scattering and absorption, Research Report No. 2002-08, Institute of Applied Physics, University of Bern (2002).

[III.13]Bohren, C. F. and Huffman, D. R., [Absorption and scattering of light by small particles], John Wiley and Sons Press, New York (1983).

[III.14]Ghinea, R., Ugarte-Alvan, L., Ionescu, A. M., Cardona, J. C., Pérez, M. M. and Yebra, A., "Influence of the size and distribution of filler particles on the colour of resin composites," Proceedings of the IS&T's Fourth European Conference on Color in Graphics, Imaging and Vision (2008).

[III.15]International Organization for Standardization, Guide to the Expression of Uncertainty in Measurement. Corrected and reprinted, Geneva, 1995.

[III.16]Major, I. A., *The morphology of dentin and dentinogenensis* in [Dentin and Dentino Genesis], Linde, A. Ed., CRC Press, Boca Raton, Vol. 1, 2-18 (1984).

[III.17]Curzon, M. E. J. and Featherstone, J. D. B., *Chemical composition of enamel* in [Handbook of Experimental Aspects of Oral Biochemistry], Lazzan, E. P. Ed., CRC Press, Boca Raton, 123–135 (1983).

[III.18]Chicea, J. D., "Probing particle aggregation in aqueous suspensions by light scattering anisotropy measurements," Optoelectron. Adv. Mater. 12, 152 (2010).

Chapter IV.

DETERMINATION OF SCATTERING AND ABSORPTION PROPERTIES USING THE INVERSE-ADDING-DOUBLING METHOD

STATE OF THE ART

Optical properties of biological media are key parameters in such contrasting fields as the food industry [IV.1] and legal or forensic medicine [IV.2]. In particular, research concerning the interaction of laser light with new biomaterials is of great interest for clinical applications. The development of laser-based techniques for treatments and diagnostics depends on the knowledge of light distribution in the biological media. In restorative dentistry this is especially important, since novel mechanisms for improving patients' comfort and satisfaction are permanently sought.

The most disturbing aspects for dentistry patients are related to the use of mechanical instruments. Therefore, the development of light tools is an appealing alternative [IV.3]. Low-power lasers are used mainly because of their biostimulatory, analgesic, and anti-inflammatory action. High-power lasers which produce visible physical effects are used as substitutes for scalpel or conventional rotary devices (e.g. laser-ablation equipment instead of a bur or turbine handpiece) [IV.4]. There are also some laser varieties that are replacing halogen lamps, for the same purposes: curing and whitening [IV.5]. The use of other laser types has been proposed as a method of decontaminating treated areas in order to prevent caries and plaque as well as to detain bacterial spread [IV.6, IV.7]. The improvement in the adhesion of restorative material is also an advantage of laser treatment cited by clinicians [IV.8].

On the other hand, aesthetic failure is one of the most widespread reasons for restoration replacement. Aesthetic restoration involves a visible match of the optical properties of restorative material and natural teeth. These optical properties are determined by absorption and scattering of light emerging on the surface and inside the medium. Among the main appearance properties of restorative materials, the perceived color and translucency are intimately related with light-scattering properties [IV.9, IV.10]. Thus, the final success and quality of the restoration imply a thorough physical understanding of light interaction in dental biomaterials.

The interaction of light in an absorbing and scattering medium can be estimated using the radiative transport equation which may be solved using the adding-doubling method [IV.11-IV.13]. Based on the latest one, the inverse adding-doubling (IAD) method was proposed [IV.14] and implemented in the *iad* program [IV.15]. With this technique, reflection and transmission measurements performed with an integrating sphere are converted to the optical properties of the media (scattering and absorption coefficients). This program has been broadly used to determine the absorption and scattering properties of diverse biological media [IV.16-IV.21]. The general idea is that measurements of reflection and transmission are provided to the program in order to extract the optical properties of the sample. Measuring the diffuse reflection, collimated transmission (T_c) and total transmission ($T_t = T + T_c$) allows the program to determine the three key optical properties: absorption coefficient (μ_a), scattering coefficient (μ_s), and anisotropy coefficient (g). However, if only the diffuse reflection and total transmission measurements are available, then only the absorption and the reduced scattering ($\mu'_s = \mu_s(1-g)$) coefficients can be calculated. Thus, in these cases, additional measurements are required in order to determine the scattering anisotropy factor. This is an important point, since materials with the same reduced scattering coefficient but different g values can show different angular scattered intensities, both in form and magnitude. Therefore, using the absorption and the reduced scattering coefficients alone for comparing materials or for reconstruction using inverse methods based, for example, on diffusion theory would lead to incorrect interpretations [IV.22].

The objective of this chapter is to experimentally analyze the scattering and absorption properties of two different types of dental-resin composites and one type of zirconia ceramic and comparatively study them. With this aim, the IAD method was applied for these biomaterials, combining previous results of goniometric measurements with transmission and reflection measurements performed using a laser-integrating-sphere-based setup. For comparisons between the different types of materials, the uncertainties associated to the optical properties were also determined.

THEORETICAL BACKGROUND

In this chapter, dental biomaterials were considered to have homogeneous optical properties and a uniform refraction index. This ensured that light will travel in a straight line until scattered or absorbed. The geometry of the samples was approximated by a plane-parallel slab of finite thickness. Such a shape allows generalization to layered samples or extension to an infinitely thick sample. The boundaries were assumed to be smooth and to reflect specularly according to Fresnel's law. The distribution of light was assumed to be static with time (both optical properties which change and irradiance times shorter than about one nanosecond were excluded) and it was assumed that there were no light sources in the material. The last assumption was that the polarization of light may be ignored.

In addition to the thickness, light propagation through a slab is determined by three parameters: the absorption coefficient, the scattering coefficient, and the phase function. The phase function indicates the fraction of light scattered from an obstacle as a function of the scattering angle. If normalized, the phase function represents the angle’s probability of being the angle between the direction of the photons before and after the scattering event. The phase function of several dental biomaterials was experimentally analyzed and discussed in detail in the previous chapter [IV.23- IV.25].

Like biological tissues, biomaterials are assumed to be random turbid media, with variations in the optical properties small enough to prevent localized absorption. In other words, they are considered to have volumetric scattering and absorption properties rather than being composed of discrete scattering and absorption centers distributed in a non-scattering, non-absorbing medium. Volumetric absorption (or scattering) is determined by multiplying an absorption (or scattering) cross section with the density of absorbers (or scatterers) [IV.26].This is how the absorption coefficient, μ_a, and scattering coefficient, μ_s, are defined. These coefficients represent the probability per infinitesimal path length that a photon will be absorbed or scattered by the material, correspondingly. The scattering and absorption coefficients are typically measured in inverse millimeters, and the reciprocal of these coefficients is the average distance that light will travel before being scattered or absorbed, respectively.

The behavior of light in a biomaterial sample for which the geometry can be approximated by a plane-parallel slab can be described by the radiative transport equation [IV.27]

$$(\hat{s}\cdot\bar{\nabla})L(\bar{r},\hat{s}) = -\mu_t L(\bar{r},\hat{s}) + \mu_s \int_{4\pi} p(\hat{s},\hat{s}')L(\bar{r},\hat{s}')d\omega' \qquad \text{(IV.1)}$$

where L is the radiance (W cm^{-2}sr^{-1}) at position r in the direction of the unit vector s. The differential solid angle $d\omega'$ has the unit vector s as an outward normal. The phase function p represents the fraction of light scattered from the direction s' in the direction s and is normalized such that it is unity when integrated over all directions. The attenuation or transport coefficient, μ_t is defined by the sum of scattering and absorption coefficients

$$\mu_t = \mu_a + \mu_s \qquad \text{(IV.2)}$$

which express the exponential attenuation of light with depth in the material (the probability that light will travel in the material to a depth z without scattering or absorbing is $e^{-\mu_t z}$). The reciprocal of the transport coefficient is the average distance that light will travel before being scattered or absorbed, usually called the mean free path or penetration depth (since it is a measure of how deep light can penetrate the material), l_t:

$$l_t = \frac{1}{\mu_t} \qquad \text{(IV.3)}$$

The left-hand side of the radiative transport equation, Eq. (IV.1), describes the rate of change of the intensity at the point indicated by r in the direction of the unit vector s. This rate of change is equal to the intensity lost due to absorption and scattering (the first term on the right-hand side) plus the intensity gained through light scattering from all other directions into the direction s (the last term on the right-hand side).

Calculations of light distribution based on the radiative transport equation require the knowledge of the absorption coefficient, the scattering coefficient, and the phase function. For these parameters to be determined, a solution of the transport equation is needed first. Due to its difficulty, diverse approximations are made to solve the radiative transport equation.

The diffusion approximation is based on the observation that the light distribution in highly scattering media tends to become isotropic. This is true even if the initial light-source distribution and the phase function are highly anisotropic. Each scattering event blurs the light distribution and, as a result, the light distribution tends towards uniformity as the number of scattering events increases.

In the diffusion theory, the radiance in Eq. (IV.1) can be divided into collimated and diffuse components:

$$L(\bar{r},\hat{s}) = L_{coll}(\bar{r},\hat{s}) + L_d(\bar{r},\hat{s}) \quad \text{(IV.4)}$$

Intuitively, once light becomes isotropic, only backward scattering terms change the net flux, forward scattering is indistinguishable from no scattering. The collimated radiance, L_{coll}, includes both the light scattered into a direction parallel to the incident beam and any unscattered light. The unscattered light does not interact with the material and satisfies the Beer's law, with transmission equation

$$T_c = e^{-\mu_t z} \quad \text{(IV.5)}$$

with z being the material thickness.

Because the collimated radiance includes light scattered forwards, the beam is attenuated not by the usual total extinction or transport coefficient, μ_t, but by the reduced transport coefficient μ_t'

$$\mu_t' = \mu_a + \mu_s' \qquad \text{(IV.6)}$$

where μ_s' is the reduced scattering coefficient

$$\mu_s' = (1-g)\mu_s \qquad \text{(IV.7)}$$

and g is the scattering anisotropy factor.

The scattering coefficient is reduced because light scattered in the forward direction is indistinguishable from unscattered light. The fraction of light *not* scattered within the forward peak is (1-g), and consequently, the scattering coefficient is reduced by a factor of (1-g).

Thus the reduced scattering coefficient, μ_s', represents the amount of light scattered outside of the collimated portion of the radiance and within the diffuse portion of the radiance. The reduced transport coefficient, μ_t', incorporates forward-scattered light into the collimated beam in the same way, such that light was incorporated into expressions for the reduced scattering coefficient.

The collimated light is attenuated at a rate proportional to the reduced transport coefficient

$$\left(\hat{s}_0 \cdot \overline{\nabla}\right) L_{coll}\left(\bar{r}, \hat{s}\right) = -\mu_t' L_{coll}\left(\bar{r}, \hat{s}\right) \qquad \text{(IV.8)}$$

where s_0 is a unit vector in the direction of the incident flux.

The amount of collimated light entering the slab is given by

$$L_{coll}\left(\bar{r}, \hat{s}\right) = \left(1 - r_s\right) L_{inc}\left(\bar{r}, \hat{s}\right) \qquad \text{(IV.9)}$$

where L_{inc} is the illuminating flux and r_s is the specular reflection coefficient given by the usual Fresnel reflection formula.

The solution of (IV.8), subject to the initial condition of Eq. (IV.9), is

$$L_{coll}(\bar{r},\hat{s}) = (1-r_s)L_{inc}(\bar{r},\hat{s})e^{-\mu'_t z/\mu_0} \quad \text{(IV.10)}$$

where μ_0 is the cosine of the angle that s_0 forms with the *z*-axis (z/μ_0 is the distance incident light travels in the material to reach a depth z in the slab) and L_{inc} may be defined from a monodirectional flux $\pi F_0(r)$ which illuminated the top surface of the sample [IV.28]

$$L_{inc}(\bar{r},\hat{s}) = \pi F_0 \delta(\mu-\mu_0) \quad \text{(IV.11)}$$

with δ being the delta function.

The diffuse radiance L_d includes the light scattered in all the directions except the one parallel to the incident beam and is characterized by the diffusion approximation as a sum of a diffuse radiant fluence ϕ_d and a diffuse irradiance (radiant flux per unit area) E_d. These are defined as the first two moments of the radiance L_d:

$$\phi_d(\bar{r}) = \int_{4\pi} L_d(\bar{r},\hat{s}')d\omega' \quad \text{(IV.12)}$$

$$\bar{E}_d(\bar{r}) = \int_{4\pi} L_d(\bar{r},\hat{s}')\hat{s}'d\omega' \quad \text{(IV.13)}$$

The diffuse radiance can then be expressed as

$$L_d(\bar{r},\hat{s}) = \frac{1}{4\pi}\phi_d(\bar{r}) + \frac{3}{4\pi}\bar{E}_d(\bar{r})\cdot\hat{s} \quad \text{(IV.14)}$$

where the factors of $1/4\pi$ and $3/4\pi$ result from normalization. Eq. (IV.14) represents the first two terms of the Taylor expansion for the diffuse radiance L_d, where ϕ_d represents the isotropic and E_d the anisotropic (slightly forward directed) contribution to the diffuse radiance. The diffusion approximation simplifies the sum to the first two terms in order to have a more tractable transport equation [IV.29]. Specifically, if we substitute this two-term expansion of the radiance into the radiative transport equation and then integrate over ω, the result is [IV.26]

$$\bar{\nabla}\phi_d(\bar{r}) = -3\mu_t'\bar{E}(\bar{r}) + \bar{Q}_1(\bar{r}) \qquad \text{(IV.15)}$$

where ***Q₁*** is the first-order source term of the volumetric source ***Q***:

$$\bar{Q}_1(\bar{r}) = \int_{4\pi} Q(\bar{r},\hat{s})\hat{s}\,d\omega \qquad \text{(IV.16)}$$

Where there are no sources, or where the sources are isotropic, Q_1 vanishes from Eq. (IV.15). Then the vector irradiance is the gradient of the scalar fluence. This equation gives precision to the intuitive notion that there is net energy flow (i.e. non-zero vector irradiance) from regions of high energy density (high fluence) to regions of low energy density.

By integrating the radiative transport equation over all directions ω at a point *r*, it yields

$$\bar{\nabla}\cdot\bar{E}_d(\bar{r}) = -\mu_a\phi_d(\bar{r}) + Q_0(\bar{r}) \qquad \text{(IV.17)}$$

where ***Q₀*** is the zero-order source term of the volumetric source ***Q*** which may be equated to [28]:

$$Q_0(\bar{r}) = \int_{4\pi} Q(\bar{r},\hat{s})d\omega = \mu_s'(1-r_s)\pi F_0(\bar{r})e^{-\mu_t' z/\mu_0} \qquad \text{(IV.18)}$$

Thus, regarding Eqs. (IV.10), (IV.11) and (IV.12), we see that Eq. (IV.17) states the net change in the diffuse radiant flux equals the intensity lost through absorption of the diffuse radiant fluence plus that gained through the scattering of collimated light into the diffuse portion of the radiance.

Finally, substituting Eq. (IV.15) into Eq. (IV.17), we arrive at the classic diffusion equation:

$$\nabla^2\phi_d(\bar{r}) = 3\mu_t'\mu_a\phi_d(\bar{r}) - 3\mu_t' Q_0(\bar{r}) + 3\bar{\nabla}\cdot\bar{Q}_1(\bar{r}) \qquad \text{(IV.19)}$$

The diffusion equation has a simple solution in the case of a single isotropic point light source in an infinite medium

$$\phi_d\left(\bar{r}\right) = \frac{3\mu_t'}{4\pi}\Phi\frac{e^{-\mu_{eff} r}}{r} \qquad \text{(IV.20)}$$

where Φ is the power of the point light source, r is the distance to the location of the point source, and μ_{eff} is the effective attenuation or transport coefficient:

$$\mu_{eff} = \sqrt{3\mu_a\mu_t'} \qquad \text{(IV.21)}$$

Correspondingly, the effective mean free path or penetration depth, l_{eff}, can be defined by the reciprocal of the effective transport coefficient:

$$l_{eff} = \frac{1}{\mu_{eff}} \qquad \text{(IV.22)}$$

In the case of a single isotropic-point light source in an infinite medium, the point source results in an energy density in the volume with an exponential falloff. In the case of a scattering medium in a finite region of space, the diffusion equation must be solved subject to the appropriate boundary conditions. For different boundary conditions (index matching or mismatching, no incident diffuse light or diffuse light incident), Prahl accomplished the diffuse reflection (T) and transmission (R) of a slab with finite thickness by modeling the phase function as a delta-Eddington phase function [IV.28].

The solutions indicate that, by measuring the diffuse reflection, collimated transmission (T_c), and total transmission ($T_t = T + T_c$) enable the determination of three optical properties: absorption coefficient (μ_a), scattering coefficient (μ_s) and anisotropy coefficient (g). However, if only the diffuse reflection and total transmission measurements are available, only absorption and reduced scattering ($\mu'_s = \mu_s(1-g)$) coefficients can be calculated. Thus, in these cases, additional measurements for determining the scattering anisotropy factor are required.

MATERIALS AND METHODS

Sample preparation

Two different types of dental-resin composites (nano-filled and hybrid) with similar polymeric matrices (dimethacrylates: bisphenol A diglycidylether methacrylate [Bis-GMA], bisphenol A polyethylene glycol diether dimethacrylate [Bis-EMA], urethane dimethacrylate [UDMA], and triethylene glycol dimethacrylate [TEGDMA]), were studied. The characteristics of each dental-resin composite, according to the manufacturers, are shown in Table IV.1.

Table IV.1. Characteristics of the two different types of dental-resin composites analyzed, according to the manufacturers.

Dental-Resin Composite	Organic Matrix	Inorganic Filler	Type
Filtek Supreme XT	Bis-GMA, Bis-EMA, UDMA, TEGDMA	Silica agglomerate, highly dispersed silica	Nanocomposite
Z250	Bis-GMA, Bis-EMA, UDMA	Silica, zirconium dioxide	Hybrid

Each specimen was prepared on a glass plate (Knittel GLASER, Bielefeld, Germany) with a hole bored using a high-speed hand drill with a round bur. After the placement of the composite, a clear plastic sheet (Acrylite Plus Clear, Tap Plastics, Dublin, CA, USA) was laid on the top and bottom of the mould and another glass plate was pressed onto the top to standardize the specimen thickness. Each specimen underwent photo-polymerization for 40 seconds using a light-curing unit (Bluephase, Ivoclar Vivadent AG, Liechtenstein) with an irradiance of 1100 mW/cm^2 ± 10%. After photo-polymerization, all glass plates were removed. Specimens were handled according to manufacturer's instructions. All specimens were prepared by the same user in order to minimize variability.

To analyze zirconia ceramic dental material, we used sintered LAVA^{TM}Zirconia provided by the manufacturer. The sintered ceramic were made using computer-aided design and manufacturing (CAD/CAM) procedures from pre-sintered zirconia blanks, the size of which had been increased to compensate for shrinkage during sintering in a special high-temperature furnace.

The inverse-adding-doubling method

The inverse-adding-doubling (IAD) method is a way to determine the optical properties of turbid media based on the adding-doubling approximation: inverse denotes a reversal of the usual process of calculating reflection and transmission from optical properties, and adding-doubling indicates the method used to resolve the radiative-transport equation.

The adding-doubling method assumes knowledge of the reflection and transmission properties for a single thin homogeneous layer. For a thick sample, the reflection and transmission are estimated by repeated doubling until the desired thickness is reached. The radiance at the two surfaces of a thin slab can be attained if the phase function is known, since the multiple scattering is negligible. If an identical slab is added, the successive scattering back and forth between the component layers may be considered in order to calculate the radiance of the thicker slab. By iteratively adding other thin layers or doubling the total thickness, computation can be made for thicker slabs. With this quick and simple method, anisotropic scattering, internal reflecting, and arbitrary thick-layered media may be modeled [IV.30].

As commented above, optical properties are used as input in order to calculate the reflectance and transmittance by means of the adding-doubling method. Nevertheless, in practice, total reflectance and transmittance values are measured, whereas the optical properties are unknown. Since the situation is the opposite, inverse estimation is needed. The IAD method, therefore, uses total reflectance and total transmittance values as inputs to estimate the values of the optical properties, i.e. absorption and reduced scattering coefficient. In the reverse approach, the optical properties of a sample can be determined by changing them at each iteration until the estimated reflectance and transmittance values match with the measured ones.

To solve the radiative transport equation, the ***iad*** program must be supplied with the experimental values of total diffuse reflectance (M_R) and transmittance (M_T) together with the values of the scattering anisotropy factor (g) and the refraction index (n) of the sample. The program guesses a set of optical properties (μ_a and μ'_s) and then calculates values for reflectance (M_R) and transmittance (M_T). This process is repeated until the calculated and measured values of reflectance (M_R) and transmittance (M_T) are within a specified tolerance (for the sum of both relative differences, the tolerance default value is 0.01%).

In addition, particle simulations based on random sampling from appropriate probability distributions are also solutions for the radiative transfer equation [IV.31, IV.32]. This particle simulation represents the most common Monte Carlo application in radiative transfer.

The Monte Carlo simulation is a statistical method that calculates the trajectories of a great number of photons and, as a result, presents the reflectance and transmission of a sample for a given set of optical parameters. The use of this simulation minimizes systematic errors, considers the scattering phase function, and also takes into account the measuring geometry. A limiting consideration is that the accuracy of quantities calculated increases only with the square root of the number of photon histories, making the Monte Carlo particle simulation a computationally costly method. Nevertheless, as computing power is progressively becoming cheaper, this technique is being more widely applied, for example, in tissue optics [IV.33, IV.34].

The inverse Monte Carlo simulation was included in the *iad* program to achieve an accurate evaluation of the sample's optical properties. The measurements of the total diffuse reflectance (M_R) and transmittance (M_T) used in the IAD method to determine the optical absorption coefficient (μ_a) and reduced scattering coefficient (μ'_s) are modeled by the Monte Carlo simulation technique, which uses a stochastic simulation of light interaction with biological media [IV.35- IV.37].

Figure IV.1 shows a schematic diagram of the *iad*-program logic [IV.28, IV.36]. At the beginning, lost light through the sample edges is fixed at zero and the program calculates a coarse grid for measured reflectance and transmittance values with stipulated absorption coefficient, reduced scattering coefficient, and scattering anisotropy factor (in the case of available g values, they can be assigned by means of a command line of the program which switches this variable to a fixed value). The diffuse and direct reflectance and transmittance are calculated by adding-doubling algorithm for a set of optical properties (μa, μ'_s and g). Then, the lost light for the diffuse and direct fractions is proportionally subtracted and the total reflectance and transmittance is calculated. The loop is repeated by changing the optical properties until the calculated and the measured values match each other. When this occurs, the fraction of lost light is calculated by performing the Monte Carlo simulation. With the lost-light correction, new optical coefficients are sought and the process is repeated again until the changes in the values of the absorption and scattering coefficients are less than 0.1%.

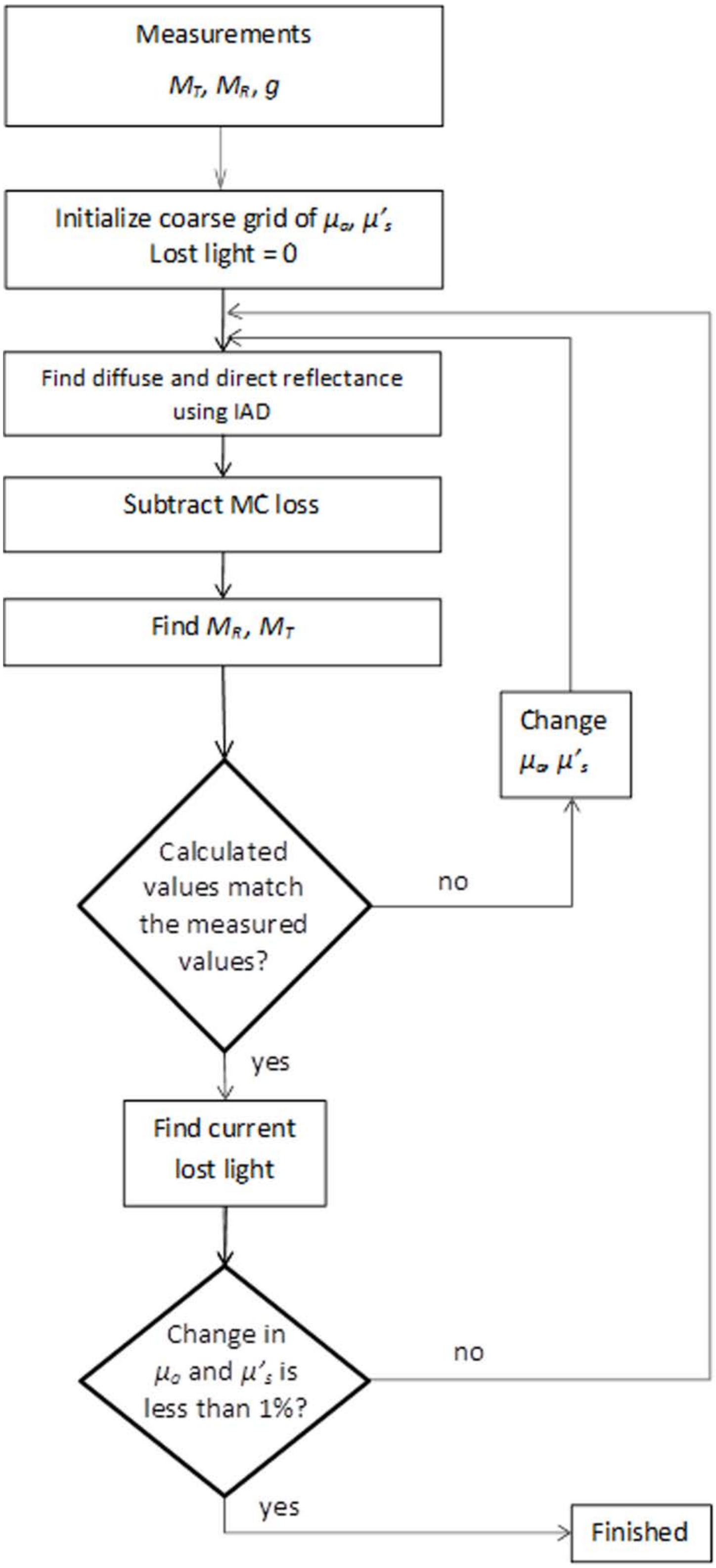

Figure IV.1. Schematic diagram of the *iad*-program logic with diffuse reflectance (M_R) and transmittance (M_T) along with scattering anisotropy factor (g) experimental values as input parameters.

In this chapter, using the ***iad*** program [IV.15], the absorption coefficient (μ_a) and reduced scattering coefficient (μ'_s) were attained from the experimental values of total diffuse reflectance (M_R) and transmittance (M_T) along with those of the scattering anisotropy factor (g) calculated in the previous chapter [IV.23]. The experimental values of total diffuse reflectance (M_R) and transmittance (M_T) were determined by measuring total reflection and transmission with an integrating-sphere setup.

The difference between reflection and reflectance is that reflection is the light reflected by the sample, whereas reflectance is the light reflected by the sample normalized by the incoming light. Analogously, transmission is the light transmitted by the sample, whereas transmittance is the light transmitted by the sample normalized by the incoming light. Hence, reflectance and transmittance are relative quantities ranging between 0 and 1, which are independent of the intensity of the incident light.

For the measurement of the reflected and transmitted light, the sample is situated, respectively, at the exit and entrance port of a sphere. Normally the detector is placed on the inner sphere surface. The integrating-sphere theory accounts for the losses caused by absorption from the sphere wall and light escaping the sphere. The power detected depends on the total light remaining within the sphere and on the relative (to the total sphere area) size of the detector [IV.38, IV.39].

Together with the reflectance and transmittance values, a critical input of the *iad* program is the integrating-sphere wall reflectance r_w. Two measurements (Figure IV.2) are needed to experimentally determine r_w by means of the expression

$$\frac{1}{r_w} = a_w + a_d r_d (1 - a_e) + a_s r_{std} (1 - a_e) \frac{R_{\text{std}}^{\text{diffuse}}}{R_{\text{std}}^{\text{diffuse}} - R_0^{\text{diffuse}}} \qquad \text{(IV.23)}$$

where a_w, a_d, a_e, and a_s are, respectively, the sphere wall (ports excluded), the detector, the entrance port, and the sample, relative areas to the total sphere wall area; r_d and r_{std} are, respectively, the reflectance of the detector and the reference standard.

Eq. (IV.23) illustrates the difficulty in determining accurate values of the sphere-wall reflectance from the measurements. The two diffuse reflectances $\mathrm{R}_{\mathrm{std}}^{\mathrm{diffuse}}$ and $\mathrm{R}_{0}^{\mathrm{diffuse}}$ differ only in the amount of diffuse light leaking from the sphere when the port is empty. Consequently, the difference will be small (roughly proportional to the relative area of the sample port) and any errors in the measurements will be magnified when the division is performed.

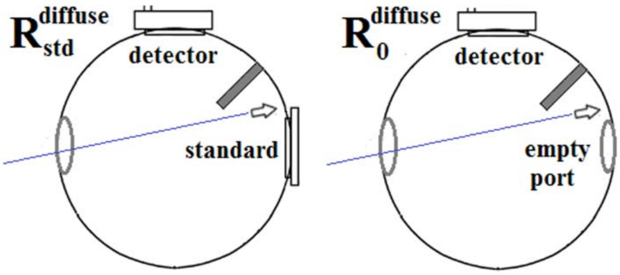

Figure IV.2. Measurements of diffuse reflectance needed to determine the integrating-sphere wall reflectance (r_w).

For a single-integrating-sphere setup using collimated light (i.e. first incident on the sample [Figure IV.3]), the total diffuse reflectance M_R is defined in terms of easily measurable sample and standard reflection as

$$M_R = r_{std} \frac{\mathrm{R}(\mathrm{r}_{\mathrm{s}}^{\mathrm{direct}}, r_{\mathrm{s}}) - \mathrm{R}(0,0)}{\mathrm{R}(\mathrm{r}_{\mathrm{std}}, r_{\mathrm{std}}) - \mathrm{R}(0,0)} \qquad \text{(IV.24)}$$

where R(0,0) is subtracted to discount the effect of the incident light that hits the sphere wall before the sample, which is not uniformly diffuse (the light must hit the walls one more time before becoming uniform).

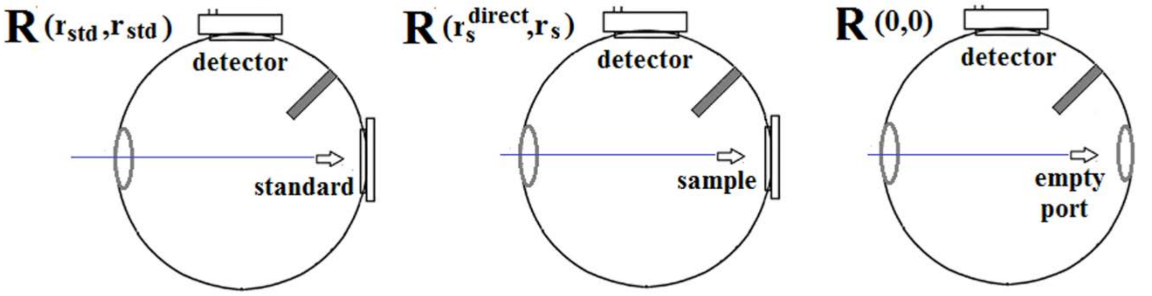

Figure IV.3. Single-integrating sphere measurements of reflection needed to extract the total diffuse reflectance of the sample M_R.

Under the same conditions (single-integrating-sphere setup using collimated light [Figure IV.4]), the total diffuse transmittance M_T is defined in terms of sample reflection and incident light measurements as

$$M_T = \frac{\mathrm{T}(\mathrm{t}_\mathrm{s}^{\mathrm{direct}}, t_\mathrm{s}) - \mathrm{T}_{\mathrm{dark}}}{\mathrm{T}(0,0) - \mathrm{T}_{\mathrm{dark}}} \qquad \text{(IV.25)}$$

where $\mathrm{T}_{\mathrm{dark}}$ constitutes the background signal detected when obscuring the source. Note that, although it is necessary to subtract this signal from every measurement, this subtraction is canceled in Eq. (IV.24).

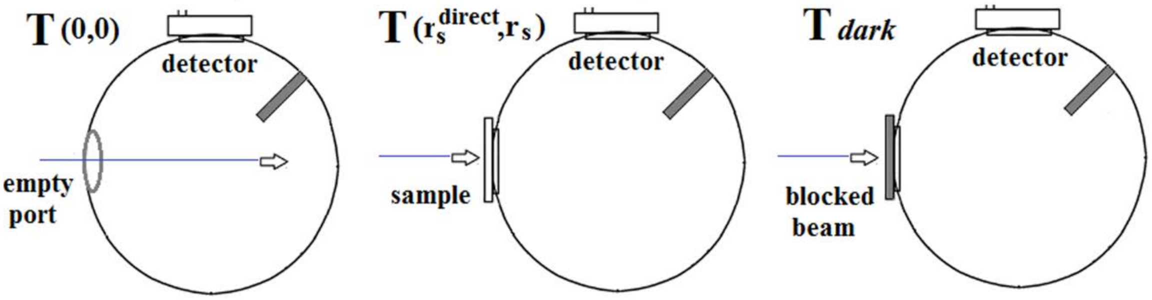

Figure IV.4. Single-integrating sphere measurements of transmission needed to extract the total diffuse transmittance of the sample M_T.

Experimental setup

As commented above, it is difficult to achieve accurate values for the integrating-sphere wall reflectance r_w, since the quantity of interest is a small difference between two measurements. In the present Thesis, this was done under repeatability conditions of measurement in order to determine the corresponding uncertainty: 20 measurements of the two diffuse reflectances were taken, from which 20 values of the sphere-wall reflectance were determined. Then, we calculated the average of the 20 different values and its corresponding type-A uncertainty, expressed as a standard deviation [IV.40]. In addition, to minimize the uncertainty, we repeated this procedure three times, resulting in three sphere-wall reflectance values. Finally, the sphere-wall reflectance was considered to be the average of these three values while its associated uncertainty was computed considering the law of propagation of uncertainties [IV.40]. In Eq. (IV.23), the reflectance of the detector, r_d, was assumed to be negligible. In all the calculations, the manufacturer-specified values for r_{std} were considered.

Reflectance and transmittance values were determined from the direct measurements of total reflection and transmission. It should be noted that these values are independent of the intensity of the incident light.

For each dental biomaterial studied, the reflectance and transmittance values were joined with the corresponding scattering anisotropy value for computing the absorption and the reduced scattering coefficients by means of the IAD method. Again, this was done under repeatability conditions of measurement: the metrological procedure was repeated 20 times with each sample in order to determine the uncertainty associated to the absorption and the reduced scattering coefficients. From these 20 measurements, we calculated the average value of both coefficients and their corresponding type-A uncertainties, expressed as standard deviations [IV.40].

From the average values of the absorption and the reduced scattering coefficients, the effective transport coefficient, μ_{eff}, and the effective mean free path, l_{eff}, were calculated for each biomaterial. The uncertainties associated to these optical properties were computed considering the law of propagation of uncertainties [IV.40], taking into account the uncertainties of the corresponding absorption and reduced scattering coefficients.

It is noteworthy that, in the present PhD thesis, spectral variations not only of the refraction index but also of the scattering anisotropy factor were taken into account. Despite their potential repercussion in accurateness, these aspects are commonly neglected when using the IAD method for determining the optical properties of biological media. Sometimes a single value in the entire spectral range investigated is assumed for n and/or g, but it is not particularly associated with the medium under study [IV.16, IV.41]; other times, g measurements are performed specifically for the medium but with a single wavelength [IV.42- IV.44].

As demonstrated elsewhere [IV.23- IV.25], scattering anisotropy factor values of the dental biomaterials are farther away from zero (isotropy) and also change with the wavelength. This is expected to affect the spectral values of other g-related optical properties. On the other hand, the refractive index of the material is important in determining the optical properties because it affects the reflection at the border lines caused by sample surface and filler particles or matrix, in the case of the dental-resin composites [IV.49, IV.50]. Particularly, for the dental-resin composites, since they are composed of inorganic filler particles immersed in an organic matrix, changes in the refractive index inside the material may have a substantial influence. Since data provided by the manufacturers is restricted to separated values of filler and matrix refractive indexes, we measured the overall refractive index of each dental-resin composite samples with an Abbe refractometer (PCE Iberica, Spain). For the zirconia ceramic, we considered the refractive index values given elsewhere [IV.48].

Below, we describe the laser-integrating-sphere-based setup used to undertake the reflection and transmission measurements on the dental biomaterial samples. This experimental setup is shown in Figures IV.5 and IV.6. Basically, it consists of a laser source, a mirror assembly, a three-port integrating sphere (Oriel 70674, Newport, USA), and a silicon photodiode detector (S2281, Hamamatsu, Japan) connected to a measuring system. The measuring system was composed by a photosensor amplifier (C2719

Hamamatsu, Japan), a multimeter (34401A, Agilent Technologies, USA), and a personal computer.

Throughout the measuring procedure, the photodiode was attached to the same port of the sphere. This port was perpendicular to the sample port and a baffle was located between the two ports to prevent the detection of specular reflected light. Depending on the stage of the measuring procedure, by actuating on the mirror assembly, the laser beam was aimed at the corresponding entrance port: the sample port, for the transmission measurements; and the opposite port, for the reflection measurements. It bears noting that, with this configuration, the sample port was fixed and the entrance port was variable (as opposed to traditional configurations). In this way, the movement of the sample between reflection and transmission measurements was avoided.

For the reflection measurement, mirrors 1 and 2 were plugged, while mirror 3 was put into action in order to aim the laser beam to the reflection entrance port, P_R. The mirrors of the assembly were interchanged for the transmission measurements: 3 was sealed off while 1 and 2 actuated to direct the beam to the transmission entrance port, i.e. the sample port, P_S. At this stage of the measuring procedure, P_R was obturated with a specific port plug of the same material as the inner sphere wall (barium sulfate).

For the sphere-wall reflectance measurements, with the mirrors of the assembly set as in the reflection measurements, the integrating sphere was rotated so that the laser beam first irradiated the sidewall of the sphere between the baffle and the sample port.

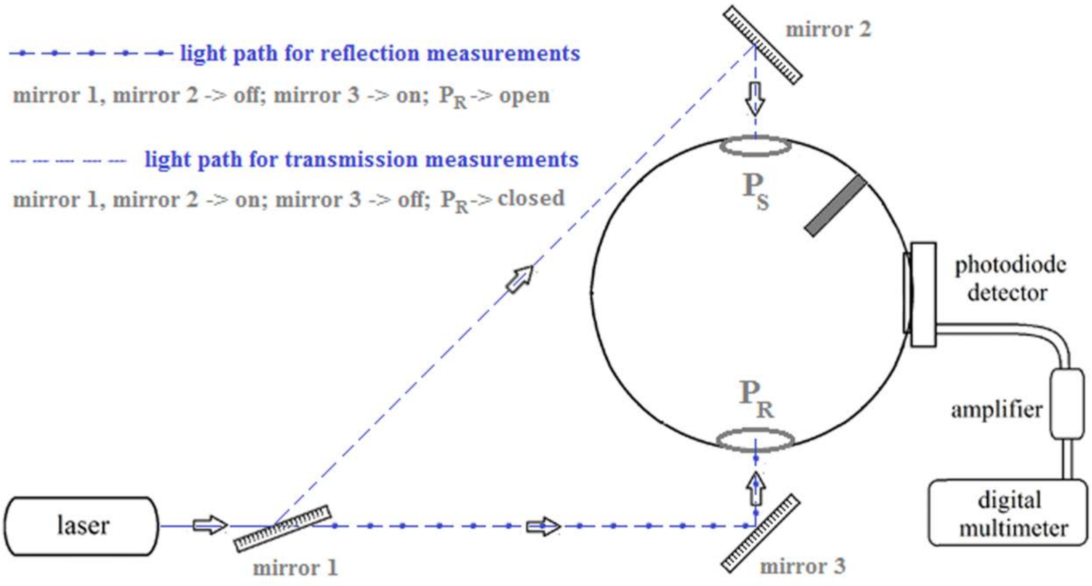

Figure IV.5. Scheme of the experimental setup used in reflection and transmission measurements on the dental biomaterials. P_s is the sample port and P_R is the reflection entrance port (stopped with a port plug for transmission measurements).

Figure 4.6. Experimental setup used in reflection and transmission measurements on the dental biomaterials. A folding mount allows mirror 1 (bottom left) to be lifted away so that the beam reaches mirror 3 (bottom right) for reflection measurements.

With the aim of calculating the optical properties of the biomaterials at different wavelengths, measurements were made using two laser sources: a He-Ne laser source with a power of 12.0 mW (30564, Research Electro Optics, USA), which provided a wavelength of 632.8 nm; and a tunable ion-argon laser source with 1000 mW of maximum total power (Stellar-Pro-L ML/1000, Modu-Laser, USA), which provided wavelengths of 457.9, 488.0, and 514.5 nm. For each of these wavelengths, the whole process of achieving the sphere-wall reflectance and the samples' reflectance and transmittance was performed.

Before the processing, all the data were corrected to reduce effects from background noise, due to laboratory lighting and photodiode dark current (response in the absence of input light-signal, i.e. with the detector in the dark). The background noise was corrected by subtracting from the measured signal values the background signal detected when obscuring the laser source.

The experimental procedure employed fulfilled all the necessary requirements to provide optical-property values with lower associated uncertainties. Firstly, collimated rather than diffuse irradiance was used. Diffuse light may irradiate the sample through the beam by first irradiating the sidewall of the sphere. Alternatively, collimated light may directly irradiate the sample, as occurred in our setup. In the diffuse case, there is a signal registered by the detector due to the light within the sphere, even when no sample is present. Thus all measurements are made with a high background signal. Noise in this background signal, especially with low-reflectance samples, result in uncertainties in the calculation of the reflectance [IV.13]. In the collimated case the sample reflectance acts as the source, and the background signal is due only to the laboratory ambient lighting (almost inappreciable, since it must enter the sphere before reaching the detector) and to the photodiode dark current. Thus, noise in this background signal is expected to be lower with the collimated irradiance that we used. In addition, before processing, we corrected all the data to reduce the effects of this background noise.

Secondly, major difficulties arise in making precise collimated transmission measurements for samples with greater extinction or transport coefficients, due to the low signal registered by the detector. Although the use of a photomultiplier rather than a photodiode could be expected to improve the measurement, this constitutes a much more expensive option. Without the collimated transmission measurement the reduced scattering coefficient cannot be separated into the scattering coefficient and the scattering anisotropy factor *g*, except if the value of the former one (*g*) is already known. In the previous chapter [IV.23- IV.25], goniometric measurements were made in order to recover the experimental phase functions and the corresponding *g* values of dental-resin composites and zirconia ceramic. Given the low uncertainties found, the use of these *g* values offered greater guarantees.

On other hand, with a double-integrating-sphere system, in the reflectance sphere an additional uncertainty will be caused by the signal returning from the transmittance sphere through the sample. For collimated irradiance this signal is not directly proportional to the reflectance of the sample (but rather the transmittance) and is maximal when there is no absorption. This leads to a greater uncertainty in reflectance than with a single-integrating-sphere system [IV.13]. Thus, with the use of a single-sphere system the uncertainty in reflectance decreased because of the exchange of light between the spheres was avoided.

Finally, with conventional integrating-sphere configurations, the reflectance and transmittance measurements were sequentially undertaken keeping the entrance port and changing the sample position. By means of a mirror assembly, this disadvantage was overcome and, consequently, also the uncertainty involved was expected to be reduced. It should be pointed out that, since we did not seek to measure changes in optical properties of biomaterials with external stimulus (such as heating o light-curing), simultaneous measurement of reflection and transmission were not required in this Thesis.

In summary, the experimental procedure employed offered the advantage of using single-sphere system (avoiding light interactions between the spheres) without their disadvantage, since the movement of the sample between reflection and transmission measurements was surpassed with the incorporation of an adequate mirror assembly. This setup is appropriate for steady-state (time independent) biomaterial studies and also recommended when low uncertainties are sought, e.g. in comparative analyses of different materials.

Input parameters for the ***iad*** program

As indicated above, for each wavelength analyzed, the absorption coefficient (μ_a) and reduced scattering coefficient (μ'_s) were determined from the experimental values of total diffuse reflectance (M_R), transmittance (M_T), and scattering anisotropy factor (g) using the ***iad*** program. Together with this data, the program requires some additional parameters related not only to the samples but also to the experimental setup used for the measurements.

In addition to M_R, M_T and g spectral values, the parameters related to the samples required are the thickness and the refractive index values. Table IV.2 shows the thicknesses of the sample determined using a Series 500, Mitutoyo digital caliper (0.01 in sensitivity). The spectral values of the refractive index taken into account are listed in Table IV.3.

Table IV.2. Thicknesses of the samples used in the measurements (values determined with 0.01 mm in sensitivity).

Material	Thickness (mm)
Nanocomposite	0.41
Hybrid composite	0.80
Zirconia ceramic	0.30

Table IV.3. Spectral refraction index values considered for the dental biomaterials analyzed.

λ (nm)	**Nanocomposite**	**Hybrid composite**	**Zirconia ceramic**
457.9	1.5390	1.5320	2.19337
488.0	1.5385	1.5315	2.18254
514.5	1.5380	1.5315	2.17471
632.8	1.5380	1.5315	2.15169

As noted above, among the setup parameters required for the program to describe the particular experiment performed, the integrating-sphere wall reflectance r_w is critical. Table IV.4 lists the experimental r_w values determined as indicate above, together with their corresponding uncertainties.

Table IV.4. Reflectance values of the integrating-sphere wall, with their associated uncertainties.

λ (nm)	457.9	488.0	514.5	632.8
r_w	0.9805 ± 0.0009	0.98263 ± 0.00025	0.9769 ± 0.0006	0.98269 ± 0.00016

Additional input parameters mandatory for executing the *iad* program are the diameters of: the laser beam (2 mm), the integrating sphere (158.2 mm) and the sphere ports (15 mm, in the entrance and sample ones; 11 mm, in the detector one).

RESULTS AND DISCUSSION

For each dental biomaterial analyzed, the spectral values of the optical properties determined are presented in the following tables with their associated uncertainties. Tables 4 IV.5 to IV.7 show the experimental values of: the absorption coefficient, μ_a; the reduced scattering coefficient, μ'_s; the scattering coefficient, μ_s; the effective transport coefficient, μ_{eff}; and the effective mean free path, l_{eff}.

As pointed out above, the values of μ_a, and μ'_s were determined from the measurements, and g values were calculated in the previous chapter (see Table III.4) [IV.23]. By applying Eq. (IV.7), μ_s values were calculated from the values of μ'_s and g. Finally, μ_{eff} and l_{eff} values were calculated as indicated in Eq. (IV.21) and (IV.22), respectively.

Table IV.5. Optical properties with their associated uncertainties for the nanocomposite.

λ (nm)	μ_a (mm^{-1})	μ'_s (mm^{-1})	μ_s (mm^{-1})	μ_{eff} (mm^{-1})	l_{eff} (mm)
457.9	0.0704 ± 0.0014	0.999 ± 0.005	26.08 ± 0.25	0.475 ± 0.005	2.104 ± 0.021
488.0	0.0350 ± 0.0006	0.851 ± 0.012	16.6 ± 0.3	0.305 ± 0.004	3.28 ± 0.04
514.5	0.0281 ± 0.0017	0.769 ± 0.005	17.87 ± 0.20	0.259 ± 0.008	3.86 ± 0.12
632.8	0.01705 ± 0.00104	0.7400 ± 0.0039	43.5 ± 0.6	0.197 ± 0.006	5.08 ± 0.16

Table IV.6. Optical properties with their associated uncertainties for the hybrid composite.

λ (nm)	μ_a (mm^{-1})	μ'_s (mm^{-1})	μ_s (mm^{-1})	μ_{eff} (mm^{-1})	l_{eff} (mm)
457.9	0.0586 ± 0.0005	1.343 ± 0.004	10.41 ± 0.04	0.4964 ± 0.0021	2.014 ± 0.009
488.0	0.0382 ± 0.0004	1.191 ± 0.006	8.24 ± 0.04	0.3753 ± 0.0020	2.664 ± 0.014
514.5	0.0284 ± 0.0012	1.028 ± 0.004	7.13 ± 0.03	0.300 ± 0.006	3.33 ±.07
632.8	0.00221 ± 0.00011	0.7261 ± 0.0014	15.89 ± 0.06	0.0695 ± 0.0018	14.4 ± 0.4

Table IV.7. Optical properties with their associated uncertainties for the zirconia ceramic.

λ (nm)	**μ_a (mm^{-1})**	**μ'_s (mm^{-1})**	**μ_s (mm^{-1})**	**μ_{eff} (mm^{-1})**	**l_{eff} (mm)**
457.9	0.0203 ± 0.0005	14.63 ± 0.12	12.27 ± 0.10	0.945 ± 0.013	1.058 ± 0.015
488.0	0.02889 ± 0.00025	14.15 ± 0.05	11.35 ± 0.06	1.109 ± 0.005	0.902 ± 0.004
514.5	0.0604 ± 0.0007	11.47 ± 0.07	9.30 ± 0.06	1.446 ± 0.009	0.692 ± 0.005
632.8	0.00947 ± 0.00008	20.696 ± 0.014	17.14 ± 0.04	0.767 ± 0.003	1.304 ± 0.005

Data in the former tables confirm the suitability of diffusion theory for the dental biomaterials studied, since the values of the reduced scattering coefficient are much higher than those of the absorption coefficient. On the other hand, the data show that the spectral variations of the reduced scattering coefficient, μ'_s, did not agree with those of the scattering coefficient, μ_s, for all the biomaterials studied. For both dental-resin composites μ'_s decreased monotonically in the wavelength range whereas μ_s presented a minimum. However, for the zirconia ceramic, both scattering coefficients showed similar spectral behavior, with higher values for the reduced one. This illustrates the expected influence of the scattering anisotropy factor values. The factor of 1-g varied between 1.192 ± 0.003 and 1.247 ± 0.005 for the zirconia ceramic, while this factor varied from 0.01700 ± 0.00021 to 0.0513 ± 0.0004 for the nanocomposite, and from 0.04570 ± 0.00014 to 0.1445 ± 0.0003 for the hybrid composite. Zirconia g values are considerably closer to the isotropy ($g = 0$) than the composites g values, which are strongly forward directed (near to 1). Thus, scattering anisotropy has a markedly distinct impact on the optical properties of zirconia ceramics and dental-resin composites, as demonstrated.

For comparisons among the different dental biomaterials at the wavelengths evaluated, the values of the absorption coefficient, μ_a, the scattering coefficient, μ_s, the effective transport coefficient, μ_{eff}, and the effective mean free path, l_{eff}, are jointly represented in Figures IV.7 to IV.10, respectively. In addition, to help the evaluation of the differences between the two dental-resin composites, Figure IV.11 displays simultaneously their values of the reduced scattering coefficient, μ'_s. For the zirconia ceramic, μ'_s spectral values are represented in Figure IV.12. The inclusion of μ'_s values in this figure assists a clearer confirmation of the scattering anisotropy effects. In this figures, the error bars corresponding to the uncertainties have been represented too.

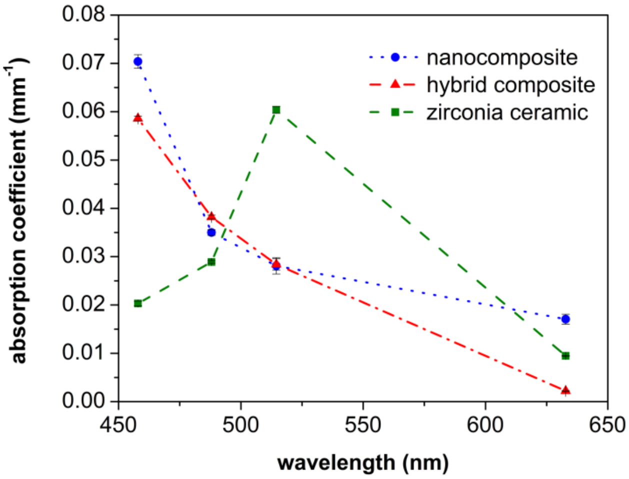

Figure IV.7. Spectral values of the absorption coefficient for the dental biomaterials studied.

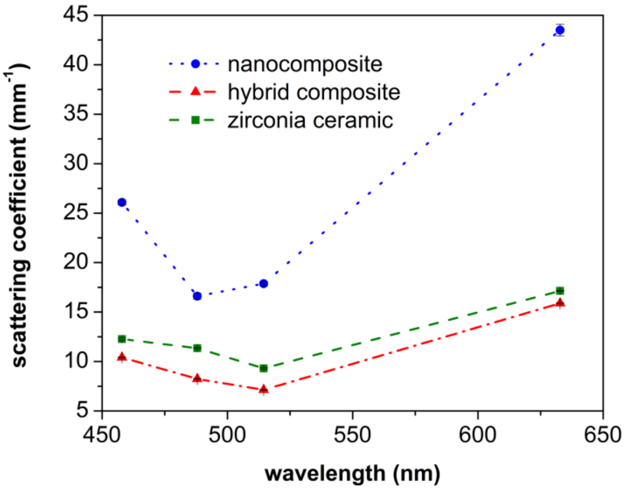

Figure IV. 8. Spectral values of the scattering coefficient for the dental biomaterials studied.

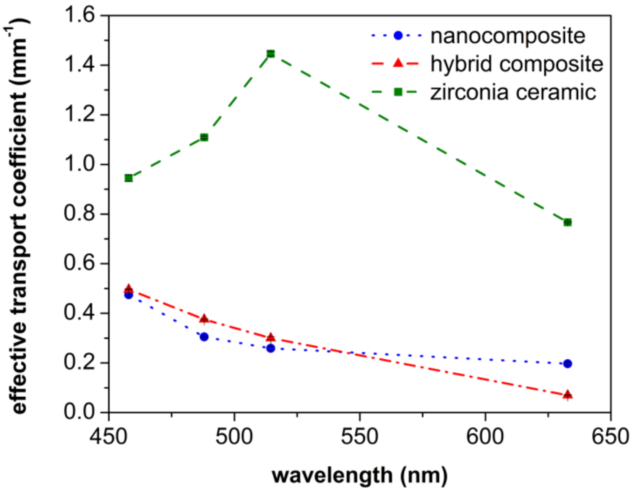

Figure IV.9. Spectral values of the effective transport coefficient for the dental biomaterials studied.

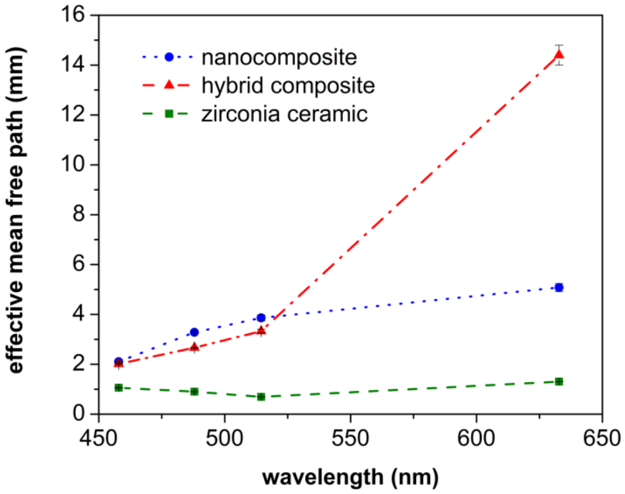

Figure IV.10. Spectral values of the effective mean free path for the dental biomaterials studied.

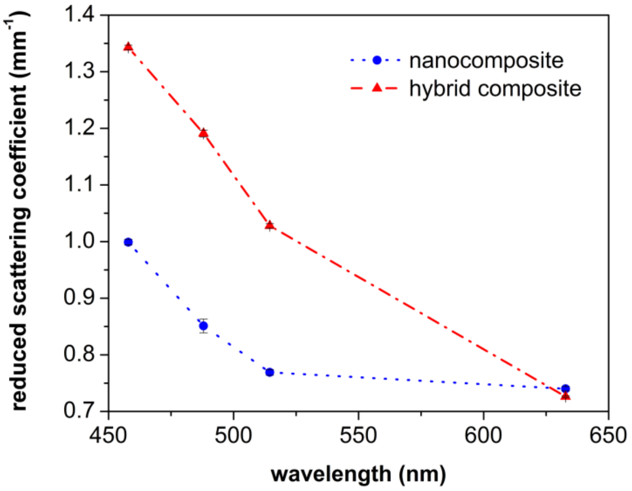

Figure IV.11. Spectral values of the reduced scattering coefficient for the dental-resin composites studied.

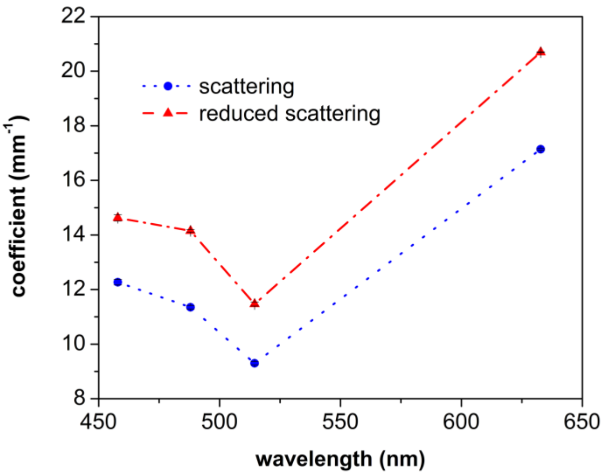

Figure IV.12. Spectral values of the scattering coefficients for the zirconia ceramic studied.

As can be seen, differences in the optical properties of the three dental biomaterials studied are significant. By virtue of the low uncertainties found, the experimental values calculated could be distinguished and compared. The absorption coefficient had similar spectral variations for both dental-resin composites, but completely different for the zirconia ceramic. In the case of the scattering coefficient, the spectral values appeared to follow more parallel trends for the three biomaterials, with higher values for the nanocomposite. Comparisons of the reduced scattering coefficients of only the dental resins revealed that the highest values were presented by the hybrid composite except at the 632.8-nm wavelength. The scattering anisotropy distinct impacts on the optical properties of zirconia ceramic and on those of the dental-resin composites can be clearly checked observing Figures IV.8, IV.11, and IV.12.

For both dental-resins, the effective transport coefficient showed similar spectral trends. On the contrary, the effective transport coefficient of the zirconia ceramic presented not only higher values but also a different spectral tendency compared with the composites. The effective mean free path seemed to present rather dissimilar spectral trends for each dental biomaterial studied, with a marked increment at 632.8 nm in the case of the hybrid composite.

These data may be valuable for clinical applications, since the effective mean path or penetration depth is a measure of how deeply laser light can penetrate into the material. Furthermore, with the knowledge of μ_a, μ_s μ_s, and g, we can estimate spectral values and color coordinates from simulated reflectances without the need of preparing samples for additional measurements [IV.48 - IV.50].

REFERENCES

[IV.1] Qin, J. and Lu, R., "Measurement of the absorption and scattering properties of turbid liquid foods using hyperspectral imaging," Appl. Spectrosc. 61(4), 388-396 (2007).

[IV.2] Randeberg, L. L. and Svaasand, L. O., "Simulated color: a diagnostic tool for skin lesions like port-wine stain," Proc. SPIE 4244, 1–12 (2001).

[IV.3] Pearson, G .J. and Schuckert, K. H., "The role of lasers in dentistry: Present and future," Dent. Update 30(2), 70-74, 76 (2003).

[IV.4] Shigetani, Y., Tate, Y., Okamoto, A., Iwaku, M. and Abu-Bakr, N., "A study of cavity preparation by Er:YAGlaser. Effects on the marginal leakage of composite resin restoration," Dent. Mater. J. 21(3), 238-249 (2002).

[IV.5] Jones, A. H., Diaz-Arnold, A. M., Vargas, M. A. and Cobb D. S., "Colorimetric assessment of laser and home bleaching techniques," J. Esthet. Dent. 11(2), 87-94 (1999).

[IV.6] Kato, J., Moriya, K., Jayawardena, J. A., Wijeyeweera R. L. and Awazu, K., "Prevention of dental caries in partially erupted permanent teeth with a CO_2 laser," J. Clin. Laser Med. Surg. 21(6), 369-374 (2003).

[IV.7] Keller, U., Hibst, R., Geurtsen W., Schilke, R., Heidemann, D., Klaiber, B. and Raab, W. H., "Erbium:YAG laser application in caries therapy. Evaluation of patient perception and acceptance," J. Dent. 26(8), 649-656. (1998).

[IV.8] Ramos, T. M., Ramos-Oliveira, T. M., de Freitas, P. M., Azambuja, N. Jr., Esteves-Oliveira, M., Gutknecht, N. and de Paula, E. C., "Effects of Er:YAG and Er,Cr:YSGG laser irradiation on the adhesion to eroded dentin," Lasers Med. Sci. (2013).

[IV.9] Terry, D.A., Geller, W., Tric, O., Anderson, M. J., Tourville, M. and Kobashigawa, A., "Anatomical form defines color: function, form and aesthetics," Pract. Proced. Aesthet. Dent. 14(1), 59-67 (2002).

[IV.10] Lee, Y. K., "Influence of scattering/absorption characteristics on the color of resin composites," Dent. Mater. 23(1), 124-31 (2007).

[IV.11] Liu, Q. and Ruprecht, E. "Radiative transfer model: matrix operator method," Appl. Opt. 35(21), 4229-4237, (1996).

[IV.12] Prahl, S. A, *The adding-doubling method* in [Optical-thermal response to laser irradiated tissue], Welch A. J. and van Gemert M. J. C. Ed., New York, 101-129 (1995).

[IV.13] Pickering, J. W., Prahl, S. A. van Wieringen, N., Beek, J. F., Sterenborg, H. J. C. M. and van Gemert, M. J. C., "Double-integrating-sphere system for measuring the optical properties of tissue," Appl. Opt. 32(4), 399-410 (1993).

[IV.14] Prahl, S. A, van Gemert, M. J. C. and Welch, A. J., "Determining the optical properties of turbid media by using the adding-doubling method," Appl. Opt. 32(4), 559-568 (1993).

[IV.15] Prahl, S. A., http://omlc.ogi.edu/software/iad/index.html, *iad* program (2012).

[IV.16] Wang, L., Sharma, S., Aernouts, B., Ramon, H. and Saeys, W., "Supercontinuum laser based double-integrating-sphere system for measuring optical properties of highly dense turbid mediain the 1300-2350 nm region with high sensitivity," Proc. SPIE 8427, 84273B-1-6 (2012).

[IV.17] Sardar, D. K., Yust, B. G., Barrera, F., Minum, L. C. and Tsin A. T. C., "Optical absorption and scattering of bovine cornea, lens and retina in the visible region," Lasers Med. Sci. 24(6), 839-847 (2009).

[IV.18] Honda, N., Ishii, K., Kimura, A., Sakai, M. and Awazu, K., "Determination of optical property changes by laser treatments using inverse adding-doubling method," Proc. SPIE 7175, 71750Q-1-8 (2009).

[IV.19] Ishii, K., Kimura, A. and Awazu, K., "Optical properties of tissues after laser treatments in the wavelength range of 350 - 1000 nm," Proc. SPIE 6991, 69912F-1-7 (2008).

[IV.20] Sardar, D. K., Swanland, G. Y., Yow R. M., Thomas R. J. and Tsin A. T. C., "Optical properties of ocular tissues in the near infrared region," Lasers Med. Sci. 22(1), 46-52 (2007).

[IV.21] Chen, Y. C., Ferracane, J. L. and Prahl, S. A., "A pilot study of a simple photon migration model for predicting depth of cure in dental composite," Dent. Mater. 21(11), 1075–1086 (2005).

[IV.22] Tahir, K. and Dainty, C., "Experimental measurements of light scattering from samples with specified optical properties," J. Opt. A: Pure Appl. Opt. 7, 207–214 (2005).

[IV.23] Fernández-Oliveras, A., Rubiño, M. and Pérez, M. M., "Scattering anisotropy measurements in dental tissues and biomaterials," J. Europ. Opt. Soc. Rap. Public. 7, 12016-1-8 (2012).

[IV.24] Fernández-Oliveras, A., Pecho, O. E., Rubiño, M. and Pérez, M. M., "Measurements of scattering anisotropy in dental tissue and zirconia ceramic," Proc. SPIE. Vol. 8427 84272C-1-6 (2012).

[IV.25] Fernández-Oliveras, A., Pecho, O. E., Rubiño, M. and Pérez, M. M., "Comparison between experimental and computational methods for scattering anisotropy coefficient determination in dental-resin composites," Proc. SPIE. Vol. 8427 84272B-1-7 (2012).

[IV.26] Ishimaru, A., [Wave Propagation and Scattering in Random Media], Academic Press, New York, volume 1 (1978).

[IV.27] Chandrasekhar, S., [Radiative Transfer], Dover, New York (1960).

[IV.28] Prahl, S. A., Light Transport in Tissue, PhD thesis, University of Texas at Austin, 1988.

[IV.29] Andrews, L. C., Philips, R. L., [Laser beam propagation through random media], SPIE Optical Engineering Press, Bellingham (2005).

[IV.30] Terán, E., Méndez, E. R., Enríquez, S. and Iglesias-Prieto, R. "Multiple light scattering and absorption in reef-building corals," Appl. Opt. 49(27), 5032-5042 (2010)

[IV.31] Kienle, A. and Patterson, M. S., "Determination of the optical properties of turbid media from a single Monte Carlo simulation," Phys. Med. Biol. 41, 2221–2227 (1996).

[IV.32] Patterson, M. S., Wilson, B. C., Wyman, D. R., T"he propagation of optical radiation in tissue I. Models of radiation transport and their application," Lasers Med. Sci. 6(2), 155-168 (1991).

[IV.33] Palmer, G. M. and Ramanujam, N., "Monte Carlo-based inverse model for calculating tissue optical properties. Part I: Theory and validation on synthetic phantoms," Appl. Opt. 45(5), 1062-1071 (2006).

[IV.34] Palmer, G. M. Zhu, C., Breslin, T. M., Xu, F., Gilchrist, K. W. and Ramanujam, N. "Monte Carlo-based inverse model for calculating tissue optical properties. Part II: Application to breast cancer diagnosis," Appl. Opt. 45(5), 1072-1078 (2006).

[IV.35] Jacques, S. L., *Monte Carlo modeling of light transport in tissues* in [Optical-thermal response to laser irradiated tissue], Welch A. J. and van Gemert M. J. C. Ed., New York (1995).

[IV.36] Prahl SA, Keijzer M, Jacques SL, Welch AJ "A Monte Carlo model of light propagation in tissue," SPIE Institute Series Vol. IS 5, 102-111(1989).

[IV.37] Hourdakis J. and Perris, A., "A Monte Carlo estimation of tissue optical properties for use in laser dosimetry," Phys. Med. Biol. 40(3), 351-364 (1995).

[IV.38] Pickering, J. W., Moes, C. J. M., Sterenborg, H. J. C. M., Prahl, S. A. and van Gemert, M. J. C., "Two integrating spheres with an intervening scattering sample," J. Opt. Soc. Am. A 9, 621-631 (1992).

[IV.39] Prahl, S. A. Vitkin, I. A. Bruggemann, U. Wilson, B. C. and Anderson, R. R. "Determination of optical properties of turbid media using pulsed photothermal radiometry," Phys. Med. Biol. 37, 1203-1218 (1991).

[IV.40] International Organization for Standardization, Guide to the Expression of Uncertainty in Measurement. Corrected and reprinted, Geneva, 1995.

[IV.41] Salomatina, E., Jiang, B., Novak, J. and Yaroslavsky, A. N., "Optical properties of normal and cancerous human skin in the visible and near-infrared spectral range," J Biomed. Opt. 11(6), 064026-1-9 (2006).

[IV.42] Sardar, D. K., Salinas, F. S., Perez, J. J. and Tsin, A. T. C., "Optical characterization of melanin," J. Biomed. Opt. 6(4), 404-411 (2001).

[IV.43] Sardar, D. K., Yow, R. M., Tsin, A. T. C. and Sardar, R., "Optical scattering, absorption and polarization of healthy and neovascularized human retinal tissues," J. Biomed. Opt. 10(5), 0515011-1-8 (2005).

[IV.44] Sardar, D. K. and Levy, L.B., "Optical Properties of Whole Blood," Lasers Med. Sci. 13, 106–111 (1998).

[IV.45] Roggan, A. Albrecht, H. Dörschel, K. Minet, O. and Müller, G., "Experimental set-up and Monte-Carlo model for the determination of optical properties in the wavelength range 330-1100 nm," Proc. SPIE 2323, 21-36 (1995).

[IV.46] Yeh, C. L. Miyagawa, Y. and Powers, J. M., "Optical properties of composites of selected shades," J. Dent. Res. 61(6), 797-801 (1982).

[IV.47] Bass, M., DeCusatis, C., Enoch, J., Lakshminarayanan, V., Li, G., MacDonald, C., Mahajan, V. and Van Stryland, E., [Handbook of Optics. Volume IV: Optical Properties of Materials, Nonlinear Optics, Quantum Optics], McGraw Hill Professional (2009).

[IV.48] Koblova E. V., Bashkatov, A. N., Dolotov, L. E., Sinichkin, Y. P., Kamenskikh, T. G., Genina, E. A. and Tuchin, V. V., "Monte Carlo modeling of eye iris color," Proc. SPIE 6535, 1 (2006).

[IV.49] Randeberg, L. L. and Svaasand, L. O., "Simulated color: a diagnostic tool for skin lesions like port-wine stain," Proc. SPIE 4244, 1–12 (2001).

[IV.50] Svaasand, L. O., Norvang, L. T., Fiskerstrand, E. J., Stopps, E. K. S., Berns, M. W. and Nelson, J. S., "Tissue parameters determining the visual appearance of normal skin and port wine stains," Lasers Med. Sci. 10, 55–65 (1995).

Chapter V.

MEASUREMENTS OF OPTICAL POLARIZATION PROPERTIES: EFFECT ON POLARIZED LIGHT STATE

STATE OF THE ART

Knowing the optical polarization properties of a substance or material has many applications, because these properties are a consequence of the internal structure of the material and can be related to other different properties. For this reason, optical polarization studies are widely used in metrology with diverse goals. Polarization measurements have traditionally been used to indirectly determine the chemical concentration of solutions when the solute is a substance with optical activity. On this basis, an optical polarimetric system allows real-time glucose monitoring and has the potential of being used as a noninvasive measure of glucose for diabetes [V.1].

Well-known photoelastic principles have enabled the development of many industry-friendly tools, such as quality-control tests of solid materials, where stress variations are measured based on the changes of light propagation velocity in birefringent materials. Methods based on the mechanical birefringence have been developed for the investigation of trapped particles and defects in silicon wafers [V.2], to locate laser-induced damage in transparent materials [V.3] and to instantly identify the stress concentration zones in chain-plate assemblies [V.4] or in glass articles of complex shapes [V.5].

The optical properties of biological media are related to their constituents. Many biological tissues or molecules are known to be birefringent, and therefore possess polarization properties. Additionally, biological scatterers such as cell nuclei and mitochondria alter light polarization on each scattering event according to the geometry and optical properties of the scatterers. In biomedical applications, understanding the relationship between the optical and biological properties of tissues has provided not only therapeutic techniques but also diagnosis tools. Optical polarimetry is especially significant for noninvasive diagnosis of neovascularized ocular tissues and hence can enable the detection of ocular diseases such as diabetic retinopathy and macular degeneration [V.6- V.7].

In the field of biomaterials, certain physical and optical properties are often analyzed for quality-control tests as well as for comparing these materials and biological tissues. In dentistry, resin composites are among the most common and widely used materials for replacing dental tissue. For this reason, mechanical and certain optical properties (color, translucency and fluorescence) of these tooth-colored polymeric restorative biomaterials have been extensively studied. Some studies have analyzed polymerization stress for dental resins containing a stress-reducing monomer [V.8] or in nanogel-modified monomer and composite materials [V.9], studies aimed at evaluating shrinkage-strain, hardness, and optical properties as a function of the reducing agent [V.10] or color and translucency in silorane-based resin composites [V.11]. Since optical polarization properties are the consequence of the internal structure of the material and they are related to other properties, the study of optical polarization behavior may provide novel and useful information in this context. In general terms, there is a considerable interest in the investigation of polarized light in biological media, and therefore polarization measurements for biological tissues and biomaterials are needed. In his chapter the aim is to measure the polarized light scattered off of dental tissues and dental-resin composites in order to study their optical polarization behavior and compare them. This information could be useful for the designing and developing a functional tooth.

METHOD AND MATERIALS

Measurement of polarization shift

The experimental setup for polarization measurements for dental tissues and biomaterials is shown in Figures V.1 and V.2. It was composed by a He-Ne laser, two linear polarizers and a detection system based on a photodiode. The former system included a multimeter and an amplifier connected to the photodiode detector. The He-Ne laser (Research Electro Optics model LHRR-1700) with a power of 17.0 mW and beam diameter of 0.98 mm, was random polarized and both polarizers were precision linear polarizers from Newport Corp. (model 10LP-VIS-B).

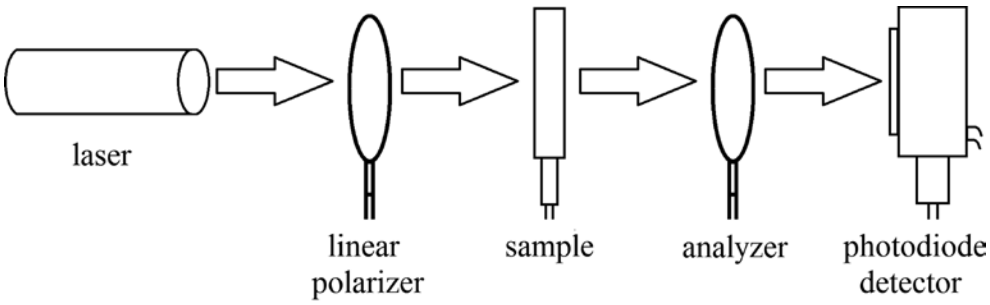

Figure V.1. Scheme of the experimental set-up used for the polarization measurements for dental tissues and biomaterials.

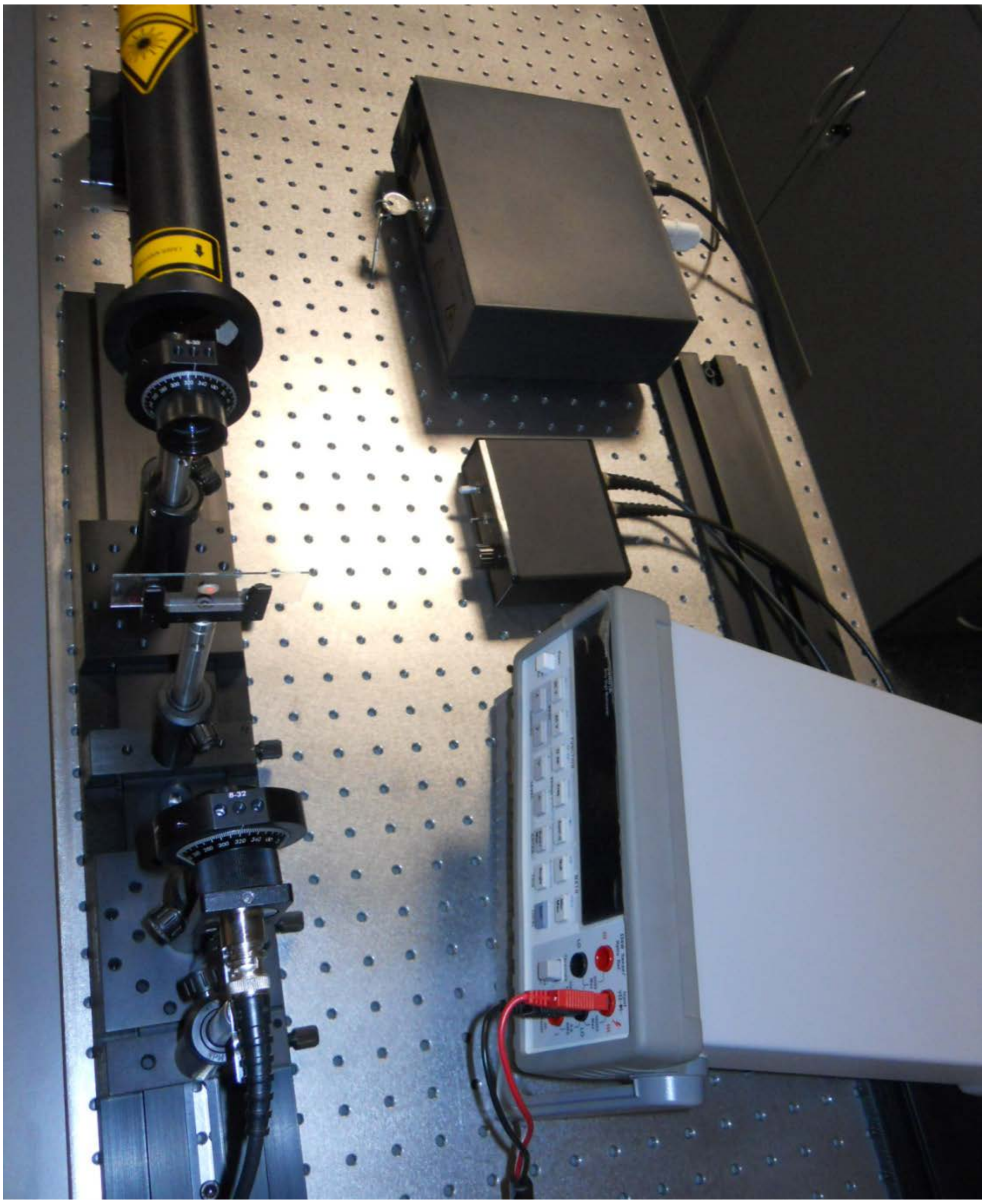

Figure V.2. Experimental set-up used for the polarization measurements for dental tissues and biomaterials.

The laser beam was passed through one linear polarizer placed in front of the sample, beyond which were placed the second linear polarizer (analyzer) and the photodiode detector. At the beginning, the first linear polarizer without the analyzer and the sample in the laser path was rotated to maximize the laser light intensity, indicating that the laser beam was completely polarized in the direction parallel to the transmission axis of the linear polarizer. Then, the analyzer was placed and rotated until the maximum laser light intensity was reached so that the transmission axes of both polarizers were parallel. Once the maximum laser intensity was achieved without the sample in the path of the light, the reference condition was established. Afterwards, the sample was placed between the two linear polarizers and the polarization shift of the scattered laser light was observed. The shift (in degrees) was determined by rotating the analyzer until maximum light intensity was achieved. This was done under repeatability conditions of measurement, in order to determine the corresponding uncertainty: for each sample analyzed, 20 measurements of the polarization shift were taken and the average of the different values was calculated. In addition, to minimize the uncertainties in the measurements, for each material analyzed, measurements were repeated at three different locations on the sample and the averages were considered.

Dental-tissue and biomaterial sample preparation

One human tooth was laterally cut into five slices of 1mm of thickness. All cuts were made with an automatic precision cut-off machine Accutom-5 *Struers* (Ballerup, Denmark). A central slice provided a sample with an outer layer (enamel) and an inner layer (dentine). This specimen was polished with silicon carbide paper from 220 to 4000 grits and finally with alumina slurry of 1, 0.3 and 0.05μm. Then, it was collocated in an ultrasonic cleaner *Renfert* (California, USA) with distilled water in 3 cycles of 10 minutes to eliminate polishing detritus. Finally, the sample was stored in distilled water.

For sample preparation, each resin composite was packed into a hole of a slide cover (10 mm in diameter and 1 mm in thickness). After the packing of the composite, another slide cover was placed below the other one and a third slide cover was pressed on top of the specimen. Each specimen underwent light polymerization for 40 seconds, using a light-curing unit (Bluephase, Ivoclar-Vivadent) with an irradiance of 1100 mW/cm^2± 10% according to manufacturer's instructions. Once resin photopolymerized, both slide covers were removed and the packed composite sample was attained.

The two different types of dental-resin composites studied are indicated in Table V.1. They have similar polymeric matrices, methacrylates: bisphenol A diglycidylether methacrylate (Bis-GMA), bisphenol A polyethylene glycol diether dimethacrylate (Bis-EMA), urethane dimethacrylate (UDMA) and triethylene glycol dimethacrylate (TEGDMA). However, the filler particle type as well as the filler particle-size range and size distribution was different: nanocomposites and hybrid resin composites were evaluated. This is of great importance, since the filler size, content, distribution, and composition might influence properties of the dental-resin composites.

Table V.1. Characteristics of the two different types of dental-resin composites analyzed.

Dental-Resin Composite	**Organic Matrix**	**Inorganic Filler**	**Type**
Filtek Supreme XT	Bis-GMA, Bis-EMA, UDMA, TEGDMA	Silica agglomerate, highly dispersed silica	Nanocomposite
Tetric EvoCeram	Bis-GMA, UDMA, TEGDMA	Ba glass, ytterbium triflouride, mixed oxides, pre-polymers	Hybrid

RESULTS AND DISCUSSION

As described in the previous section, four different dental materials (two dental-resin composites and two human dental tissues) were analyzed under repeatability conditions of measurement. First, without the sample in the path of the laser beam, the analyzer was rotated until the maximum intensity was reached and the angular position of the transmission axis was measured 20 times. To establish the shift reference condition, we calculated the average value of these measurements. For each sample analyzed, the measurement of the transmission axe angular position was also made 20 times, and the average value was calculated as well. The corresponding polarization shift was determined from this average value by subtracting the shift reference condition established. The dispersion associated with the measurements was calculated by a type-A uncertainty, expressed as a standard deviation, and the uncertainty in the polarization shift under repeatability conditions of measurement was calculated according to the law of propagation of uncertainties [V.12].

In addition, to minimize the uncertainties in the measurements, for each material studied, measurements were repeated at three different locations on the sample and the corresponding polarization shifts were determined. Finally, the average value of the shifts was considered and the associated uncertainty was found by applying the law of propagation of uncertainties again. The results for the dental tissues and biomaterials analyzed are shown in Table V.2.

As can be seen in the Table V.2, for human dentine the average value of the polarization shift found was 7 degrees, with an associated uncertainty of 2 degrees. This implies that human dentine has notable polarization properties since the polarization shift found was considerably higher than the corresponding uncertainty. However, for the human enamel and both dental resins the average shift values were found to be similar to their corresponding uncertainties. Therefore, dental-resin composites and human enamel do not show pronounced polarization properties.

Table V.2. Average values of and uncertainties associated with the polarization shift in dental tissues and resin composites.

Dental Tissues and Biomaterials	**Average Value (º)**	**Uncertainty (º)**
Human Dentine	7	2
Human Enamel	2	2
Nanocomposite	2	2
Hybrid	1	2

It is noteworthy that shift values of the former dental materials are very close to each other, while they differ clearly with respect the polarization shift of human dentin. Consequently, the results suggest that although human dentine has remarkable polarization properties, human enamel and dental-resin composites do not show major polarization shifts. This is in agreement with the assumptions of the previous chapter, where the polarization of light was ignored.

REFERENCES

[V.1] Malik, B. H., Coté, G. L., "Real-time, closed-loop dual-wavelength optical polarimetry for glucose monitoring," J. Biomed. Opt. 15(1), 017002: 1-6 (2010).

[V.2] Ng, C. S., Asundi, A. K., "Defect inspections using infrared phase shift field polariscope," Proc. SPIE 7522, 75220A (2009).

[V.3] Wang, P., Asundi, A., "Phase shift polarimetry for non-invasive detection of laser-induced damage," Proc. SPIE 7155, 715511 (2008)

[V.4] Anand, V., Dasari, N., Ramesh, K., "Inspection of assembly stresses in an industrial chain plate using reflection photoelasticity," Proc. SPIE 7522, 75220C (2009).

[V.5] Aben, H., Errapart, A., Ainola, L., Anton, J., "Photoelastic tomography for residual stress measurement in glass," Opt. Eng. 44(9), 093601 (2005).

[V.6] Sardar, D. K., Salinas, F. S., Perez, J. J. and Tsin, A. T. C., “Optical characterization of bovine retinal tissues,” J. Biomed. Opt. 9(3), 624–631 (2004).

[V.7] Sardar, D. K., Yow, R. M., Tsin, A. T. C., Sardar, R., and Tsin, T., “Optical scattering, absorption, and polarization of healthy and neovascularized human retinal tissues,” J. Biomed. Opt. 10(5), 051501: 1-8 (2005).

[V.8] Eick, J. D., Kotha, S. P., Chappelow, C. C, Kilway, K. V., Giese, G. J., Glaros, A. G., Pinzino, C. S., “Properties of silorane-based dental resins and composites containing a stress-reducing monomer,” Dent. Mater. 23(8), 1011-1017 (2007).

[V.9] Moraes, R. R., Garcia, J. W., Barros, M. D., Lewis, S. H., Pfeifer, C. S., Liu, J., Stansbury, J. W., “Control of polymerization shrinkage and stress in nanogel-modified monomer and composite materials,” Dent. Mater., In press (2011).

[V.10] Furusea, A. Y., Mondellib, J., Wattsc, D. C., “Network structures of Bis-GMA/TEGDMA resins differ in DC, shrinkage-strain, hardness and optical properties as a function of reducing agent,” Dent. Mater. 27(5), 497-506 (2011).

[V.11] Pérez, M. M., Ghinea, R., Ugarte-Alván L. I., Pulgar, R., Paravina, R. D., “Color and translucency in silorane-based resin composite compared to universal and nanofilled composites,” J. Dent. 38 (2), e110-e116 (2010).

[V.12] International Organization for Standardization, Guide to the Expression of Uncertainty in Measurement. Corrected and reprinted, Geneva, 1995.

Chapter VI.

RUGOMETRIC INSPECTION FOR DETERMINATION OF ROUGHNESS PARAMETERS AND MEASUREMENTS OF SPECULAR GLOSS

STATE OF THE ART

Research concerning the surface properties of new biomaterials is of great interest for clinical applications. In dentistry, *in vitro* and *in vivo* studies have demonstrated that the surface texture has a significant relationship with plaque formation [VI.1- VI.3]. The roughness of a provided surface has been recognized as the main factor allowing bacteria to adhere to the surface, while less surface roughness is accompanied by reduced plaque retention [VI.4, VI.5]. Greater surface roughness of the tooth helps the penetration of bacteria and plaque accumulation, leading to a higher risk of cavities. Therefore, in restorative dentistry, studying the surface properties of materials meant to replace dental tissues in an irreversibly diseased tooth is important for avoiding harmful changes in future treatments.

On the other hand, the surface properties are intimately related with the optical properties in a material, since the way that light is reflected by the material depends not only on its composition but also on its microstructure. For example, in polymer engineering, the connection between surface quality and optical properties such as gloss and color is increasingly evident [VI.6-VI.8].

Although clinical function and longevity of biomaterials are the first prerequisites in dental applications, optimizing appearance is desirable and increasingly demanded by patients. Surface smoothness, polishability, luster, and specific shade attributes play important roles in achieving optimal aesthetics for dental restorations. Color and gloss are among the major appearance properties of dental biomaterials [VI.9- VI.11] and its relationship with surface roughness has also been reported. [VI.12- VI.13] Gloss is a complex visual impression resulting from surface evaluation [VI.14, VI.15]. The more direct light is reflected, the more obvious the impression of gloss will be.

Perception of tooth color is influenced by many factors, including the optical properties of teeth, such as scattering of light, surface gloss, translucency, and opacity [VI.16]. The surface gloss is related to the roughness because a rough surface will scatter the light. Greater surface roughness results in lower gloss due to the reduction of the flux reflected by the surface in the specular direction.

Consequently, surface properties such as roughness and gloss are essential for a complete characterization of dental biomaterials since they are of major significance in controlling the appearance and, therefore, restoration aesthetics. Hence, comparative studies of different shades and surface treatments on diverse materials that are meant to replace dental tissues may provide useful information for restorative dentistry.

One of the objectives of this chapter is to experimentally analyze the surface-characterization parameters of the different types of dental-resin composites and zirconia ceramics, and comparatively study them. With this aim, non-invasive microtopographic surface inspections of these biomaterials were developed by means of the optical active triangulation systems MICROTOP.06.MFC. The other objective of this chapter is to experimentally determine the specular gloss of different types of dental-resin composites and zirconia ceramics, and comparatively analyze them. Gloss measurements were performed using a glossmeter calibrated with a black glass standard. For comparisons between the different types and colors of dental biomaterials, the uncertainties associated to gloss and roughness parameters were also determined.

THEORETICAL BACKGROUND

Optical triangulation

The general triangulation procedure can be illustrated as in Figure VI.1 [VI.17]. Depth information can be easily obtained. The relation between the measured value (y') and height (Z) is simply:

$$y' = M \frac{Z \sin(\eta+\theta)}{\cos\eta + \left(Z\!\!\diagup\!\! f \right) \cot(\eta+\theta)} \qquad \text{(VI.1)}$$

where $M = f'/f$ is the optical magnification in the observation arm, f and f' are the focal lengths of the observation optics, η the incidence angle and θ the observation one.

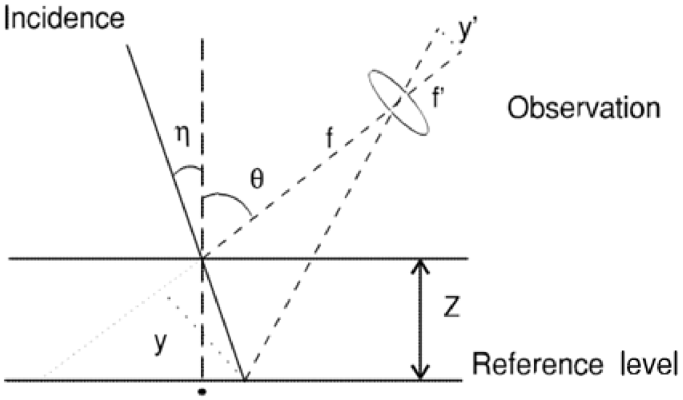

Figure VI.1. A sketch of the general triangulation geometry (courtesy of Prof. Manuel F. M. Costa).

This active triangulation structure illustrated in Figure VI.1 is geometrically equal to the passive triangulation approach were the incidence arm is replaced by a second observation arm.

Without considering interference effects, several systems have been developed that use fringe projection or in general structured lightning. Typically one light stripe is projected onto the object at a known angle and is viewed by one or two cameras from another(s) angle(s). The stripe is made to scan the sample by mechanical or opto-mechanical means.

More popular with the advent of large pixel number CCD cameras and inexpensive, real time frame grabbers and image processing software, became the projection of not just one stripe at the time but a whole fringe pattern covering virtually all the area to be inspected. Other kinds of patterned lightning are employed like grids or arrays of points.

Discreet, active triangulation procedures, where a small diameter or focused well-shaped light beam is projected onto the samples and the areas to be inspected scanned, are also of good use for their reliability and versatility.

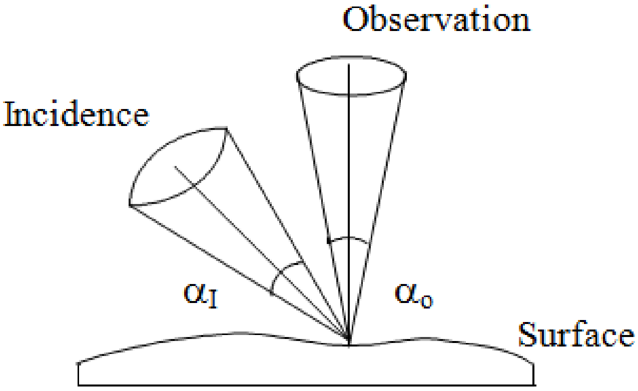

Figure VI.2. Geometry of the surface's relief inspection system (courtesy of Prof. Manuel F. M. Costa).

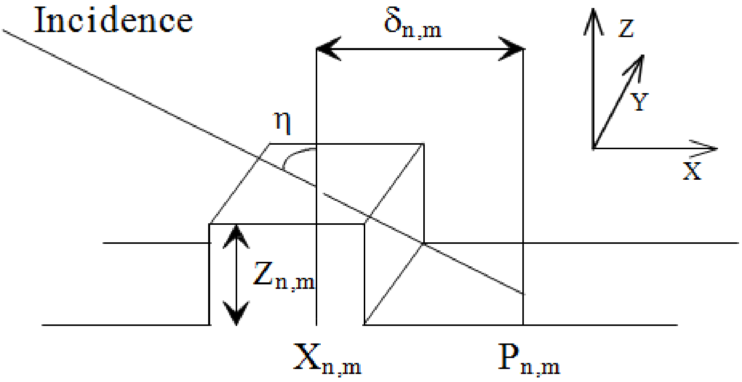

Figure VI.3. The intersection of an oblique light beam with an opaque surface creates on it a bright spot whose lateral position depends on the surface height (courtesy of Prof. Manuel F. M. Costa).

Typically in sensors based in active discreet triangulation the bright spot that is created on a flat surface on the incidence of an oblique light beam (Figures VI.2 and VI.3) moves over the surface when this is given a normal displacement [VI.18]. An observer located above the surface will notice this lateral movement and be able to translate them into the displacement incurred by the surface. Alternatively, if there is a reference level and the sample under observation is placed above it, the lateral movement of the spot can be translated in terms of local thickness.

The sample is placed on a reference surface and scanned by a light beam shinning obliquely, and focused onto a small, diffraction limited, spot on the surface. The scanning is made by moving the sample step by step in equal precisely known increments. At each sampled point, the bright spot's position is imaged on a camera (a linescan camera will be a suitable solution as the spot's position will always lay on the incidence plane) that is interfaced with a microcomputer where the spot's position will be registered. At each scanning step the spot shift regarding the reference position is calculated and the thickness, or height, and the really inspected surface points are computed and identified. The three-dimensional set of co-ordinates (Figure VI.3) will be:

$$\begin{aligned} X_{n,m} &= n\Delta - \delta_{n,m} \\ Y_{n,m} &= m\Phi \\ Z_{n,m} &= \frac{\delta_{n,m}}{M}\cot\eta \end{aligned} \qquad \text{(VI.2)}$$

where η is the incidence angle, Δ the sweep increment in the direction of the plane of incidence (*X*) and Φ in the perpendicular one, *M* the magnification of the observation system placed above, perpendicularly, to the surface, and $\delta_{n,m}$ the spot shift (on the *X* direction), regarding a reference position Pn,m, at the scan position (X_n, Y_m).

The type of the surface under inspection, and its relief characteristic in the three dimensions, condition the overall performance of this method in addition to its particular implementation.

Statistical surface parameters

For the dimensional characterization of surfaces, meaningful statistical parameters such as the average roughness, R_a, are commonly used. R_a, is defined as the average of the absolute deviations with respect to the mean:

$$R_a = \frac{1}{N}\sum_{i=1}^{N}\left|\Delta Z_i\right| \qquad \text{(VI.3)}$$

where $\Delta Z_i = Z_i - Z_m$ are the deviations with respect to the average height, Z_m:

$$Z_m = \frac{1}{N}\sum_{i=1}^{N} Z_i \qquad \text{(VI.4)}$$

R_q is defined with respect to the root-mean-square deviation of the surface-height dataset:

$$R_q = \sqrt{\frac{1}{N}\sum_{i=1}^{N}\Delta Z_i^2} \qquad \text{(VI.5)}$$

Other statistical surface parameters that can be calculated from R_q include the skewness of the surface-height distribution, R_{sk}, given by the third moment about the mean:

$$R_{sk} = \frac{1}{N \cdot R_q^3}\sum_{i=1}^{N}\Delta Z_i^3 \qquad \text{(VI.6)}$$

and the kurtosis of the surface-height distribution R_{ku}, defined by the fourth moment about the mean:

$$R_{ku} = \frac{1}{N \cdot R_q^4}\sum_{i=1}^{N}\Delta Z_i^4 \qquad \text{(VI.7)}$$

The skewness value can range from minus infinity to plus infinity and refers to asymmetry of the distribution. A distribution with an asymmetric tail extending to the right is referred to as positively skewed, while a distribution with an asymmetric tail extending to the left is referred to as negatively skewed. Perfectly symmetric distributions have zero skewness. Kurtosis value refers to the shape of the distribution. Platykurtic distributions have shorter tails than the normal distribution and leptokurtic have longer tails. Platykurtic distributions are defined as having $R_{ku} < 3$, while leptokurtic distributions have $R_{ku} > 3$ [VI.19]. When $R_{sk} = 0$ and $R_{ku} = 3$, the surface has a normal distribution of heights.

Gloss can be defined as an uneven geometrical light distribution reflected by the surface of an object, with an increased flux in the specular direction. Gloss measurements quantify the amount of light reflected in the specular direction of the specimen's surface. The specular angle is equal but opposite to the angle of incidence. Specular light is responsible for the highlight visible on shiny materials. Therefore, gloss measurements quantify how shiny a material is.

A glossmeter is a reflectometer composed of an incandescent light source with a collimator and a photodetector. The light beam is directed onto the surface of the specimen test at a specified incidence angle and the intensity of the reflected light is photoelectrically measured by the detector, which is located in the specular direction of the incident beam. The reflectometer method uses the proportions of directed reflected light as a measure of gloss and, therefore, high reflectometer values are indicative of high gloss.

The measurements relate to the reflected flux of light from a polished black glass plate with a defined index of refraction, which is used as a standard. A gloss of 100 gloss units is assigned to this black glass standard. Besides referring to a black standard, it is also quite common in the literature to relate the reflectometer value to the irradiated light quantity and to express it as a percentage. If the reference or calibration gloss value of the black standard (G_{std}) is known, this can be done by the simple calculation:

$$G = \frac{G_r}{100} \cdot G_{std} \quad \text{(VI.8)}$$

where G_r and G are the reflectometer gloss values related to the black standard and to the irradiated light quantity (as a percentage), respectively.

Reflectometers are differentiated by the illumination/viewing angles. The reflectometer geometry to be used depends on the surface gloss of the specimen under test. The portion of the light reflected by the surface (*R*), depending of the angle of the incoming light (*ε*), can be calculated with the aid of Fresnel's formula [VI.20]:

$$R(n,\varepsilon)=\left[\frac{n^{2}\cdot\cos\varepsilon-\left(n^{2}-\sin^{2}\varepsilon\right)^{\frac{1}{2}}}{n^{2}\cdot\cos\varepsilon+\left(n^{2}-\sin^{2}\varepsilon\right)^{\frac{1}{2}}}\right]^{\frac{1}{2}}+\left[\frac{\left(n^{2}-\sin^{2}\varepsilon\right)^{\frac{1}{2}}-\cos\varepsilon}{\left(n^{2}-\sin^{2}\varepsilon\right)^{\frac{1}{2}}+\cos\varepsilon}\right]^{\frac{1}{2}} \qquad \text{(VI.9)}$$

where *n* is the refraction index of the specimen surface under test, which is assumed to be surrounded by air.

For the values of *n* corresponding to materials such as plastics, ceramics, coats of paints and varnishes, and the like, *R* augments with *ε*, and shows relatively low values over a broad range of the angle of incidence. Owing to the higher proportion of reflected light with large angles of the incoming light, matte surfaces should be evaluated with a wide angle of incidence, semi-gloss ones with a medium angle and high-gloss ones only with a very narrow angle [VI.21-VI.23]. It must take into account that gloss values attained with different angles are necessarily dissimilar, since the portion of the light reflected by the surface changes with the angle of incidence.

METHOD AND MATERIALS

Sample preparation

Two different types of dental-resin composites (nano-filled and supra-spherical) with similar polymeric matrices (dimethacrylates: bisphenol A diglycidylether methacrylate [Bis-GMA], bisphenol A polyethylene glycol diether dimethacrylate [Bis-EMA], urethane dimethacrylate [UDMA], and triethylene glycol dimethacrylate [TEGDMA]), were studied. The characteristics of each dental-resin composite, according to the manufacturers, are shown in Table VI.1.

Table VI.1. Characteristics of the two different types of dental-resin composites analyzed, according to the manufacturers.

Dental-Resin Composite	Organic Matrix	Inorganic Filler	Type
Filtek Supreme XT	Bis-GMA, Bis-EMA, UDMA, TEGDMA	Silica agglomerate, highly dispersed silica	Nanocomposite
Estelite Omega	Bis-GMA, TEGDMA	Silica, zirconia	Supra-spherical

Two different shades of both dental-resin composites were studied: clear translucent and A2 enamel for the nanocomposite; translucent and A2 enamel in the case of the supra spherical composite.

Each specimen was made on a glass plate 1 mm thick (Knittel GLASER, Bielefeld, Germany) with a circular hole prepared using a high-speed hand drill with a round bur. After the placement of the composite, a clear plastic sheet (Acrylite Plus Clear, Tap Plastics, Dublin, CA, USA) was laid on the top and bottom of the mould and another glass plate was pressed onto the top to standardize the specimen thickness. Each specimen underwent photo-polymerization for 40 seconds using a light-curing unit (Bluephase, Ivoclar Vivadent AG, Liechtenstein) with an irradiance of 1100 mW/cm^2 ± 10%.

With this procedure, the resulting specimen is called a *Mylar strip*. After photo-polymerization, a Kerr OptiDisc® surface treatment was applied to one specimen of each dental-resin composite. In this surface treatment a sequence of four abrasive discs is used and the resulting roughness is expected to be coarser than before the treatment. Specimens were handled according to manufacturer's instructions and were prepared by the same user in order to minimize variability. Since the surfaces of all dental-resin samples were treated in a similar manner, between-sample comparisons are possible in this study.

To analyze zirconia ceramic dental material, we used pre-sintered and sintered LAVA™Zirconia samples with similar thicknesses provided by the manufacturer. The sintered ceramics were made using computer-aided design and manufacturing (CAD/CAM) procedures from pre-sintered zirconia blanks, the size of which had been increased to compensate for shrinkage during sintering in a special high-temperature furnace. We studied two sintered zirconia ceramics: SP3-color and uncolored. The sample thicknesses were 0.48 mm, for the pre-sintered zirconia ceramic, and 0.50 mm, for both sintered zirconia ceramics (determined with 0.01 mm in sensitivity).

Rugometric and microtopographic inspection

All samples were submitted to rugometric and microtopographic non-invasive inspection performed with the MICROTOP.06.MFC laser microtopographer in order to determine the statistical surface-characterization parameters R_a, R_q, R_{sk}, and R_{ku}.

For computing the former statistical parameters, the sample surface inspected was 1 mm^2. In this area, 51 one-dimensional profiles with 601 points per profile were recorded. For each sample, the metrological procedure was repeated 20 times in order to determine the uncertainty associated to the surface parameters. From these 20 measurements, we calculated the average value of each parameter and its corresponding type-A uncertainty, expressed as a standard deviation [VI.24].

Below, we briefly describe the optical active triangulation microtopographic inspection system MICROTOP.06.MFC [VI.24- VI.26] used for the rugometric and microtopographic non-invasive inspection of the dental biomaterial samples. The set-up is schematically shown in Figures VI.4 and VI.5 (courtesy of Prof. Manuel F. M. Costa). Its use for inspection in dental applications has already been proved [VI. 28].

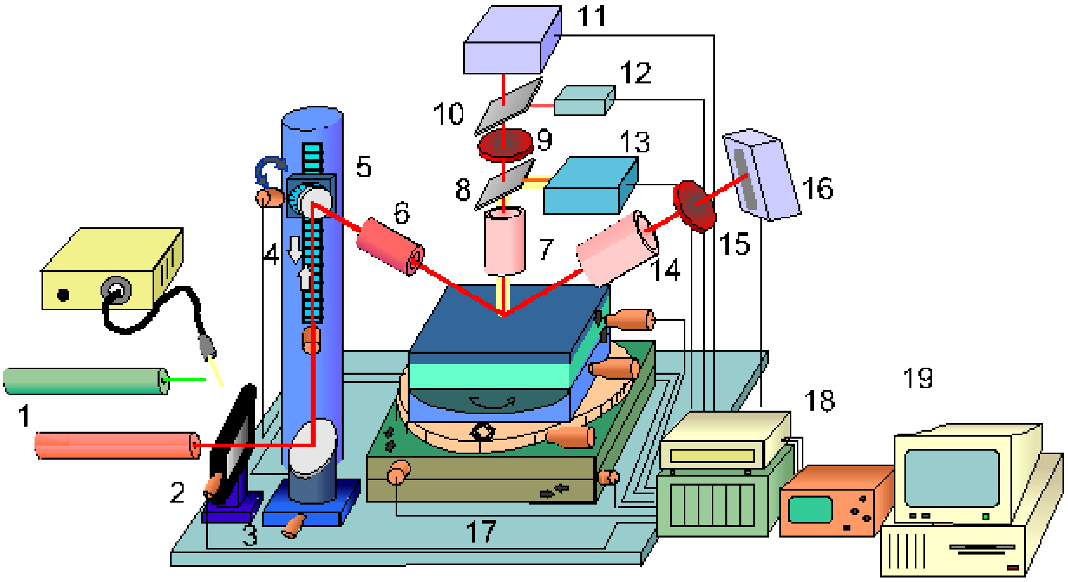

Figure VI.4. Scheme of the MICROTOP.06.MFC microtopographer: 1. Interchangeable light sources; 2. Vibration isolation stand; 3. Neutral density filter; 4. Beam steering system; 5. Incidence angle control motorised system; 6. Incidence optics; 7. Normal observation optics; 8. and 10. Beam splitters; 9. Interference filter; 11. Normal photosensitive detection system; 12. Photodetector; 13. Video camera and illuminator; 14. Specular observation optics; 15. Interference filter; 16. Specular photosensitive detection system; 17. Sample support and motorised positioning system; 18. Data acquisition and control system; 19. Microcomputer.

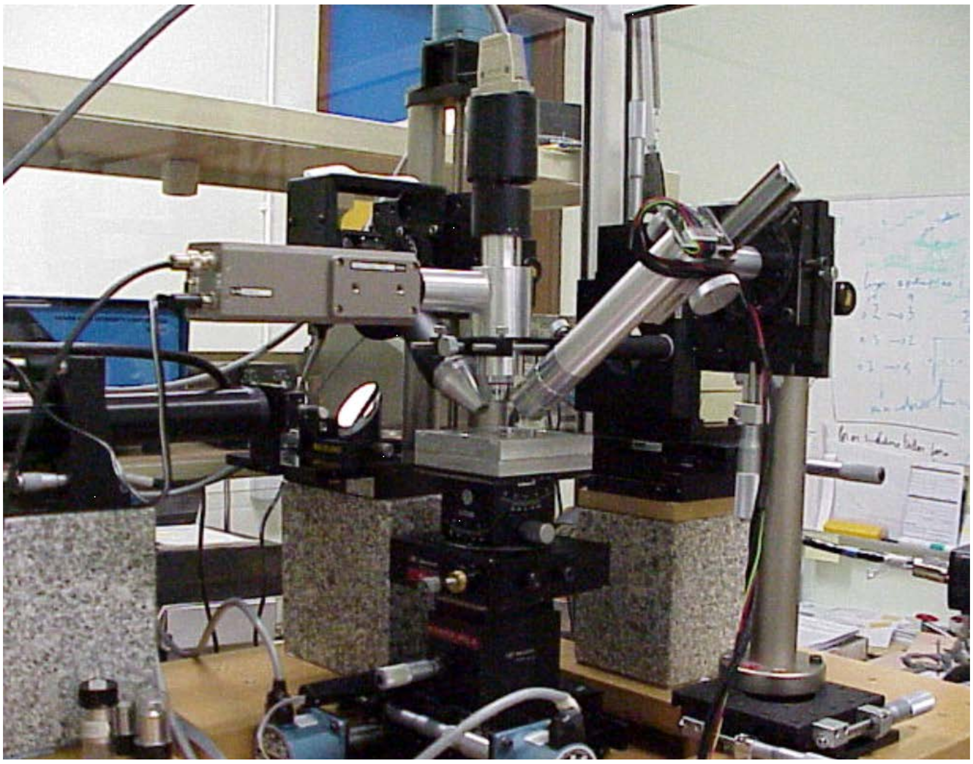

Figure VI.5. The MICROTOP.06.MFC microtopographer.

For several years, optical profilometers and microtopographers were developed at the Physics Department of the Universidade do Minho investigating different applications. For many years the main microtopographer MICROTOP.03.MFC was successfully applied to the examination of a large range of surface types and other inspection tasks [VI.25]. Over the years, small improvements in certain characteristics have been made and special versions have been designed for particular applications such as a portable set and a system to inspect polymers. Recent requests [VI.26, VI.27] have led us to improve the system by incorporating a number of innovative features. Increased versatility and reliability, with a larger measuring range, better accuracy, and resolution now down to the nanometer range have been achieved in the MICROTOP.06.MFC. Discreet active triangulation [VI.25] is the method employed. Essentially in this kind of sensors a beam of light shines on the sample at some angle and the reflected light is collected at another angle.

The surface to be inspected is scanned by one oblique light beam. One Xe white light source and two HeNe lasers at 632.8 and 534 nm are available and can be easily interchanged. The incident light is collimated and focused. A small, diffraction-limited bright spot is thus projected onto the sample. The bright spot is imaged both perpendicularly and specularly onto electronic photosensitive detection systems in order to assess its lateral position. The photosensors are a 2048-pixel Fairchild CCD linear array on the specular arm and a Reticon line scan camera. The area of the surface to be inspected is scanned point by point by the “sensor’s tip” (the light beam focused onto the surface). The system’s greatest robustness was sought. Also a high lateral positioning resolution and accuracy should be achieved. Thus both the incidence arm and observation arms of the sensor are kept fixed. For the sample’s scanning the sensor is moved by means of a precision XY displacement table driven by precision step motors. Piezo-driven motors allow positioning with nanometer resolution within a 1.5-mm range. At each scanning point, on a rectangular array separated by distances down to 1.25 μm, the lateral spot’s position in both sensors is determined and registered.

The spot's shift on both detector planes, between consecutive scan positions is directly related to the height differences between those inspected surface points. In the "specular" arm of the system the detector can be positioned (just introducing an adapter) tilted relative to the observation optics in order to increase the depth range of the sensor (Schleimpflug' condition). Employing the linear arrays, both arms are on a confocal arrangement allowing the best resolution.

The incidence set-up, apart from the light source, comprises a neutral density variable filter, a motorized beam-steering system, a spatial filter, and focusing optics. The change in the incidence angle is synchronized with the shift in observation angle on the "specular" arm. A vertical movement precision stage equipped with computer-controlled motion provided by an accurate DC encoder with high positioning repeatability and resolution is used to refocus the optical observation system but especially for calibration of both arms of the sensor. In order to resolve shaded areas and mutual reflections, a high-precision rotational stage is used to allow easy change to opposite light incidence. Often the faces of the surface to be analyzed are not parallel or simply the surface to be inspected does not lie horizontally. For maintaining the best height resolution, a tilt table was incorporated to the positioning system of the samples. Furthermore, it may allow the inspection of 3D objects or surfaces with pronounced holes, for instance.

Optical observation systems are composed of microscope objective lenses chosen according to the relief characteristics of the surface. The objective lenses can be independently focused in both sensor arms, and they will be used to image the light spot onto the opto-electronic photosensitive detection systems. Both the "normal" and the "specular" sensor arms are attached to a XYZ precision displacement table for finer adjustments. A 2D CCD camera was attached to the system, allowing the capture of bidimensional color images of the scanned area for matching and improved visualization aid. To fulfill different requirements, various photosensitive systems are available and all are interchangeable. A personal microcomputer acquires the data and controls the entire inspection process and the presentation of the results. At the end of the inspection process, we may have just one dataset, though typically two datasets, one for each arm of the sensor. Data processing is independently performed and two sets of parameters and functions are established by triangulation and scattering analysis. The correlation of the datasets is investigated, comparing in order to compile the single best set of reliable and accurate data.

Gloss measurements

Gloss measurements of all dental biomaterial samples were performed with a Minolta Multi-Gloss 268 reflectometer which is schematically shown in Figure VI.6. The Minolta Multi-Gloss 268 is a portable measuring unit which conforms to the standards ASTM D 523, DIN 67 530, ISO 2813and BS 3900 Part D5, and it is provided with the standard geometries of 20º, 60º and 85º.

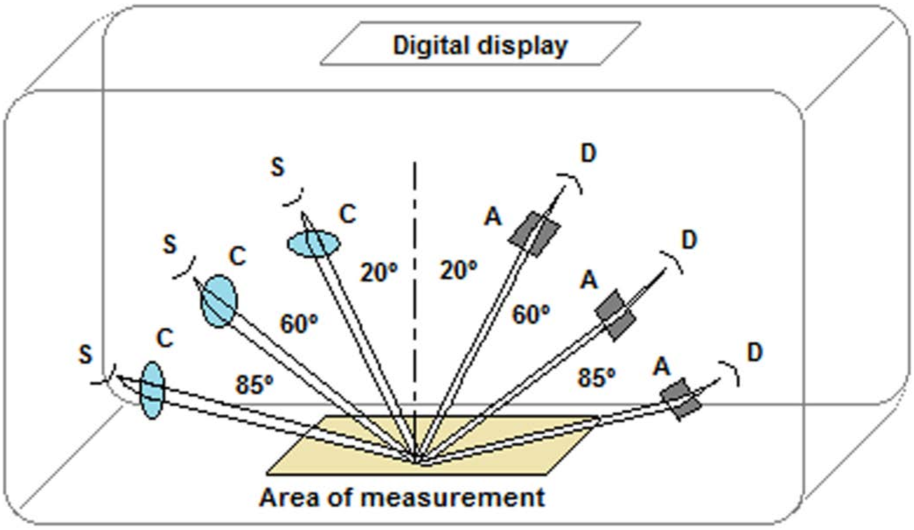

Figure VI.6. Scheme of the Minolta Multi-Gloss 268 glossmeter used to examine the dental biomaterial samples. S: source; C: collimator; A: aperture; D: detector.

When the Multi-Gloss 268 is used, the degree of gloss of the test surface determines the selection of illumination and reflection angles, as follows: semi-gloss surfaces are measured at an angle of 60º. Measurements should range between 10 and 70 gloss units. If highly reflective surfaces are measured using the 60º geometry and the measured value exceeds 70 gloss units, the measurements should be repeated using the 20° geometry. Matte surfaces, however, showing measured values of less than 10 gloss units (using the 60° geometry), should be measured using the 85° geometry. Nevertheless, for a better differentiation of the measured values, the manufacturers recommend using the 85° geometry in all cases in which the value measured at 60° is below 30 gloss units.

According to these instructions, all the dental biomaterial samples were firstly examined using the 60° geometry. Since for all the samples the gloss values measured at 60° were below 30 gloss units, they were all finally examined using the 85° geometry. To perform the measurements, each specimen was placed below the device base and eventually completely covered the measurement area at the center of the aperture. The measurements were carried out in darkness to exclude external light during the readings.

For each sample, the metrological procedure was repeated 20 times in order to determine the uncertainty associated to the gloss values. From these 20 measurements, we calculated the average gloss and its corresponding type-A uncertainty, expressed as a standard deviation [VI.24].

The glossmeter measurements were related to a polished black glass plate with a refractive index of 1.567, used as a standard. Each time before a new test series was measured, the glossmeter was calibrated by comparing the results with the calibration plate, which has a different reference value for each incidence angle. The reference gloss value of the black standard at the 85° geometry was 99.8.

Taking into account the calibration value at the 85° geometry, G_{std}, Eq. (VI.6) was used to relate the reflectometer values to the quantity of irradiated light and to express gloss values as percentages. The uncertainties associated to the gloss percentages were computed considering the law of propagation of uncertainties [VI.24] taking into account the uncertainties of the gloss values related to the standard and the corresponding calibration value.

RESULTS AND DISCUSSION

For the dental biomaterials analyzed, the average surface-parameter values calculated from the microtopographic inspection with their associated uncertainties are presented in the following tables. Table VI.2 shows the surface parameters of the dental-resin composites without surface treatment (*Mylar strip*), whereas the parameters of the dental-resin composites after the OptiDisc® surface treatment are listed in Table VI.3.

As can be seen, differences between the two shades of both kinds of composites are significant. For each dental-resin composite type, the A2 enamel shade shows lower values of R_a and R_q. It may be associated with dissimilarity in the concentration of filler particles for the different shades, resulting in cluster-formation variations. In comparisons of both composite types with similar shades, the roughness parameters R_a and R_q present higher values in the case of the nanocomposite. Larger cluster sizes for the nanocomposite may explain this performance (see Figure VI.7 [VI.29]).

Although the values of R_a and R_q notably increase with the surface treatment, the above observations are valid for the dental-resin composites with and without the treatment. However, the behavior of R_{sk} and the R_{ku} is not the same. For the samples without the surface treatment, the skewness values approach 0 and the kurtosis values tend to 3; therefore, these surfaces have approximately a normal distribution of heights. With the surface treatment, the R_{sk} values become smaller (more negative) and the R_{ku} values larger, moving away from 0 and 3, respectively. As a result, we can conclude that the surface treatment applied to the dental-resin composites not only increases the average roughness but also changes the symmetry and shape of the surface-height distribution, moving it farther away from the normal distribution.

Table VI.2. Average surface parameters with their associated uncertainties for the dental-resin composites without surface treatment (*Mylar strip*).

Material	**Average R_a (µm)**	**Average R_q (µm)**	**Average R_{sk}**	**Average R_{ku}**
Clear translucent nano-composite	0.927 ± 0.012	1.156 ± 0.015	0.12 ± 0.10	3.4 ± 0.3
A2 enamel nano-composite	0.206 ± 0.005	0.258 ± 0.004	-0.124 ± 0.023	3.00 ± 0.04
Translucent supra-spherical composite	0.322 ± 0.004	0.401 ± 0.004	-0.073 ± 0.023	2.92 ± 0.03
A2 enamel supra-spherical composite	0.174 ± 0.005	0.212 ± 0.004	-0.14 ± 0.03	3.28 ± 0.09

Table VI.3. Average surface parameters with their associated uncertainties for the dental-resin composites after the OptiDisc® surface treatment.

Material	**Average R_a (µm)**	**Average R_q (µm)**	**Average R_{sk}**	**Average R_{ku}**
Clear translucent nano-composite	2.43 ± 0.06	3.18 ± 0.08	-0.30 ± 0.18	3.66 ± 0.20
A2 enamel nano-composite	0.90 ± 0.08	1.24 ± 0.13	-1.61 ± 0.23	7.6 ± 1.6
Translucent supra-spherical composite	1.55 ± 0.03	2.07 ± 0.04	-0.59 ± 0.09	4.69 ± 0.09
A2 enamel supra-spherical composite	0.339 ± 0.008	0.63 ± 0.03	-6.34 ± 0.17	71 ± 3

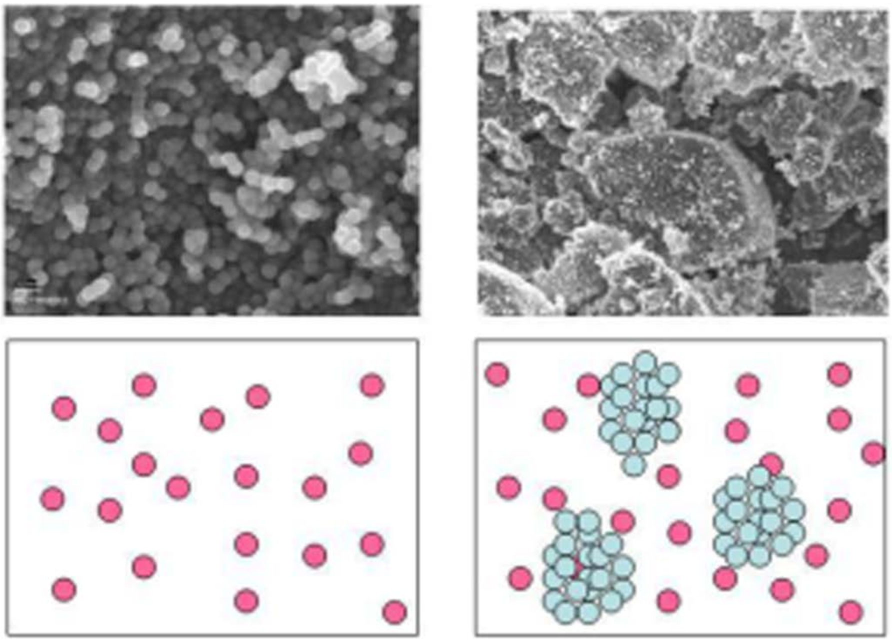

Figure VI.7. Dissimilarity in the filler-particle concentration of dental-resin composites due to cluster formation: nano-filler (left) and nano-filler with clusters (right).

Although the values of R_a and R_q notably increase with the surface treatment, the above observations are valid for the dental-resin composites with and without the treatment. However, the behavior of R_{sk} and the R_{ku} is not the same. For the samples without the surface treatment, the skewness values approach 0 and the kurtosis values tend to 3; therefore, these surfaces have approximately a normal distribution of heights. With the surface treatment, the R_{sk} values become smaller (more negative) and the R_{ku} values larger, moving away from 0 and 3, respectively. As a result, we can conclude that the surface treatment applied to the dental-resin composites not only increases the average roughness but also changes the symmetry and shape of the surface-height distribution, moving it farther away from the normal distribution.

In Figure VI.8, two relief maps obtained with the MICROTOP.03.MFC system for the A2 enamel composite samples without surface treatment (*Mylar strip*) are shown. In Figure VI.9, two relief maps of the treated A2 enamel composite surfaces are present for comparison.

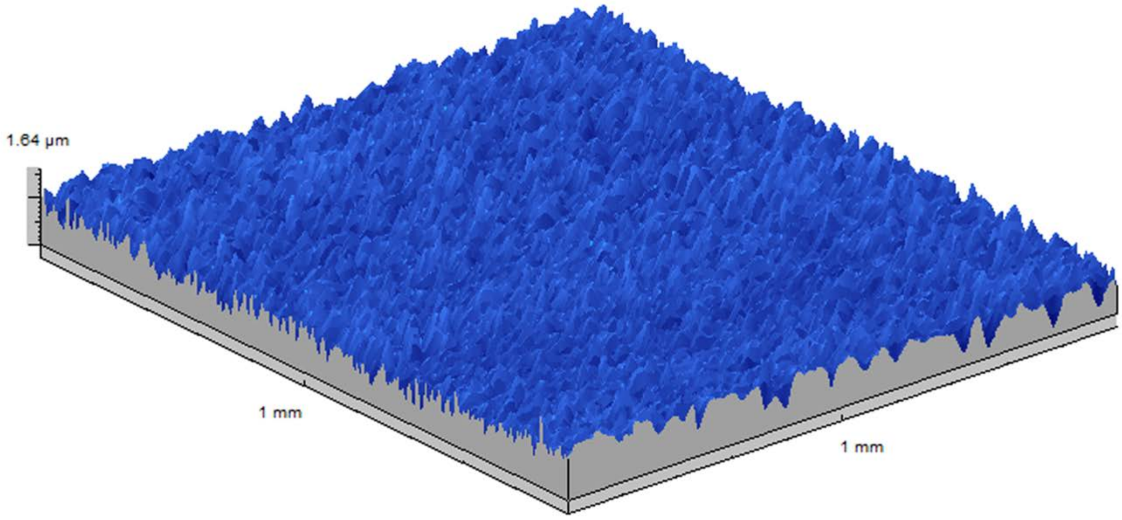

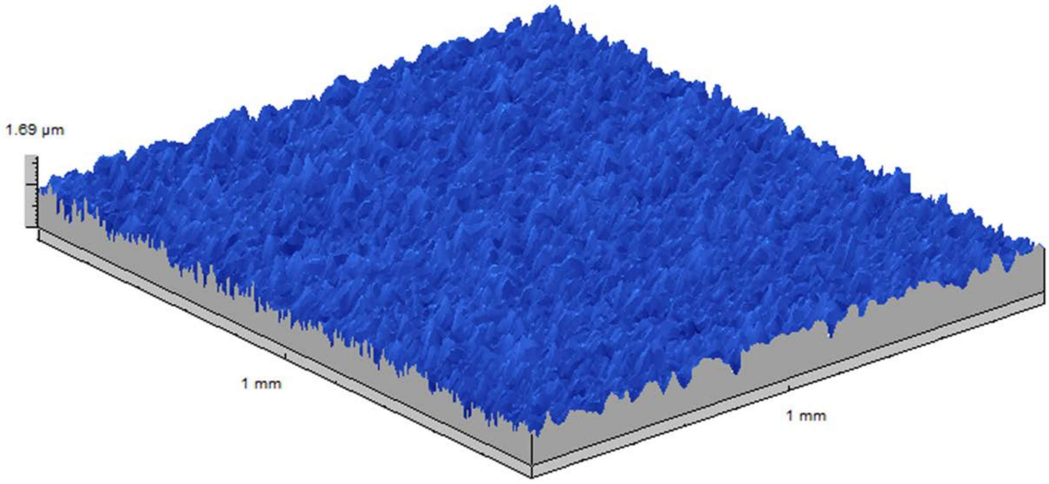

Figure VI.8. Relief maps obtained with the MICROTOP.03.MFC system for the A2 enamel dental-resin composite samples without surface treatment (*Mylar strip*): nanocomposite (top) and supra-spherical composite (bottom).

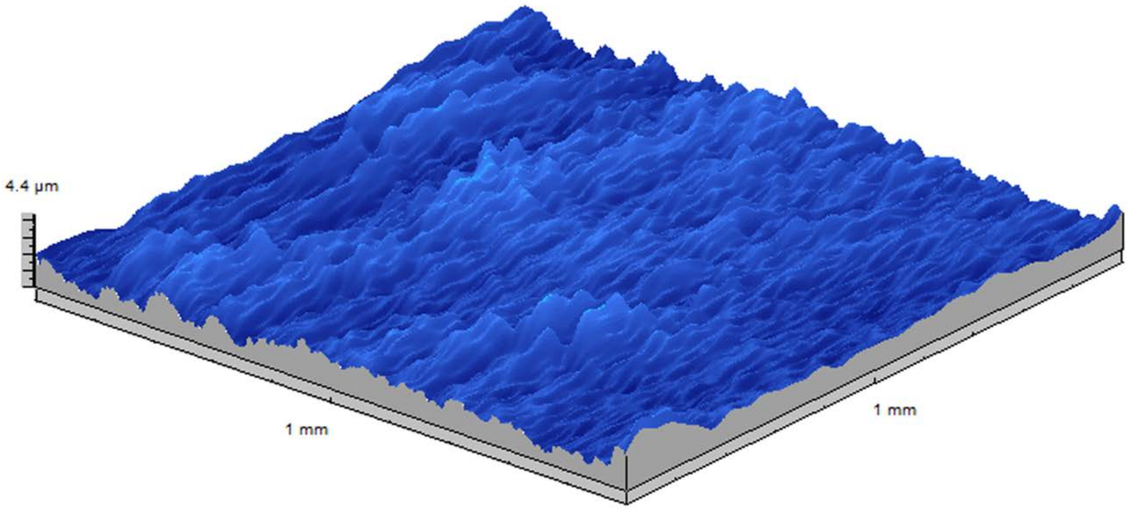

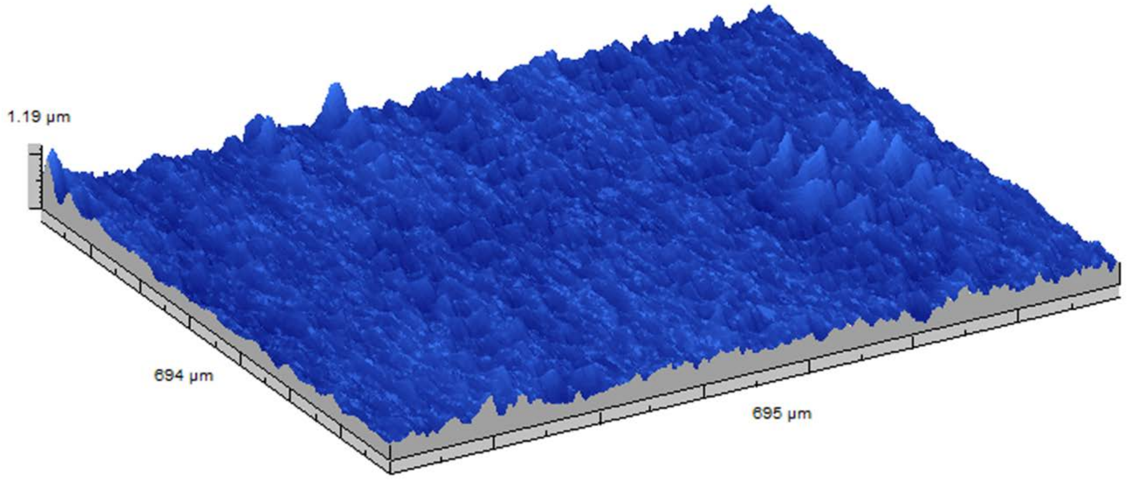

Figure VI.9. Relief maps obtained with the MICROTOP.03.MFC system for the A2 enamel dental-resin composite samples with the OptiDisc® surface treatment: nanocomposite (top) and supra-spherical composite (bottom).

In Table VI.4, we quantify the relative differences in the statistical parameters due to the composite-surface treatment. The uncertainties associated were computed taking into account the law of propagation of uncertainties [VI.24]. Note that, in the case of the clear translucent nanocomposite, the relative difference in R_{sk} is negative because of its change of sign.

Table VI.4. Relative differences in the average surface parameters due to the composite surface treatment with their associated uncertainties.

Material	**R_a relative difference**	**R_q relative difference**	**R_{sk} relative difference**	**R_{ku} relative difference**
Clear translucent nano-composite	1.62 ± 0.08	1.75 ± 0.08	-3 ± 3	0.08 ± 0.10
A2 enamel nano-composite	3.4 ± 0.4	3.8 ± 0.5	12 ± 3	1.5 ± 0.5
Translucent supra-spherical composite	3.82 ± 0.11	4.17 ± 0.13	7 ± 3	0.60 ± 0.04
A2 enamel supra-spherical composite	0.96 ± 0.07	1.96 ± 0.14	45 ± 10	20.8 ± 1.2

The surface parameters of the zirconia ceramics studied are listed in Table VI.5. Comparing the R_a and R_q values of Table VI.5 with those of Table VI.2, the differences between the two sintered zirconia colors are not as remarkable as the ones found between the composites' shades. The roughness parameters R_a and R_q present lower values in the case of the pre-sintered zirconia ceramic. On the other hand, R_{sk} and the R_{ku} take similar values for both sintered and pre-sintered zirconia ceramics, with skewness values close to 0 and the kurtosis values tending to 3. Thus, for the zirconia ceramic studied the sintering process results in an increment of the average roughness without notably affecting the symmetry and shape of the surface distribution of heights.

Table VI.5. Average surface parameters with their associated uncertainties for the zirconia ceramics analysed.

Material	**Average R_a (µm)**	**Average R_q (µm)**	**Average R_{sk}**	**Average R_{ku}**
SP3-color sintered zirconia ceramic	1.295 ± 0.014	1.578 ± 0.014	-0.06 ± 0.06	2.49 ± 0.07
No-color sintered zirconia ceramic	1.268 ± 0.017	1.613 ± 0.021	-0.32 ± 0.05	3.29 ± 0.12
Pre-sintered zirconia ceramic	1.024 ± 0.016	1.264 ± 0.015	-0.28 ± 0.04	2.41 ± 0.03

For the dental biomaterials analyzed, the average gloss percentages and roughness values calculated from the measurements with their associated uncertainties are presented in the following tables. Table VI.6 shows the average gloss and roughness of the dental-resin composites without surface treatment (*Mylar strip*), whereas the averages for the dental-resin composites after the OptiDisc® surface treatment are listed in Table VI.7.

Differences between the two shades of both kinds of composites were found to be significant in the case of the roughness parameters but not for the specular gloss. For each dental-resin composite type, the A2 enamel shade shows lower values of R_a and R_q, but a similar gloss percentage compared to the translucent shade. In comparisons of both composite types with similar shades, the gloss percentage proved similar or slightly lower in the case of the nanocomposite and the roughness parameters present higher values for the aforementioned composite.

Table VI.6. Average gloss percentages and roughness values with their associated uncertainties for the dental-resin composites without surface treatment (*Mylar strip*).

Material	**Average gloss (%)**	**Average R_a (μm)**	**Average R_q (μm)**
Clear translucent nano-composite	3.59 ± 0.10	0.927 ± 0.012	1.156 ± 0.015
A2 enamel nano-composite	3.39 ± 0.10	0.206 ± 0.005	0.258 ± 0.004
Translucent supra-spherical composite	3.59 ± 0.10	0.322 ± 0.004	0.401 ± 0.004
A2 enamel supra-spherical composite	3.59 ± 0.10	0.174 ± 0.005	0.212 ± 0.004

Table VI.7. Average gloss percentages and roughness values with their associated uncertainties for the dental-resin composites after the OptiDisc® surface treatment.

Material	**Average gloss (%)**	**Average R_a (μm)**	**Average R_q (μm)**
Clear translucent nano-composite	3.59 ± 0.10	2.43 ± 0.06	3.18 ± 0.08
A2 enamel nano-composite	2.99 ± 0.10	0.90 ± 0.08	1.24 ± 0.13
Translucent supra-spherical composite	3.59 ± 0.10	1.55 ± 0.03	2.07 ± 0.04
A2 enamel supra-spherical composite	3.59 ± 0.10	0.339 ± 0.008	0.63 ± 0.03

The above observations are valid for the dental-resin composites with and without the treatment. With the surface treatment the gloss percentage decreases only slightly for the A2 enamel nanocomposite, even though the values of R_a and R_q notably increase for all the composite samples. As a result, we can conclude that the surface treatment applied to the dental-resin composites augment the average roughness but the changes in the specular gloss are not significant.

The average gloss percentages and roughness values of the zirconia ceramics studied are listed in Table VI.8. As can be seen, the gloss percentage is higher, and R_a and R_q present lower values in the case of the pre-sintered zirconia ceramic. Thus, for the zirconia ceramic studied, the sintered process results in an increment of the surface roughness with reduced specular gloss.

Table VI.8. Average gloss percentages and roughness values with their associated uncertainties for the zirconia ceramics analyzed.

Material	**Average gloss (%)**	**Average R_a (μm)**	**Average R_q (μm)**
SP3-color sintered zirconia ceramic	0.80 ± 0.10	1.295 ± 0.014	1.578 ± 0.014
No-color sintered zirconia ceramic	2.40 ± 0.10	1.268 ± 0.017	1.613 ± 0.021
Pre-sintered zirconia ceramic	2.99 ± 0.10	1.024 ± 0.016	1.264 ± 0.015

In Table VI.9, we quantify the relative differences in the average gloss percentages and roughness values due to the composite-surface treatment and to the zirconia-sintering process. The uncertainties associated were computed taking into account the law of propagation of uncertainties.

Table VI.9. Relative differences in the average gloss percentages and roughness values due to the composite surface treatment with their associated uncertainties.

Material	Gloss relative difference	R_a relative difference	R_q relative difference
Clear translucent nano-composite	0.00 ± 0.04	1.62 ± 0.08	1.75 ± 0.08
A2 enamel nano-composite	-0.12 ± 0.04	3.4 ± 0.4	3.8 ± 0.5
Translucent supra-spherical composite	0.00 ± 0.04	3.82 ± 0.11	4.17 ± 0.13
A2 enamel supra-spherical composite	0.00 ± 0.04	0.96 ± 0.07	1.96 ± 0.14
SP3-color zirconia ceramic	-0.20 ± 0.04	0.265 ± 0.024	0.249 ± 0.024
No-color zirconia ceramic	-0.73 ± 0.03	0.238 ± 0.026	0.277 ± 0.023

It bears noting that the relative difference in gloss was negative while the relative differences in R_a and R_q were positive. This means that greater surface roughness was accompanied by less specular gloss, corroborating that the relationship between the specular gloss and the surface roughness showed the expected behavior.

REFERENCES

[VI.1] Quirynen, M., Marechal, M., Busscher, H. J., Weerkamp, A. H., Darius, P. L. and Van Steenberghe, D., “The influence of surface free energy and surface roughness on early plaque formation. An in vivo study in man,” J. Clin. Periodontol. 17(3), 138–144 (1990).

[VI.2] Quirynen, M., van der Mei, H. C., Bollen, C. M., Schotte, A., Marechal, M., Doornbusch, G. I., Naert, I., Busscher, H. J. and Van Steenberghe, D., "An in vivo study of the influence of the surface roughness of implants on the microbiology of supra- and subgingival plaque," J. Dent. Res. 72(9), 1304–1309 (1993).

[VI.3] Wu-Yuan, C., Eganhouse, K., Keller, J. and Walters, K., "Oral bacterial attachment to titanium surfaces: a scanning electron microscopy study," J. Oral Implantol. 21(3), 207–213 (1995).

[VI.4] Bollen, C., Papaioannou, W., Van Eldere, J., Scheppers, E., Quirynen, M. and Van Steenberghe, D., "The influence of abutment surface roughness on plaque accumulation and peri-implant mucositis," Clin. Oral Implant. Res. 7(3), 201–211 (1996).

[VI.5] Quirynen, M., Bollen, C. Papaioannou, W., Van Eldere, J. and Van Steenberghe, D., "The influence of titanium abutments surface roughness on plaque accumulation and gingivitis. Short term observations," Int. J. Oral Maxillofac. Implants. 11(2), 169–178 (1996).

[VI.6] Pisciotti, F., Boldizar, A. and Rigdahl, M., "Effects of injection-molding conditions on the gloss and color of pigmented polypropylene," Polym. Eng. Sci. 45(12), 1557-1567 (2005).

[VI.7] Oliveira, M. J., Brito, A. M., Costa, M. C. and Costa, M. F., "Gloss and surface topography of ABS: A study on the influence of the injection molding parameters," Polym. Eng. Sci. 46(10), 1394-1401(2006).

[VI.8] Liu, S. J., Wu, Y. C. and Chen, W. K., "Surface gloss difference on water assisted injection moulded thermoplastic parts: effects of processing variables," Plast. Rubber. Compos. 35(1), 29-36 (2006).

[VI.9] Qualtrough, A. and Burke, F., "A look at dental esthetics," Quintessence Int. 25(1), 7-14 (1994).

[VI.10] Samorodnitzky-Naveh, G., Geiger, S. and Levin, L., "Patients' satisfaction with dental esthetics," J. Am. Dent. Assoc. 138(6), 805-808 (2007).

[VI.11] Terry, D.A., Geller, W., Tric, O., Anderson, M. J., Tourville, M. and Kobashigawa, A., "Anatomical form defines color: function, form and aesthetics," Pract. Proced. Aesthet. Dent. 14(1), 59-67 (2002).

[VI.12] Lee, Y. K., Lim, B. S. and Kim, C.W., "Effect of surface conditions on the color of dental resin composites," J. Biomed. Mate. Res. 63(5), 657-63 (2002).

[VI.13] Egilmez, F., Ergun, G., Cekic-Nagas, I., Vallittu, P. K. and Lassila, L. V., "Estimation of the surface gloss of dental nano composites as a function of color measuring geometry," Am. J. Dent. 25(4), 220-6 (2012).

[VI.14] Hunter, R. S. and Harold, R. W., [The Measurement of Appearance], John Wiley & Sons, New York (1987).

[VI.15] Landy, M. S., "A gloss on surface properties," Nature 447, 158-159 (2007).

[VI.16] Joiner, A., "Tooth colour: a review of the literature" J. Dent. 32(Suppl 1), 3-12 (2004).

[VI.17] Costa, M. F. M., "Optical Triangulation-Based Microtopographic Inspection of Surfaces," Sensors 12, 4399-4420 (2012).

[VI.18] Costa, M. F. M.; Almeida, J. B., "System of optical noncontact microtopography," Appl. Opt. 32, 4860–4863 (1993).

[VI.19] Gadelmawla, E. S.; Koura, M. M., Maksoud, T. M. A., Elewa I. M. and Soliman, H. H., "Roughness parameters," J. Mater. Process. Technol. 123(1), 133-145 (2002).

[VI.20] Goldschmidt, A. and Streitbeger, H. J., [Basf Handbook on Basics of Coating Technology], Vincentz Network, Hannover (2003).

[VI.21] ASTM D523, Standard test method for specular gloss, American Society for Testing and Materials, West Conshohocken, PA, 1995.

[VI.22] ISO 2813, Paints and varnishes – Measurements of specular gloss of non-metallic paint films at 20º, 60º and 85º, International Organization for Standardization, Geneva, 1994.

[VI.23] BS 3900, Methods of test for paints. Part D5: Measurement of specular gloss of non-metallic paint films at 20º, 60º and 85º, London, 1995.

[VI.24] International Organization for Standardization, Guide to the Expression of Uncertainty in Measurement. Corrected and reprinted, Geneva, 1995.

[VI.25] Costa, M. F. M. "Surface Inspection by an optical triangulation method," Opt. Eng. 35(9), 2743-2747 (1996).

[VI.26] Costa, M. F. M. and Teixeira, V. "Rugometric and Microtopographic Inspection of Cr-Cr2O3 Cermet Solar Absorbers," Int. J. Photoenergy 1110-662X , article ID 82327 (2007).

[VI.27] Costa, M. F. M., Batista, C., Portinha, A., Teixeira, V., Oliveira C. R., and Ribeiro, R. M., "Microtopographic inspection of laser glazed thermal barrier coatings," Opt. Eng. 47(6), 063603-1-6 (2008).

[IV.28] Costa, M. F. M. and Pereira, P. B., "Optical microtopographic inspection of the surface of tooth subjected to stripping reduction," Proc. SPIE 8001, 80012X-1-5 (2011).

[IV.29] Ugarte-Alván, L. I., Evaluación óptica de nuevas resinas compuestas: nanocomposites y resinas de silorane, PhD thesis, University of Granada, 2010.

Chapter VII.

CONCLUSIONS

1.- Angular-scattering measurements were made for a spectral characterization of the dental tissues and biomaterials in the visible range. Previously, measurements had been made with different sample thicknesses, checking the behaviour of the angular-scattering profile. *g* values had similar spectral variations, except for the human dentine. The thicker samples yielded a less forward-directed scattering profile than did the thinner samples.

The uncertainty corresponding to *g* values fell within the range of 0.00011 and 0.005. Zirconia *g* values were considerably closer to the isotropy ($g = 0$) than the composites' *g* values, which were strongly forward-directed (near to 1). The angular scattering profiles indicated the presence of a more pronounced forward-directed scattering in the nano-filled dental-resin than in the hybrid dental-resin composite. For the zirconia ceramic, the outcome of sintering displayed an optical behaviour more similar to that of dentine tissue, in terms of scattering anisotropy.

The dental-resin composites and the human enamel showed a similar angular scattering behaviour. On the other hand, the zirconia ceramic presented a scattering angular behaviour more similar to that of the human dentine. This is valuable for biomedical applications, since it means that, in terms of angular scattering behaviour, the biomaterials are comparable to the tissues that they are meant to replace.

2.- The IAD method was used to combine the results of the goniometric measurements with transmittance and reflectance measurements performed using a laser-integrating-sphere-based setup. The experimental procedure was conducted under repeatability conditions of measurement and fulfilled all the necessary requirements to provide optical-property values with lower uncertainties. Therefore, this procedure is advisable for the comparative analysis of different materials.

The results agreed with the application of the diffusion theory, since the reduced scattering coefficient had values much higher than the absorption coefficient. The scattering anisotropy had clearly distinct impacts on the optical properties of zirconia ceramic and dental-resin composites. The absorption coefficient had similar spectral variation for both dental-resin composites, but thoroughly different for the zirconia ceramic. In the case of the scattering coefficient, the spectral values appeared to follow more parallel trends for the three biomaterials, with higher values for the nanocomposite. The effective transport coefficient of the zirconia ceramic presented not only higher values but also a different spectral behavior compared with the composites. The effective mean free path seemed to show somewhat dissimilar spectral trends for each dental biomaterial, with a marked increment at 632.8 nm in the case of the hybrid composite.

3.- Dental-resin composites and human enamel did not show significant polarization shifts. However, optical polarization properties of human dentine were found to be different. Nevertheless, differences between nanocomposite and hybrid dental-resin composite did not proved to be significant in terms of their optical polarization behavior.

4.- Dental-resin composites and pre-sintered and sintered zirconia ceramics were submitted to rugometric non-invasive inspection performed with the MICROTOP.06.MFC laser microtopographer. Gloss measurements were conducted using a glossmeter device. The experimental procedure was conducted under repeatability conditions of measurement in order to determine the uncertainty related to gloss and roughness parameters.

The surface treatment applied to the dental-resin composites not only increased the average roughness but also changes the symmetry and shape of the surface-height distribution, moving it farther away from the normal distribution. However, the changed in the specular gloss due to the surface treatment were significant only for the A2 enamel nano-composite. The sintering process of the zirconia ceramics appeared to increase the average roughness and reduce the specular gloss, without notably affecting the symmetry or shape of the surface-height distribution.

The differences between the two shades of both kinds of composites were significant in the case of the roughness parameters but not for the specular gloss. In comparisons of both composite types with similar shades, the gloss percentage proved to be similar or slightly lower in the case of the nanocomposite. In addition, the roughness parameters R_a and R_q presented higher values for this dental-resin composite.

The experimental methods used for determining the optical properties and the surface roughness parameters were shown to be suitable for comparison between materials by virtue of the low uncertainties found.

Chapter VIII.

PUBLICATIONS

Scientific publications resulting from the work developed in this PhD thesis are:

Fernández-Oliveras, A., Rubiño M. and Pérez M. M., "Scattering and absorption properties of biomaterials for dental restorative applications". Submitted (2013).

Fernández-Oliveras, A., Rubiño M. and Pérez M. M., "Determination of optical properties in dental restorative biomaterials using the inverse-adding-doubling method". Proc. SPIE, in press (2013).

Fernández-Oliveras, A., Costa, M. F. M., Pecho, O. E., Rubiño, M. and Pérez, "Rugometric and microtopographic non-invasive inspection in dental-resin composites and zirconia ceramics". Proc. SPIE, in press (2013).

Fernández-Oliveras, A., Costa, M. F. M., Yebra, A., Rubiño, M. and Pérez, M. M., "Gloss measurements and rugometric inspection in dental biomaterials". Proc. SPIE, in press (2013).

Fernández-Oliveras, A., Rubiño, M. y Pérez M. M., "Análisis comparativo de medidas de anisotropía de scattering en tejidos y biomateriales dentales". Ópt. Pura Apl., 46(2), 83-88 (2013).

Fernández-Oliveras, A., Rubiño M. and Pérez M. M., "Scattering anisotropy measurements in dental tissues and biomaterials". J. Eur. Opt. Soc.-Rapid Publ. 7, 12016-1-12016-8 (2012).

Fernández-Oliveras, A., Pecho, O. E., Rubiño, M. and Pérez, M. M., "Measurements of scattering anisotropy in dental tissue and zirconia ceramic". Proc. SPIE 8427, 84272C-1-6 (2012).

Fernández-Oliveras, A., Carrasco, I. M., Ghinea, R., Pérez, M. M. and Rubiño, M., "Comparison between experimental and computational methods for scattering anisotropy coefficient determination in dental-resin composites". Proc. SPIE 8427, 84272B-1-7 (2012).

Fernández-Oliveras, A., Rubiño, M. y Pérez M. M., “Análisis comparativo de medidas de anisotropía de scattering en tejidos y biomateriales dentales”. Actas de la X Reunión Nacional de Óptica. Zaragoza, España (2012).

Fernández-Oliveras, A., Pecho, O. E., Rubiño, M. and Pérez, M. M., “Measurements of optical polarization properties in dental tissues and biomaterials”. Proc. SPIE 8001, 80012Y-1-7 (2011).

Fernández-Oliveras, A., Pecho, O. E., Rubiño M. and Pérez M. M., “Optical polarization measurements of dental tissues and nanocomposites”. Histology and Histopathology, Volume 26 (supplement 1), 315 (2011).

Chapter IX.

FUNDING

This latest chapter is dedicated to funding sources that have made this PhD thesis possible. Thanks to this funding, the materials, instrumentation and devices required to perform the experimental measurements were acquired. They have also supported participation in scientific events, research stays and publications related to this Thesis. These sources of funding are:

Beca de Formación de Investigadores, Programa 3 del Plan Propio de Investigación de la Universidad de Granada. Application: 2008. Recipient: Alicia Fernández Oliveras. Supervisor: A. Manuel Rubiño López. Organization involved: Departamento de Óptica de la Universidad de Granada. Period: 01/10/2008 - 31/11/2008.

Beca de Formación del Profesorado Universitario (FPU), Ministerio de Ciencia e Innovación. Application: 2008. Recipient: Alicia Fernández Oliveras. Supervisors: A. Manuel Rubiño López and M. del Mar Pérez Gómez. Organization involved: Departamento de Óptica de la Universidad de Granada. Period: 01/12/2008 - 24/03/2013.

Proyecto I+D MAT2009-09795, Ministerio de Ciencia e Innovación. Coordinator: M. del Mar Pérez Gómez. Organization involved: Departamento de Óptica de la Universidad de Granada. Period: 01/01/2010 - 31/12/2012.

Grupo de Óptica de Granada FQM 151, Plan Andaluz de Investigación de la Junta de Andalucía (PAI). Coordinator: Enrique F. Hita Villaverde. Organization involved: Departamento de Óptica de la Universidad de Granada. Period: 10/12/2007 - present.